Optimal control and noise characterization for few qubit systems

Dissertation zur Erlangung des Grades des Doktors der Naturwissenschaften der Naturwissenschaftlich-Technischen Fakultät der Universität des Saarlandes

von
Jurek Frey

Saarbrücken
2026

UNIVERSITÄT
DES
SAARLANDES

Tag des Kolloquiums:	13.07.2026
Dekan:	Prof. Dr.-Ing. Dirk Bähre
Berichterstatter:	Prof. Dr. Frank Wilhelm-Mauch Prof. Dr. Joachim Ankerhold
Vorsitz:	Prof. Dr. Jürgen Eschner
Akad. Mitglied:	Dr. Carsten Baltes

Acknowledgments

Here, I would like to take the opportunity to thank everyone who made this work possible.

Foremost, I would like to thank my professor, Prof. Frank Wilhelm-Mauch, both for giving me the opportunity to do my doctorate in his research group and for his constant, well-intentioned support. His expertise and incredible knowledge were very helpful in creating this work.

Additionally, I want to express my gratitude to my supervisors, Shai Machnes and Matthias Müller. They were always willing to listen to me throughout the entire process and answered countless questions of mine. In doing so, they guided me constructively through the ups and downs of the academic challenge of writing a PhD thesis.

Furthermore, I would like to thank the entire research group of PGI-12 for helpful discussions, friendly cooperation, and both professional and social-emotional support.

Finally, my heartfelt thanks go to my friends and family. Without the support and motivation I received from these people, this work definitely would not have been possible.

Abstract

New technologies such as quantum computers and associated networks can be used to solve certain computational problems more efficiently and to make communication between participants more secure. Superconducting qubits have established themselves as a promising platform in the field of computing, while vacancy centers with elements from the fourth main group are the focus of current research for building a quantum internet in the context of communication and distributed quantum computing.

In this work, we show characterization and optimal control of elementary building blocks of such quantum systems. After the introduction, the first section is dedicated to the characterization and simulation of vacancy centers with elements from the fourth main group, using a germanium vacancy center as an example. These are considered promising candidates for a quantum repeater.

In the second part, we present new possibilities for the efficient optimization of the control of quantum systems. Here, we compare optimization methods in the context of non-Gaussian noise processes with regard to precision and computational effort. The goal is to better understand decoherence in quantum systems and to effectively combat its causes.

In the final part, an experiment with a superconducting qubit is simulated and characterized. Existing methods for parity detection are compared with the demonstration of a new method.

Zusammenfassung

Neue Technologien wie Quantencomputer und dazugehörige Netzwerke können genutzt werden, um sowohl bestimmte Berechnungsprobleme effizienter zu lösen, als auch um die Kommunikation zwischen Teilnehmern sicherer zu gestalten. Supraleitende Qubits haben sich als vielversprechende Plattform im Bereich des Computings etabliert, während Fehlstellen-Zentren mit Elementen der vierten Hauptgruppe für den Aufbau eines Quanteninternets im Rahmen der Kommunikation und des verteilten Quantenrechnens im Fokus aktueller Forschung stehen.

In dieser Arbeit zeigen wir die Charakterisierung und optimale Kontrolle elementarer Bausteine solcher Quantensysteme. Nach der Einleitung, widmet sich der erste Abschnitt der Charakterisierung und Simulation von Fehlstellen-Zentren mit Elementen der vierten Hauptgruppe, am Beispiel eines Germanium-Fehlstellen-Zentrums. Diese gelten als vielversprechende Kandidaten für einen Quantenrepeater.

Im zweiten Teil präsentieren wir Möglichkeiten zur effizienten Optimierung der Kontrolle von Quantensystemen. Hierzu vergleichen wir Optimierungsmethoden im Kontext nicht-gaußscher Rauschprozesse hinsichtlich Präzision und numerischem Aufwand. Ziel ist es, Dekohärenz in Quantensystemen besser zu verstehen und ihre Ursachen effektiv zu bekämpfen.

Im letzten Teil wird ein Experiment mit einem supraleitenden Qubit simuliert und charakterisiert. Dabei werden bestehende Methoden zur Paritätserkennung mit einem neuen Verfahren verglichen.

List of publications

Coherent Control of a Long-Lived Nuclear Memory Spin in a Germanium-Vacancy Multi-Qubit Node
Nick Grimm, Katharina Senkalla, Philipp J. Vetter, Jurek Frey, Prithvi Gundlapalli, Tommaso Calarco, Genko Genov, Matthias M. Müller, and Fedor Jelezko
Phys. Rev. Lett. 134, 043603 – Published 31 January, 2025
DOI: https://doi.org/10.1103/PhysRevLett.134.043603
Discussed here in Chapter 2.

Other Works

High-resolution spectroscopy of deterministically generated single photons from a single atom
Matthias Kreis, Konstantin Klein, Jurek Frey, Christian Haen, and Jürgen Eschner
Quantum Information and Measurement (pp. F5A-62) - Published on April 4th, 2019

Status of quantum computer development V2.0
Frank K. Wilhelm, Rainer Steinwandt, Daniel Zeuch, Jurek Frey
Update of the BSI-Study also written by Brandon Langenberg, Per J. Liebermann, Anette Messinger, Peter K. Schuhmacher, Aditi Misra-Spieldenner
BSI website — Published on November 13th, 2023

Contents

List of Figures

1. Introduction

We currently live in a time when sensors, secure communication and advanced computer algorithms increasingly shape our lives. The technological developments of the recent past made it possible to effectively monitor, interact and understand our environment. Here, quantum technologies such as quantum sensors, quantum networks, and quantum computers offer more precise measurements, secure communication protocols as well as quantum algorithms which scale (for some problems) better with input size.

While the idea of harvesting quantum properties for technological advances was already present in the 1980s [Fey82; Fey86; Wie83], it took time to establish the field. For example, vacancy centers have since their discovery in the late 1970s [DH76] evolved into promising candidates for nodes in quantum networks [Pom+21; Bha+20]. Important discoveries on that way were the clarification of the spin structure in nitrogen vacancy centers (NV) [OG89], optically-detected magnetic resonance (ODMR) measurements at room temperature [Gru+97], demonstration of long spin coherence [JW04], the use of the NV center as a qubit [WJ06] and as quantum sensors [Tay+08]. In the following years silicon vacancy centers (SiV) which offer a more narrow line width, reduced spectral diffusion and inversion symmetry were substantiated as a good alternative platform [Rog+14; Sip+16]. Lately, there happened a switch to other group IV centers (lead (PbV) [Wan+24], tin (SnV) [Iwa+17] and germanium (GeV) [Iwa+15]) which offer a strong zero phonon line and high optical stability.

Today, the computing technology is at the state of Noisy Intermediate-Scale Quantum (NISQ) computers, where systems with limited qubits face challenges such as environmental interference, scalability, and reliability. These devices offer the possibility for distributed computing through interconnected quantum networks, and thereby hopefully enabling fault-tolerant quantum computers.

Indicating what might be ahead of us was demonstrated by the Google group in their paper on "quantum error correction below the surface code" [Ach+24]. It showed that a quantum algorithm which ran on their device outperformed any classical computer, and it was estimated that the same computation would have taken ten septillion years [Nev24] on classical hardware. This demonstrates which otherwise impossible tasks can be made feasible by scaling up quantum technology. A good overview on the readiness for quantum technology in general is given in [Aws+25].

With this thesis, we want to contribute to the field by investigating challenges in

emulating quantum systems, concentrating on the noisy effects of the environment. Furthermore, we will show how system parameters can be efficiently estimated and how quantum control can be improved. The focus however will lie on understanding qubit characterization and the influence of Non-Gaussian noise processes, with the aim of reducing the gap between experimental capabilities and theoretical insights.

Structure

This thesis is organized as follows:

Chapter 1 introduces the concept of quantum systems, their emulation and that of a noisy environment. Furthermore, it establishes the idea of quantum states, fidelities, controllability, optimal control and the Weyl chamber. At the end, it gives an overview of the experimental platforms present in this work.

Chapter 2 concentrates on the coherent control of negatively charged group IV color centers in diamond. In these systems, very stable, but therefore also difficult to control nuclear spins are the target of operation. The chapter introduces the experimental setup, continues with showing how to emulate the system, how to characterize it and how to initialize the underlying spin system. It concludes by discussing speed and fidelity limitations.

Chapter 3 Covers the investigation of correlated noise and the integration of it into the optimization process. It addresses how to find robust control solutions which can be found even without prior knowledge about the structure of the noise disturbing the system.

Chapter 4 deals with the characterization of a superconducting nanowire experiment and discusses improvements in parity detection schemes. It covers in detail a derivation of the theoretical model and the emulation of noise in the system. Additionally, in the chapter we match experimental data to the theoretical model by adjusting system parameters and discuss single-qubit gate optimizations for parity detection schemes.

Chapter 5 summarizes the main findings of this thesis and shows how it advanced the research field in respect to qubit characterization, optimal control in noisy environments and noise modeling.

Appendix A contains a proof for the controllability of the GeV center and pseudocode for generating noise traces.

Appendix B contains a detailed discussion on how different time evolution methods for quantum systems are capable of governing driven dynamics under non-Gaussian noise processes. It concludes with a discussion on how Gaussian process noise sam-

pling is related to Lindblad master equations using the example of a spin-star system.

1.1. States, composite systems and density matrices

States

Quantum computing is based on the smallest quantum unit, the qubit. Opposite to classical bits, which can only take the discrete values 0 or 1, qubits are capable of being in any complex superposition of the two states $|0\rangle$ and $|1\rangle$. This is a phenomenon unique to quantum systems. In mathematical language, a qubit is described by an object $|\psi\rangle$ which lives in a two-dimensional Hilbert space $\mathcal{H}$. It can be written as the superposition of the underlying basis states

$$|\psi\rangle = a\,|0\rangle + b\,|1\rangle\,, \tag{1.1}$$

where $a, b \in \mathbb{C}$ are complex numbers which are characterizing the state of the qubit. Here, a and b fulfill the normalization condition $|a|^2 + |b|^2 = 1$ ensuring a probabilistic interpretation: If the qubit is measured in the computational basis (Z-basis), it leads to a collapse of the wave function $|\psi\rangle$ to either the state $|0\rangle$ with probability $|a|^2$ or to the state $|1\rangle$ with probability $|b|^2$.

Composite Systems

Quantum systems which contain multiple, possibly interacting, smaller quantum systems are characterized by the tensor product space of the respective systems. For instance, the Hilbert space of a two-qubit system $\mathcal{H}_{12}$ can be described by $\mathcal{H}_{12} = \mathcal{H}_1 \otimes \mathcal{H}_2$. Here, $\mathcal{H}_1$ and $\mathcal{H}_2$ are the Hilbert spaces of the individual qubits. The canonical basis for this composite system is:

$$\mathcal{B}_{12} = \{|0\rangle \otimes |0\rangle\,, |0\rangle \otimes |1\rangle\,, |1\rangle \otimes |0\rangle\,, |1\rangle \otimes |1\rangle\} = \{|00\rangle\,, |01\rangle\,, |10\rangle\,, |11\rangle\}. \tag{1.2}$$

Thus, any state $|\psi\rangle$ in $\mathcal{H}_{12}$ can be expressed as:

$$|\psi\rangle = \sum_{i,j\in\{0,1\}} c_{ij}\,|ij\rangle\,, \tag{1.3}$$

where $c_{ij} \in \mathbb{C}$ and normalization requires $\sum_{i,j\in\{0,1\}} |c_{ij}|^2 = 1$.

Composite systems introduce a second quantum phenomenon: *entanglement*. An entangled state is one which cannot be written as a tensor product of individual states. This means for example that the Bell state

$$|\Phi^+\rangle = \frac{1}{\sqrt{2}}(|00\rangle + |11\rangle) \neq (a_1\,|0\rangle + b_1\,|1\rangle) \otimes (a_2\,|0\rangle + b_2\,|1\rangle) \tag{1.4}$$

can not be written as a combination of individual states for arbitrary $a_k, b_k \in \mathbb{C}$.

Entanglement is the key resource for multi-qubit quantum systems because it expands the dimensionality of the space significantly and therefore provides computational and storing potential.

Density matrices

A more general approach to represent the information in a quantum system involves the use of mixed states. Since we normally do not possess full knowledge about the system's state, we have to acquire it over multiple measurements with classical outcomes. Thus, a formalism is required that encompasses both classical probability distributions and quantum information. For this purpose, we adopt the density matrix formalism.

A general density matrix ρ can be expressed as a linear combination of density operators $\rho_i = |\psi_i\rangle\langle\psi_i|$ which project onto the (orthogonal) pure state $|\psi_i\rangle$:

$$\rho = \sum_i p_i \, |\psi_i\rangle\langle\psi_i| \,, \tag{1.5}$$

where p_i is the probability that the system is in the state $|\psi_i\rangle$. In this context the expectation value of an operator A is given by:

$$\langle A\rangle = \sum_i p_i \, \langle\psi_i| \, A \, |\psi_i\rangle = \mathrm{Tr}(\rho A). \tag{1.6}$$

A density matrix possesses two important properties: it is positive semi-definite, meaning $\langle\psi| \, A \, |\psi\rangle \geq 0$ for all $|\psi\rangle \in \mathcal{H}$, implying it is Hermitian, and additionally it is normalized, such that $\mathrm{Tr}(\rho) = 1$. These two properties are both necessary and sufficient for any operator to be interpreted as a density matrix.

The purity is defined as $\gamma = \mathrm{Tr}(\rho^2) = \sum_i p_i^2 \leq 1$, with equality, if only one state is present in the ensemble. Any non-pure state is called mixed, and the purity shows how indecisive a measurement with the operators $|\psi_i\rangle\langle\psi_i|$ would be. Also, important to note is that a measurement can be used to purify the state. Further details can be found in [NC00].

1.2. Quantum Computing

At the core of quantum computing are quantum gates, which manipulate qubits in a reversible manner. Here, we introduce one- and two-qubit gates, which form the foundation of more complex quantum algorithms. These are the elementary parts in quantum circuits, similar to classical computing, where the fundamental logical functions like OR, AND, NOT etc. are used to implement more complex functions [Bar+95].

1.2.1. Single-Qubit Gates

Single-qubit gates perform unitary operations on a single qubit. Some essential single-qubit gates include the Hadamard Gate (H) which creates equal superposition if acting on a basis state, $H|0\rangle = \frac{|0\rangle+|1\rangle}{\sqrt{2}}$, where

$$H = \frac{1}{\sqrt{2}}\begin{bmatrix} 1 & 1 \\ 1 & -1 \end{bmatrix}, \tag{1.7}$$

the Pauli Gates (X, Y, Z) which equate to a quantum analog of classical bit or phase flip

$$X = \begin{bmatrix} 0 & 1 \\ 1 & 0 \end{bmatrix}, \qquad Y = \begin{bmatrix} 0 & -\mathrm{i} \\ \mathrm{i} & 0 \end{bmatrix}, \qquad Z = \begin{bmatrix} 1 & 0 \\ 0 & -1 \end{bmatrix} \tag{1.8}$$

and the Phase Gates (S, T) which apply specific phase shifts two the qubit

$$S = \begin{bmatrix} 1 & 0 \\ 0 & \mathrm{i} \end{bmatrix}, \qquad T = \begin{bmatrix} 1 & 0 \\ 0 & \mathrm{e}^{\mathrm{i}\pi/4} \end{bmatrix}. \tag{1.9}$$

Any single qubit gate $U \in SU(2)$ can be decomposed as

$$U = R_Z(\alpha)R_Y(\beta)R_Z(\gamma) \tag{1.10}$$

where $\alpha, \beta, \gamma \in \mathbb{R}$ and $R_K(\Theta) = \exp\left(-\mathrm{i}\frac{\Theta}{2}K\right), K \in \{X, Y, Z\}$.

However, the physical hardware might be limited to only a few basic operations. In this case, the Solovay-Kitaev theorem shows us that any single qubit gate $U \in SU(2)$ can be approximated astonishingly well by a sequence of few single qubit gates from a dense, generating set $\mathcal{G}$ (for example $\mathcal{G} = \{H, T\}$) [DN05].

1.2.2. Two-Qubit Gates

Two-qubit gates enable interaction between qubits and introduce quantum entanglement. The most prominent examples are the CNOT (Controlled-NOT) Gate which inverts the second (target) qubit if the first (control) qubit is in the state $|1\rangle$

$$\mathrm{CNOT} = \begin{bmatrix} 1 & 0 & 0 & 0 \\ 0 & 1 & 0 & 0 \\ 0 & 0 & 0 & 1 \\ 0 & 0 & 1 & 0 \end{bmatrix}. \tag{1.11}$$

The CNOT, H, and S generate the Clifford group. The Clifford group combined with the T gate forms a universal quantum gate set, meaning any unitary operation can be decomposed into a combination of these [For+15]. The next two interesting two-qubit gates are the SWAP Gate which switches two qubits

$$\text{SWAP} = \begin{bmatrix} 1 & 0 & 0 & 0 \\ 0 & 0 & 1 & 0 \\ 0 & 1 & 0 & 0 \\ 0 & 0 & 0 & 1 \end{bmatrix}, \tag{1.12}$$

and the Controlled-Phase (CZ) Gate which introduces similar to the CNOT a phase shift on the target qubit based on the control qubit's state

$$\text{CZ} = \begin{bmatrix} 1 & 0 & 0 & 0 \\ 0 & 1 & 0 & 0 \\ 0 & 0 & 1 & 0 \\ 0 & 0 & 0 & -1 \end{bmatrix}. \tag{1.13}$$

These gates need to be implemented as precisely as possible but for potential scaling at least below the error correction threshold to guarantee that an algorithm will result in the intended state most of the time [Bar+14].

1.3. Fidelity Measures

Quantifying the similarity between quantum states, operations, and channels, which are completely positive, trace preserving maps between density matrices, is a fundamental task in quantum information theory. Various fidelity measures have been developed to evaluate the distance between desired and achieved states, implemented and ideal quantum gates, and quantum channels. This section introduces the fidelity measures used in this work and discusses their relevance.

State Fidelity

The fidelity between two density matrices ρ_1 and ρ_2 is known to be written as [Uhl76]

$$F(\rho_1, \rho_2) = \left(\text{Tr}\left[\sqrt{\sqrt{\rho_1}\rho_2\sqrt{\rho_1}}\right]\right)^2. \tag{1.14}$$

This measure quantifies how close in a metric sense these two quantum objects are. It is motivated from classical probability theory, where the fidelity describes the similarity of two different probability distributions X, and Y. For single-qubit density matrices it simplifies to [Joz94]:

$$F(\rho_1, \rho_2) = \text{Tr}[\rho_1\rho_2] + 2\sqrt{\det(\rho_1)\det(\rho_2)} \tag{1.15}$$

and in the case of pure states to

$$F(\rho_{\psi_1}, \rho_{\psi_2}) = |\langle\psi_1|\psi_2\rangle|^2. \tag{1.16}$$

State fidelity is a widely used metric for assessing the quality of quantum state preparation, and is closely connected to the trace distance

$$\begin{aligned} D(\rho_1, \rho_2) &= \frac{1}{2}\|\rho_1 - \rho_2\|_1 \\ &= \frac{1}{2}\,\mathrm{Tr}\Big[\sqrt{(\rho_1 - \rho_2)^\dagger(\rho_1 - \rho_2)}\Big]. \end{aligned} \tag{1.17}$$

where $\|.\|_1$ is the trace norm and the connection is [FV02; BC94]

$$1 - \sqrt{F(\rho_1, \rho_2)} \leq D(\rho_1, \rho_2) \leq \sqrt{1 - F(\rho_1, \rho_2)}. \tag{1.18}$$

Unitary Fidelity

To compare unitary operations U_1, U_2 it is useful to introduce the unitary fidelity, which is inspired by the Frobenius norm. It is stated as:

$$F(U_1, U_2) = \frac{1}{d^2}\Big|\mathrm{Tr}\big[U_1 U_2^\dagger\big]\Big|^2, \tag{1.19}$$

where d is the Hilbert space dimension on which the unitaries are acting on.
It is independent of the involved density matrices and therefore provides a powerful measure for comparing gate performance.

Process and Average Gate Fidelity

The process fidelity F_p provides a more general fidelity measure. It is suitable to compare a non-unitary quantum channel $\mathcal{E}$ to a perfect unitary operation U. It is defined as:

$$F_p(U, \mathcal{E}) = \frac{1}{d^2}\sum_k \Big|\mathrm{Tr}\big[UV_k^\dagger\big]\Big|^2, \tag{1.20}$$

where $\{V_k\}$ are the Kraus operators of the quantum channel $\mathcal{E}$, that is $\mathcal{E}\rho = \sum_k V_k \rho V_k^\dagger$.
The average gate fidelity, closely related to the process fidelity, is writable as [Nie02]:

$$F_{\mathrm{aver}}(U, \mathcal{E}) = \frac{dF_p(U, \mathcal{E}) + 1}{d + 1}. \tag{1.21}$$

A main advantage is that the average gate fidelity allows us to compare noisy experimental data with theoretical implementations of quantum gates.

Diamond distance

A more general, mathematical tool to compare quantum channels is given by the diamond distance [AKN98]. For any two quantum channels $\mathcal{E}, \mathcal{F}$ it takes the form

$$d_\diamond(\mathcal{E}, \mathcal{F}) := \|\mathcal{E} - \mathcal{F}\|_\diamond = \max_\rho \|(\mathcal{E} \otimes \mathbb{1}_n)\rho - (\mathcal{F} \otimes \mathbb{1}_n)\rho\|_1. \tag{1.22}$$

The maximum is taken over all density matrices resident in the respective space and $\|.\|_1$ denotes the trace norm. It has the advantage that it can be calculated from the maps itself and therefore is a rigorous metric for characterizing noise and optimizing quantum protocols, independent of the initial density matrix ρ_0 [WS15; Lin+19].

Sanders et al. [SWS15] link the average gate fidelity to the true error rate and warn that a high average fidelity does not imply a low error rate. In there, it is argued that the diamond distance is the meaningful way two distinguish ideal and actual quantum channels. Furthermore, they also introduce the Pauli distance which gives deeper insight on the expected error rate and where the errors likely come from.

1.4. Emulating quantum systems

In order to understand the dynamics of a quantum system, we can use different techniques to model it. In this section, we will shortly recapitalize how interactions between subsystems are modeled and briefly discuss how we can classically emulate the time evolution. This section is inspired, and larger parts are taken from [Fre20].

1.4.1. Interaction between two systems

Interactions between quantum systems can be modeled by introducing operators that act either locally on individual systems or jointly across multiple systems. For two systems S_1 and S_2, local operators affect only their respective systems, while interaction operators act on both, encapsulating the coupling between the systems. The total Hamiltonian of such a composite system is given by:

$$H_{\text{tot}} = H_{S_1} \otimes \mathbb{1} + \mathbb{1} \otimes H_{S_2} + H_{\text{Int}}, \tag{1.23}$$

where H_{S_1} (H_{S_2}) consists of operators acting solely on S_1 (S_2), leaving the other system unaffected. The interaction Hamiltonian H_{Int} can generally be expressed as:

$$H_{\text{Int}} = \sum_{ij} A_1^i \otimes A_2^j, \tag{1.24}$$

where A_1^i and A_2^j are operators acting on S_1 and S_2, respectively.
S_1 is considered the observed quantum system (S), while S_2 represents a larger, unobservable environment or 'bath' (B). The bath often has a much higher dimensionality than the system, allowing information initially localized in S to dissipate into B. The

other way is also allowed, but in general more unlikely due to the different system sizes. Thereby, the effect of information becoming inaccessible or irretrievable in the larger bath system is called decoherence.

1.4.2. Time Evolution

The system's dynamics of a state $|\psi\rangle$ are described by Schrödinger's equation, which is (in natural units $\hbar = 1$ which we use for the rest of the thesis except stated otherwise) given by:

$$\mathrm{i}\frac{\partial}{\partial t}|\psi(t)\rangle = H(t)\,|\psi(t)\rangle\,, \tag{1.25}$$

where $H(t)$ is the time-dependent Hamiltonian describing the energy observable of the system at time t. This equation is formally solved by:

$$|\psi(t)\rangle = \mathcal{T}\exp\left(-i\int_{t_0}^{t} H(t')\mathrm{d}t'\right)|\psi(t_0)\rangle\,, \tag{1.26}$$

where $\mathcal{T}$ is the time-ordering operator and t_0 is the initial time. Here, the time-ordering can be omitted if the Hamiltonian commutes with itself at different times, i.e. $\forall t_1, t_2 \in [t_0, t]$ we have $[H(t_1), H(t_2)] = 0$.

The time evolution operator $U(t, t_0)$ is defined as:

$$U(t, t_0) = \mathcal{T}\exp\left(-i\int_{t_0}^{t} H(t')\mathrm{d}t'\right). \tag{1.27}$$

It is often very difficult or even impossible to obtain the exact unitary map analytically. However, it can be computed numerically via multiple methods. A simple but sufficient algorithm to achieve this is trotterization. In this algorithm we divide the evolution time in N steps of equal length Δt and approximate the time propagator as

$$U(t) = \prod_{j=1}^{N} U_j(t). \tag{1.28}$$

Here, the product is ordered such that U_1 is the first unitary acting on the initial state, and

$$U_j(t) = \exp\{-iH(t_0 + j\Delta t)\Delta t\}. \tag{1.29}$$

We keep this notation for the rest of the thesis.

For the more general case where we describe the system by a density matrix ρ, the Schrödinger equation can be used to derive the von Neumann equation:

$$i\frac{\partial}{\partial t}\rho = [H, \rho]. \tag{1.30}$$

The formal solution for the density matrix is

$$\rho(t) = U^{\dagger}(t, t_0)\rho(t_0)U(t, t_0). \tag{1.31}$$

It is often advantageous to move to a linearized version of the von-Neumann equation by using the vectorization map

$$\rho = \begin{pmatrix} \rho_{00} & \rho_{01} \\ \rho_{10} & \rho_{11} \end{pmatrix} \rightarrow \rho' = \begin{pmatrix} \rho_{00} \\ \rho_{01} \\ \rho_{10} \\ \rho_{11} \end{pmatrix}. \tag{1.32}$$

This trick allows us to rewrite Equation (1.30) as a first order linear differential equation

$$\dot{\rho}'(t) = \mathcal{L}(t)\rho'(t). \tag{1.33}$$

In the rest of this thesis we will omit the $'$ as it will be clear from the context which form is used. Furthermore, $\mathcal{L}(t)$ is the Liouville superoperator, which in this representation can be written as.

$$\mathcal{L}(t) = -\mathrm{i}\big[H(t) \otimes \mathbb{1} - \mathbb{1} \otimes H^T(t)\big]. \tag{1.34}$$

The formalism enables us to approximate a solution for the time-dependent Liouville equation by

$$\mathcal{U}(t) \approx \prod_{j=1}^{N} \exp\{-\mathrm{i}\mathcal{L}(t_0 + j\Delta t)\Delta t\}. \tag{1.35}$$

However, in many cases it is more advantageous to emulate the usual time propagator from Equation (1.28) and average over stochastic trajectories to get an estimate for the resulting quantum channel $\mathcal{E}$, i.e.

$$\mathcal{E}(t) = \frac{1}{N} \sum_{k=1}^{N} U^{(k)}(t) \otimes (U^{(k)})^*(t). \tag{1.36}$$

where $U^{(k)}$ is the unitary evolution resulting for a single realization. The dynamics of the observed system can thus be approximated by

$$\rho(t) = \mathcal{E}(t)\rho_0. \tag{1.37}$$

1.5. Noise characterization and modelling

In quantum computation, noise can be modeled by assuming that the properties of a noise process closely reflect those of the underlying experimental noise sources.

Various models and techniques have been developed to describe and analyze the decoherence of quantum systems, each offering unique insights into specific aspects of noise behavior. While early contributions established dynamical decoupling as a tool for quantum noise spectroscopy [VKL99; Cyw+08; AS11], there has been made much progress in the recent past. For instance, [Sun+21] introduced spin-locking quantum noise spectroscopy, which "extends the spectral range of weakly anharmonic qubit spectrometers", [Sun+21, p. 1] and [Vez+24] introduced Fourier Transform Noise Spectroscopy (FTNS). This method reduced the number of Laser pulses required for noise characterization, while [Lüp+20] introduced "a protocol for two-qubit dephasing noise spectroscopy" [Lüp+20, p.1]. It addressed correlated noise across multiple qubits. Additionally, [NPV16] introduced a method for quantifying higher order cumulants. In the following sections we will explore different noise models and focus on their respective limitations and advantages. More details on the effect of noise models can be found by the interested reader in [Kra+21] which is also what we follow in the next few sections (until subsection 1.5.5).

1.5.1. Unitary Errors

We start by dividing the Hamiltonian which describes our system of interest into two parts

$$H = H_c(t) + H_n(t) = \sum_k \alpha_k(t) C_k + \sum_l B_l(t). \tag{1.38}$$

Here, α_k are the control functions, C_k are the control operators and B_l are the noise operators acting on the system. Unitary errors are present if the applied control deviates from the intended one.
For example, in an experiment, the control line amplitude which is received by a qubit is differing from the wanted one or the drive frequency might be slightly off-resonant to the targeted frequency transition. For instance, in superconducting qubits, this might be the case if the applied voltage does not correspond to the effective coupling received by the qubit.

Unitary errors are strongly influenced by the specifics of the used platform. Thankfully, most of these errors can be mitigated by techniques like dynamical decoupling, composite pulses or other self-correcting mechanisms. This is due to the fact that most of the time such incorrect estimates of system or control parameters are consistent through repeated applications of the used pulses. However, Born's rule still applies, meaning the outcome of individual measurements will still be intrinsically probabilistic [CLJ03].

1.5.2. T_1 Decay

Longitudinal relaxation, due to noise acting along the quantization axis, leads to a decay with a characteristic decay time T_1 [Kra+21]. The environment thereby exchanges energy with the qubit system, which results in a relaxation (and sometimes

excitation) of the quantum system, such that the information on the qubit state is lost. Most of the time thermal fluctuations are the cause of this. This is also explaining why the excitation and relaxation processes are often considered Markovian, i.e. fast and memoryless. Therefore, the processes can be modeled as white Gaussian noise. It is characterized by a flat power spectrum, or equally by no correlation in time. Equivalently, these processes can be described quantum mechanically within the framework of a Lindblad master equation (LME),

$$\dot{\rho} = -i[H, \rho] + \Gamma_1 \mathcal{D}[\sigma_-]\rho, \tag{1.39}$$

where $\sigma_- = |0\rangle\langle 1|$ is the lowering operator, $\Gamma_1 = \frac{1}{T_1}$ is the decay rate and $\mathcal{D}[L]\rho = L\rho L^\dagger - \frac{1}{2}\{L^\dagger L, \rho\}$ denotes the Lindblad dissipator.

An experiment to measure T_1 typically involves preparing the qubit repeatedly in the excited state $|1\rangle$, waiting for a time t, and performing a readout measurement. The mentioned effects lead to an exponential decay of the probability of remaining in the exited state

$$P_{|1\rangle} = \exp(-\Gamma_1 t). \tag{1.40}$$

Here, the decay constant $\Gamma_1 = \frac{1}{T_1}$ is typically ranging from 40 µs for superconducting qubits to 200 s for qubits based on nuclear spin states [Abd+24; Hui+23]. Since the underlying noise is memoryless, it cannot be directly mitigated to reduce its effect on the system. However, error mitigation techniques can be applied, where measurement results are modified by artificially increasing the Gaussian noise component and then extrapolated in the opposite direction to estimate how results would appear in the absence of decay [Maj+23]. The underlying assumption here is that the measurements are performed at very low temperatures T, because else we have

$$\frac{\mathrm{d}P_{|1\rangle}}{\mathrm{d}t} = -\Gamma_\downarrow P_{|1\rangle} + \Gamma_\uparrow (1 - P_{|1\rangle}) \tag{1.41}$$

$$\tag{1.42}$$

where $\Gamma_\downarrow = \Gamma_0(\overline{n} + 1)$, $\Gamma_\uparrow = \Gamma_0 \overline{n}$,$\overline{n} = \left(\exp\left(\frac{\hbar\omega_q}{k_B T}\right) - 1\right)^{-1}$ is the thermal distribution of the bath and Γ_0 is the spontaneous decay rate at zero temperature. This would mean that the decay is shortened and only happens to the equilibrium population.

1.5.3. T_2 Decay

Another significant source of information loss is transverse relaxation, also known as dephasing, as it affects the phase of the qubit in the Bloch sphere representation. Dephasing arises due to the interaction of the qubit with its environment, leading to a loss of phase information. Unlike T_1 decay, the environmental effects causing T_2 decay are typically slow and require more complex modeling to account for memory effects, which happen because of information back-flow from the environment into the qubit system. The memory effects can also be thought of in terms of correlations of

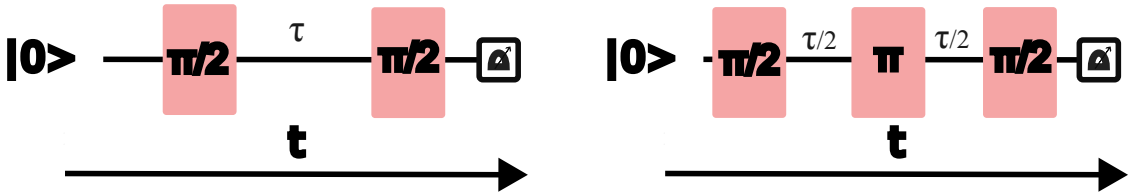

Figure 1.1.: Schematic of the Ramsey and echoed Ramsey sequences. Left: Standard Ramsey experiment. The qubit is initialized in $|0\rangle$, rotated to the equatorial plane of the Bloch sphere by a $\pi/2$ pulse, allowed to evolve freely for a time τ, and finally rotated to the exited state for measurement. Right: Echoed Ramsey sequence, identical to the standard Ramsey experiment but including a π refocusing pulse applied halfway through the free evolution.

information in time. These memory effects, referred to as non-Markovianity, complicate the emulation and modeling of the system, as the quantum state depends not only on its present state but also on its past states.
The standard procedure for characterizing dephasing is the Ramsey experiment (compare left part of Figure 1.1). In this experiment, the qubit is initialized in the ground state, followed by the application of a rotation $R_x(\frac{\pi}{2})$ to place the state on the equatorial plane of the Bloch sphere. After waiting for a time τ, another $R_x(\frac{\pi}{2})$ rotation is applied to bring the qubit into the excited state, and the qubit is subsequently read out. The observed decay in the Ramsey experiment can be described by:

$$P_{|1\rangle} = \exp(-\chi(\tau)), \tag{1.43}$$

where $\chi(\tau)$ is the decoherence function. In this case, both the transverse pure dephasing component T_ϕ and the longitudinal relaxation T_1 contribute to the overall decay.
If we assume that the dephasing noise can be modeled as white Gaussian noise process which acts on the transversal axis of the Bloch sphere, an assumption that is not always valid, the decay can be approximated as:

$$P_{|1\rangle}^{\text{Ramsey}} = \exp(-\Gamma_2 t), \tag{1.44}$$

where the decay constant Γ_2 is given by [NC00]:

$$\Gamma_2 = \frac{\Gamma_1}{2} + \Gamma_\phi, \tag{1.45}$$

and the factor 1/2 is coming from evaluating

$$\mathcal{D}(\rho) = \Gamma_1(\sigma_-\rho\sigma_+ - 1/2\{\sigma_+\sigma_-, \rho\}) \tag{1.46}$$

for ρ_{01}.

1.5.4. T_2^* and T_2^{Echo}

The combined dephasing time T_2^* describes the effective loss of coherence in a qubit system. Its value is typically extracted from Ramsey measurements and is influenced by both intrinsic noise and external factors, such as control field stability. By contrast, T_2^{Echo} is obtained using Hahn echo experiments (compare right part of Figure 1.1). It represents the intrinsic coherence time of the system after removing low-frequency noise contributions. In a Hahn echo sequence, a π pulse (a 90-degree rotation around Y) is applied midway during the free evolution time of a Ramsey measurement to refocus phase errors caused by slow environmental fluctuations. Improving both parameters is crucial for enhancing qubit performance in quantum computing applications.

1.5.5. Semi-Classical pure dephasing model

A full quantum mechanical treatment would assume that the environment can be described by a bath with a given bath-Hamiltonian and a given bath-system interaction. These systems are often described by Lindblad master equations, detailed derivations of those can be found for example in [BP02; GZ04; Wei12]. In such a picture, the bath correlations are given as

$$C_{kl}(t,t') = \mathrm{Tr}_B\{B_k(t)B_l(t')\rho_{SB}(t)\} \tag{1.47}$$

where $B_k(t)$ is an interaction operator and ρ_{SB} is the density matrix of the joint system [VMB24]. We see that this correlation function is in general not symmetric and not necessarily wide-sense stationary, i.e. the auto-covariance function can explicitly depend on time and not just on the time difference $t - t'$. However, it is enough to treat the system semi-classically, if the relevant operators commute or if the system is in a regime of large quantum numbers. Nevertheless, the correlation functions often resemble those of classical stochastic processes, and sometimes coherence has occurred sufficiently to render quantum noise effects negligible.
In the case of semi-classical dephasing for one qubit the Hamiltonian of the qubit in the rotating frame can be expressed as

$$H_k(t) = \beta_k(t)Z, \tag{1.48}$$

where β_k is the k-th realization of a random process. Any pure state $\rho_k(t)$ will evolve due to the von-Neumann equation $\dot{\rho}_k = -\mathrm{i}[H_k, \rho]$ which is formally solved by

$$\rho_k(t) = U_k\rho_0U_k^\dagger \tag{1.49}$$

where

$$U_k = \exp\left\{-\mathrm{i}\int_0^\tau \beta_k(t)\mathrm{d}tZ\right\} = \exp\{-\mathrm{i}\Phi_k(\tau)Z\}. \tag{1.50}$$

Here, we defined the accumulated phase $\Phi_k(\tau) = \int_0^\tau \beta_k(t)\mathrm{d}t$.

If we look at the evolution averaged over a large number of N noise realizations $\beta_k(t)$ we see that for an initial density matrix

$$\rho_0 = \frac{1}{2}(\mathbb{1} + X) \tag{1.51}$$

the dynamics are given as

$$\begin{aligned}\rho(\tau) &= \lim_{N\to\infty} \frac{1}{N} \sum_{k=1}^{N} \exp\{-\mathrm{i}\Phi_k(\tau)Z\}\rho_0 \exp\{\mathrm{i}\Phi_k(\tau)Z\} \\ &= \frac{1}{2}[\mathbb{1} + \langle\cos(2\Phi(\tau))\rangle X + \langle\sin(2\Phi(\tau))\rangle Y].\end{aligned} \tag{1.52}$$

This means for the respective expectation values

$$\langle X\rangle = \mathrm{Tr}(X\rho(\tau)) = \langle\cos(2\Phi(\tau))\rangle \tag{1.53}$$

and

$$\langle Y\rangle = \mathrm{Tr}(Y\rho(\tau)) = \langle\sin(2\Phi(\tau))\rangle\,. \tag{1.54}$$

If we look at the characteristic function $\varphi_{\Phi(\tau)}(z) = \langle\exp[\mathrm{i}z\Phi(\tau)]\rangle$ of the random process Φ we notice that

$$\begin{aligned}\varphi_{\Phi(\tau)}(z=2) &= \langle\exp\{\mathrm{i}\Phi(\tau)2\}\rangle \\ &= \langle\cos(2\Phi(\tau))\rangle + \mathrm{i}\langle\sin(2\Phi(\tau))\rangle \\ &= \langle X\rangle + \mathrm{i}\,\langle Y\rangle\,.\end{aligned} \tag{1.55}$$

This means we can, in the case of pure dephasing, use the characteristic function of a random process instead of averaging over realizations for describing the dynamics of a control free quantum system.

We will now shortly discuss different types of semi-classical noise:

Gaussian white noise dephasing

We start with the simplest case of pure dephasing which is white noise. For this kind of noise, the autocorrelation function reads

$$C(t,t') = \langle\beta(t)\beta(t')\rangle = \sigma^2\delta(t-t') \tag{1.56}$$

hence $\beta(t)$ is uncorrelated in time. This means, that for each time t, $\beta(t)$ is drawn from a normal distribution with zero mean and variance σ^2. This implicates that Φ is described by a Wiener process i.e.

$$\begin{aligned}\Phi(\tau) &= \sigma W_\tau \\ &\sim \mathcal{N}(0,\sigma^2\tau).\end{aligned} \tag{1.57}$$

The characteristic function is therefore given as that of a time-dependent normal distribution:

$$\varphi_{\Phi(\tau)}(z) = \exp\left(-\frac{1}{2}\sigma^2\tau z^2\right). \tag{1.58}$$

Hence, the decay function of a Ramsey experiment under pure white dephasing noise can be written as

$$\mathrm{Tr}\{\sigma_x\rho(\tau)\} = \varphi_{\Phi(\tau)}(2) = \exp\{-2\tau\sigma^2\}. \tag{1.59}$$

which would imply a dephasing rate of

$$\Gamma_2 = 2\sigma^2, \tag{1.60}$$

leading to a characteristic decay time of

$$T_2 = \frac{1}{\Gamma_2} = \frac{1}{2\sigma^2}. \tag{1.61}$$

Ornstein-Uhlenbeck (OU) process

The Ornstein–Uhlenbeck (OU) process is commonly used to model noise in spin systems [Fah+23], as it reproduces experimental observations with high accuracy. The fluctuations predominantly originate from the surrounding spin bath, where the dynamics of a few nearby spins induce small perturbations in the qubit frequency, leading to dephasing. A single noise trajectory is hereby given as a solution to the stochastic differential equation (SDE)

$$\mathrm{d}X_t = -\kappa X_t\,\mathrm{d}t + \sigma\,\mathrm{d}W_t \tag{1.62}$$

where W_t is the standard Wiener process. In the physics context, the SDE is sometimes written as a Langevin equation of the form

$$\frac{\mathrm{d}X_t}{\mathrm{d}t} = -\kappa X_t + \sigma\eta(t) \tag{1.63}$$

where $\eta(t)$ is Gaussian white noise, and represents an approximation of the nonexisting derivative of the Wiener process. If the random process starts with some initial value X_0 the solution of the above SDE reads

$$X_t = X_0\exp(-\kappa t) + \sigma\int_0^t \exp(k(s-t))\mathrm{d}W_s. \tag{1.64}$$

Here, we introduced the Itô-integral $\int_0^t f(t,s)\mathrm{d}W_s$. Its mean is zero and its variance is given by $\int_0^t (f(t,s))^2\mathrm{d}s$, i.e. if $Y = \int_0^\tau g(s)\mathrm{d}W_s$, then $Y \sim \mathcal{N}(0, \int_0^\tau g(s)^2)\mathrm{d}s)$. For the process to be wide-sense stationary, we have to choose $X_0 \sim \mathcal{N}(0, \frac{\sigma^2}{2\kappa})$ randomly

and independent of W_t. This implicates that the correlation function for this type of noise is given as

$$C^{OU}(t,s) = \frac{\sigma^2}{2\kappa}\exp\{-\kappa|t-s|\}. \tag{1.65}$$

The time integrated noise process Φ can be calculated using the Fubiny rule for Itô integrals, allowing us to interchange the integration order

$$\begin{aligned}
\Phi(\tau) &= \int_0^\tau X_t \mathrm{d}t \\
&= \int_0^\tau \left[X_0 \exp\{-\kappa t\} + \sigma \int_0^t \exp\{\kappa(s-t)\}\mathrm{d}W_s \right] \mathrm{d}t \\
&= X_0 \frac{1-\exp\{-\kappa\tau\}}{\kappa} + \sigma \int_0^\tau \int_s^\tau \exp\{\kappa(s-t)\}\mathrm{d}t\,\mathrm{d}W_s \\
&= \underbrace{X_0 \frac{1-\exp\{-\kappa\tau\}}{\kappa}}_{\sim \frac{1-\exp\{-\kappa\tau\}}{\kappa} N(0,\sigma^2)} + \underbrace{\sigma \int_0^\tau \frac{1-\exp\{\kappa(s-\tau)\}}{\kappa}\mathrm{d}W_s}_{\sim \sigma N(0, \int_0^\tau \left(\frac{1-\exp\{\kappa(s-t)\}}{\kappa}\right)^2 ds)} \\
&= \frac{1-\exp\{\kappa(s-t)\}}{\kappa} N(0, \frac{\sigma^2}{2\kappa}) + \sigma N(0, \frac{4\mathrm{e}^{-\kappa\tau} - \mathrm{e}^{-2\kappa\tau} + 2\kappa\tau - 3}{2\kappa^3}) \\
&= X_1(\tau) + X_2(\tau).
\end{aligned} \tag{1.66}$$

From this we can get the characteristic function of Φ since the characteristic function of the sum of two independent random variables is just the product of the individual characteristic functions such that

$$\begin{aligned}
\varphi_{\Phi(\tau)}(z) &= \exp\left(-\frac{\sigma^2}{4\kappa^3}(1-\exp(-\kappa\tau))^2 z^2\right) \exp\left(-\frac{\sigma^2}{2}\frac{4\mathrm{e}^{-\kappa\tau} - \mathrm{e}^{-2\kappa\tau} + 2\kappa\tau - 3}{2\kappa^3} z^2\right) \\
&= \exp\left(-\frac{\sigma^2 z^2}{2\kappa^3}(\mathrm{e}^{-\kappa\tau} + \kappa\tau - 1)\right) \overset{z=2}{=} \exp\left(-\frac{2\sigma^2}{\kappa^3}(\mathrm{e}^{-\kappa\tau} + \kappa\tau - 1)\right).
\end{aligned} \tag{1.67}$$

Squared Ornstein-Uhlenbeck process

Sometimes an environment does not interact linearly with the system. For example, in superconducting circuits the charge fluctuations interact quadratically with the system, this is why we consider the centered squared Ornstein-Uhlenbeck

$$Y_t = X_t^2 - \left\langle X_t^2 \right\rangle. \tag{1.68}$$

The correlation function can be calculated and is the same as that of an OU process with $\kappa' = \kappa/2$ and $\sigma' = \sqrt[4]{\frac{\sigma^2}{4\kappa}}$

$$C(t,s) = 2\sigma'^4 \exp\{-2\kappa'|t-s|\} \tag{1.69}$$

The characteristic function of the integrated process is given [KSK21] by

$$\phi_{\Phi(\tau)}(z) = \frac{e^{\frac{\kappa t}{2} - \frac{i\sigma^2 t}{\kappa}}}{\sqrt{\frac{(\kappa^2 - i\sigma^2 z)\sinh\left(\kappa t\sqrt{1-\frac{2i\sigma^2 z}{\kappa^2}}\right)}{\kappa^2\sqrt{1-\frac{2i\sigma^2 z}{\kappa^2}}} + \cosh\left(\kappa t\sqrt{1-\frac{2i\sigma^2 z}{\kappa^2}}\right)}}, \tag{1.70}$$

where the real part of the function is responsible for the decay and the imaginary part introduces oscillations in the expectation values over time. The oscillation can be interpreted as a Lamb shift.

Random telegraph process

A common reasoning for explaining 1/f noise in superconducting qubits is a collection of two level fluctuators (TLF) which interact with the qubit system. A noise trajectory is given as a signal which takes two values, $\pm g$ where a flip occurs randomly after a characteristic flip time $\tau = \frac{1}{\lambda}$. This random trajectory is also referred to as a symmetric Poisson process, since the probability of switching is equal for both values. Furthermore, it is a non-Gaussian noise process. The autocorrelation function for this stochastic process is given through,

$$C^{\mathrm{RTN}}(t,s) = g^2 \exp\{-2\lambda|t-s|\} \tag{1.71}$$

which is the same as for the OU process with $g = \sqrt{\frac{\sigma^2}{2\kappa}}$, $\lambda = \kappa/2$. However, the characteristic function looks quite different and is known to be [Fer06]

$$\varphi_{\Phi(t)(2)} = \begin{cases} e^{-\lambda t}\left(\frac{\lambda\sinh\left(t\sqrt{\lambda^2-4g^2}\right)}{\sqrt{\lambda^2-4g^2}} + \cosh\left(t\sqrt{\lambda^2-4g^2}\right)\right), & \lambda > 2g \\ e^{-\lambda t}(\lambda t + 1), & \lambda = 2g \\ e^{-\lambda t}\left(\frac{\lambda\sin\left(t\sqrt{4g^2-\lambda^2}\right)}{\sqrt{4g^2-\lambda^2}} + \cos\left(t\sqrt{4g^2-\lambda^2}\right)\right), & \lambda < 2g. \end{cases} \tag{1.72}$$

Multiple random telegraph noise processes

We notice that we get the characteristic function for multiple (independent) TLSs by using the properties of the characteristic functions:

$$\varphi_{a_1X_1+\cdots+a_nX_n}(z) = \varphi_{X_1}(a_1z)\cdots\varphi_{X_n}(a_nz). \tag{1.73}$$

Which means that the characteristic function of N TLSs with amplitudes $g_k = g/\sqrt{N}$ (to keep the spectral density the same), is given as

$$\varphi_{\Phi^{N\,\mathrm{RTNs}}}(t)(2) = \begin{cases} \left[\mathrm{e}^{-\lambda t}\left(\frac{\lambda \sinh\left(t\sqrt{\lambda^2-4g^2/N}\right)}{\sqrt{\lambda^2-4g^2}} + \cosh\left(t\sqrt{\lambda^2-4g^2/N}\right)\right)\right]^N, & \lambda > 2g/\sqrt{N} \\ \left[\mathrm{e}^{-\lambda t}(\lambda t+1)\right]^N, & \lambda = 2g/\sqrt{N} \\ \left[\mathrm{e}^{-\lambda t}\left(\frac{\lambda \sin\left(t\sqrt{4g^2/N-\lambda^2}\right)}{\sqrt{4g^2/N-\lambda^2}} + \cos\left(t\sqrt{4g^2/N-\lambda^2}\right)\right)\right]^N, & \lambda < 2g/\sqrt{N}. \end{cases} \tag{1.74}$$

Furthermore we see that for large N we will always find us in the case $\lambda > 2g/\sqrt{N}$ and we have

$$\lim_{N\to\infty}\left(\mathrm{e}^{-\lambda t}\left(\frac{\lambda \sinh\left(t\sqrt{\lambda^2-\frac{4g^2}{N}}\right)}{\sqrt{\lambda^2-\frac{4g^2}{N}}} + \cosh\left(t\sqrt{\lambda^2-\frac{4g^2}{N}}\right)\right)\right)^N = \mathrm{e}^{\frac{g^2\left(-2\lambda t-\mathrm{e}^{-2\lambda t}+1\right)}{\lambda^2}} \tag{1.75}$$

which is again the characteristic function of the Ornstein-Uhlenbeck process with $g = \sqrt{\frac{\sigma^2}{2\kappa}}$, $\lambda = \kappa/2$. This is not a coincidence but the central limit theorem at work. However, this also indicates that we can use the number of fluctuators N as a measure for the amount of Gaussianity given a certain spectral density. From a physical point of view, this indicates that the non-Gaussian effects of noise will only appear in systems where the environment has only few and strong interacting quantum systems surrounding the control system.

Comparing different noise models

Experimentally, it is often challenging to identify the precise origin of noise, the number of fluctuators interacting with the system, or their microscopic properties. In Appendix B, we investigate how different emulation methods are capable of showing this difference. Furthermore, we show how closely related stochastic description and Lindblad-like expansions really are. While our original goal was to use optimal control to increase the separation for different noise models, this seems to be very difficult since driving the system already decouples important information, but nevertheless lead to some interesting insights: Modeling non-Gaussian effects in driven environments is very difficult, but often not necessary. Since the drive already decouples many of these effects, secondly the two regimes where the noise is only slowly varying or constant and the very fast noise are connected, but the intermediate regime seems to offer no or very little room for improving experimental outcomes and adding more orders will capture the dynamics for longer times, but similar to fitting functions with polynomials it overshoots the solution when looked further. Here the proper solution would be probably something similar to spline interpolations.
In Figure 1.2 we show a comparison of the different noise models for a suited parameter range. We see that the random telegraph noise with N two level fluctuators

converges very quickly to the Gaussian case, indicating that "few" really means 1-3 nearby spins. What we also notice is that the non-Markovian behaviour is only observed in non-Gaussian environments. And since all processes displayed have the same spectral density, the observed dynamics allows us to distinguish noise effects coming from cumulants of order $m > 2$. While each individual process and its characteristic function can be found in the literature, a direct comparison of the four with identical spectral densities is, to the best of our knowledge, missing.

1.6. Controllability of quantum systems

An important question in quantum information is whether a given system is controllable. This is the case if every unitary transformation can be efficiently implemented on the quantum system up to arbitrary precision, i.e. if some infidelity measure (compare section 1.3) can be brought arbitrary close to zero. In a mathematical framework, we could formulate the problem as the following: Given a set of operators acting on a Hilbert space $\mathcal{H}$, namely $S_0 = \{A_1, A_2, \cdots, A_n\}$. What part of the Hilbert space is reachable with the given set of operators? And further: What assumptions do we need to satisfy for the decoherence times of the qubit system compared relative to the control capabilities of the system? To answer these questions, we refer the interested reader to the book [DAl07]. For the first question, we notice that the problem is related to the Lie-Algebra generated by the given operators that is defined as the span of continuously applying the commutator between the elements of the set. We define

$$S_k = \{[A_i, A_j] \,|\, \forall A_i, A_j \in S_{k-1}\} \cup S_{k-1}. \tag{1.76}$$

Then the Lie-closure of order k of S is given as

$$\mathcal{A}_S = \{S_k \,|\, k \text{ is the smallest natural number such that } S_{k+1} = S_k\}, \tag{1.77}$$

meaning that adding more commutators will not increase the size of the set anymore. We say that a system where the span of S_k is equal to the set of Hermitian, linear, and bounded operators $\mathcal{B}^\dagger : \mathcal{H} \to \mathcal{H}$ is fully controllable, i.e.

$$\mathcal{B}^\dagger(\mathcal{H}) = \langle S_n \rangle. \tag{1.78}$$

Simple Example

Let us consider the most simple case, where we have a single qubit with the following Hamiltonian:

$$H_1 = \frac{\omega_0}{2}\sigma_z + \Omega(t)\sigma_x, \tag{1.79}$$

where ω_0 is the qubit's energy splitting and $\Omega(t)$ is a time-dependent control field. The set of control operators here is, $S_0 = \{\sigma_z, \sigma_x\}$ and the Lie-closure is $\mathcal{A}_S = S_1 =$

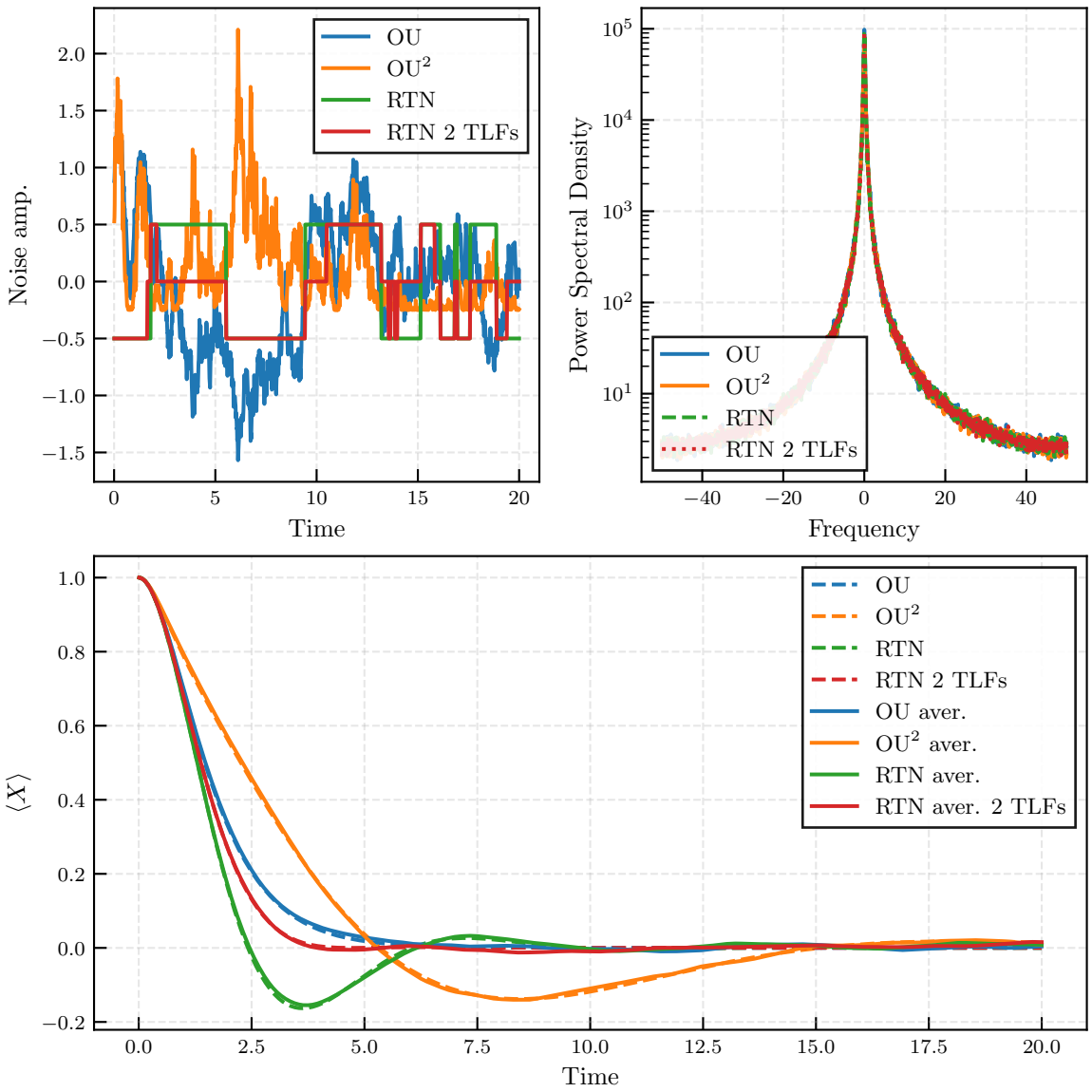

Figure 1.2.: Comparison of non-driven single qubit dynamics under different pure dephasing noise models. The blue lines correspond to an Ornstein-Uhlenbeck noise process, the orange curves to a squared Ornstein-Uhlenbeck process, the green curves to a single TLF and the red curves to a noise signal generated by two TLFs. Upper left: Single noise realizations amplitude over time, Upper right: power spectral density, which is the same for all of these noise types. Bottom: Time evolution of $\langle \sigma_x \rangle$. The solid lines correspond to evaluating the characteristic functions, while the dashed curves are averaged over $N = 10000$ noise realizations. The parameters of the noise were $\kappa = 1, \sigma = 0.5, g = \sqrt{\frac{\sigma^2}{2\kappa}}, \lambda = \frac{\kappa}{2}, \mathrm{d}t = 0.01$.

$\{\sigma_x, \sigma_y, \sigma_z\}$, since $[\sigma_z, \sigma_x] = \mathrm{i}\sigma_y$. Thus, if $\Omega(t)$ can be chosen freely, we are able to implement any single-qubit operation. If, on the other hand, the Hamiltonian takes the form

$$H = \Omega(t)\sigma_x + \Omega(t)\sigma_y \tag{1.80}$$

then the accessible set of operators is given by $\mathcal{A}_\mathcal{S} = S_0 = \{\sigma_x + \sigma_y\}$. In this case, the system would no longer be fully controllable.

1.7. Cartan decomposition

Local transformations are unitaries of the form

$$U_{\text{local}} = U_1 \otimes U_2, \tag{1.81}$$

where U_k act independently on the respective system. They do not affect the entanglement capabilities of a given gate. Any arbitrary gate U can be split into local and non-local parts [Wat+15], that is

$$U = e^{\mathrm{i}\alpha} k_1 A k_2. \tag{1.82}$$

Here, we have $k_1, k_2 \in \mathrm{SU}(2) \otimes \mathrm{SU}(2)$, $\alpha \in \mathbb{R}$ and

$$A = \exp\left\{-\frac{\mathrm{i}}{2}(c_1\sigma_x \otimes \sigma_x + c_2\sigma_y \otimes \sigma_y + c_3\sigma_z \otimes \sigma_z)\right\}. \tag{1.83}$$

With these definitions we arrive at several equivalent classes for the choice of the coordinates since many gates are equivalent up to local rotations. If we want to guarantee a unique set of coordinates for a given gate U we have to restrict the coordinates to the Weyl-chamber (compare Figure 1.3) that is [Wat+15]

$$0 \leq c_3 \leq c_2 \leq c_1 \leq \frac{\pi}{2}. \tag{1.84}$$

Here we follow [Wat+15] to implement an algorithm which calculates the matrix A from a given unitary U. We start by moving everything into the magic basis which is done with the matrix

$$Q = \frac{1}{\sqrt{2}} \begin{pmatrix} 1 & 0 & 0 & \mathrm{i} \\ 0 & \mathrm{i} & 1 & 0 \\ 0 & \mathrm{i} & -1 & 0 \\ 1 & 0 & 0 & -\mathrm{i} \end{pmatrix} \tag{1.85}$$

in this basis we define

$$U_B = Q^\dagger U Q \tag{1.86}$$

and from that

$$m = U_B^T U_B. \tag{1.87}$$

This gives us the three invariances

$$g_1 = \mathrm{Re}\left\{\frac{\mathrm{Tr}\{m\}^2}{16\det(U)}\right\} \tag{1.88}$$

$$g_2 = \mathrm{Im}\left\{\frac{\mathrm{Tr}\{m\}^2}{16\det(U)}\right\} \tag{1.89}$$

$$g_3 = \frac{\mathrm{Tr}(m)^2 - \mathrm{Tr}(m^2)}{4\det(U)}. \tag{1.90}$$

We numerically solve the polynomial equation

$$z^3 - g_3 z^2 + \left(4\sqrt{g_1^2 + g_2^2} - 1\right)z + g_3 - 4g_1 = 0. \tag{1.91}$$

The solutions z_1, z_2 and z_3 are related to the unordered Weyl coordinates via

$$\tilde{c}_j = \frac{1}{2}\arccos z_j. \tag{1.92}$$

The Weyl coordinates c_j are obtained by ordering $\tilde{c}_j$ by size. Given a physical system, with this it is sometimes easier to realize an equivalent two-qubit gate. Furthermore, we can use the theory to understand speed limits in the Germanium vacancy system (see section 2.11).

1.8. Optimal Control

Often, the respective multi-qubit systems is steered by several control lines. In terms of Hamiltonian, we add the control operators C_k with time dependent amplitude c_k to the system

$$H_c = \sum_{k=1}^{N} c_k(t) C_k. \tag{1.93}$$

The experimental implementation depends on the qubit system, for example in superconducting qubits these could be implemented over microwave signals transmitted via inductive or capacitive coupling [Tc24]. In photonic systems, state manipulation happens over phase plates and beam splitters, while in color centers the control includes both photonic and microwave manipulation implemented via lasers and a system of wires [CCK24].
To realize a gate-based quantum computer, it is necessary to implement the basic operations such as single and two-qubit gates with high precision. Optimal control tries to find control amplitudes $c_k(t)$ such that a given objective function such as the

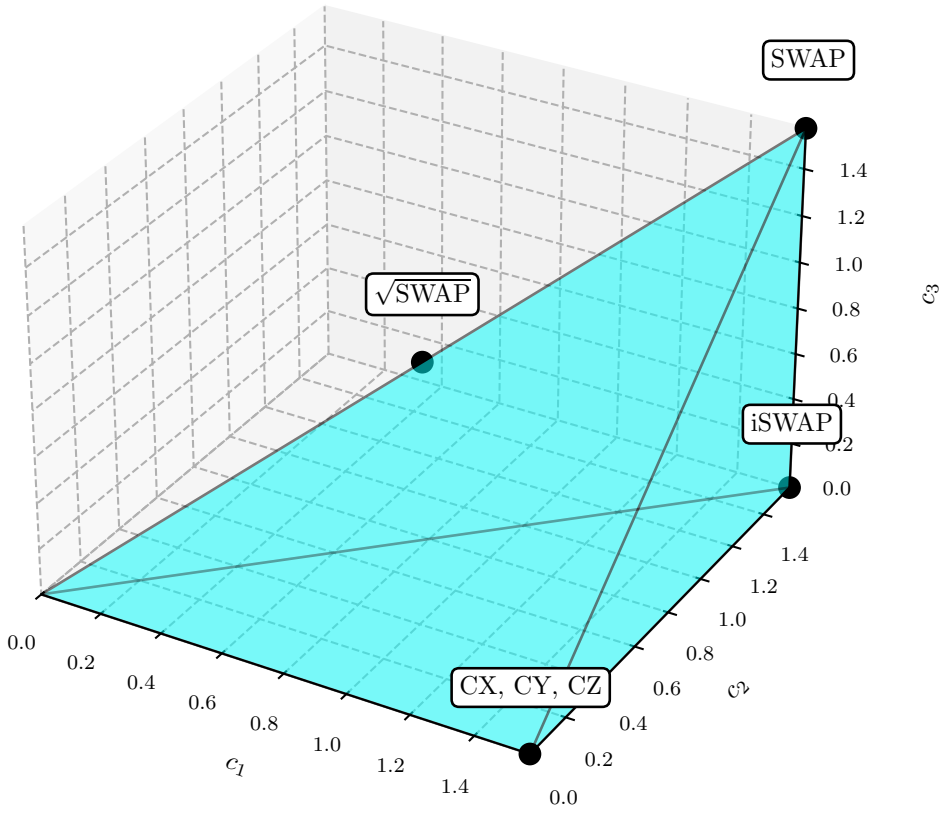

Figure 1.3.: Shown is the Weyl chamber, as the blue region, fulfilling Equation (1.84). The black dots show where a few two-qubit example gates are located. At $(\pi/2, 0, 0)$ are the controlled Pauli operations, at $(\pi/2, \pi/2, 0)$ we have the iSWAP operation which is a SWAP up to a phase on the diagonal entries, at $(\pi/4, \pi/4, \pi/4)$ is the $\sqrt{\text{SWAP}}$ operation which is halfway on the diagonal of the Weyl chamber, we need to apply it twice to reach the top corner of the Weyl chamber $(\pi/2, \pi/2, \pi/2)$ where the SWAP operation which swaps two qubits is located.

infidelity 1-F is minimized. All of this is needed because errors in quantum computers accumulate with the depth of the circuit and make the results unreliable. To fight these errors, there exists a bunch of techniques to mitigate and decouple some sorts of errors, however the main reason why large scale quantum processors could become reality is the existence of quantum error correction (QEC).
It is shown that the error rates for the gates in physical qubits need to surpass a certain threshold to make QEC work. Furthermore, additional reduction of physical gate errors reduce the number of required qubits [SR20]. To tackle this problem, the task of optimal control is to find for a given target operation $\mathcal{U}_{\text{target}}$ a good set of functions c_k which implement the required operation [Koc+22]. To measure the success probability of implementing such a task, one typically uses fidelity measures familiar from quantum control and information theory.
One of the main difficulties of optimal control, similar to machine learning, is to define a suited figure of merit (FoM) which should be optimized for. Also, it is not a priori clear how different constrains and which kind of functions have to be fulfilled by the control fields $c_k(t)$ [GWK15]. Once a parametrization for $c_k(t)$ is found, these parameters can be modified to reduce successively the FoM. To achieve this, different optimization algorithms have been developed. To name the most important ones: Krotov [MP19], which iteratively updates the control function sequentially in time to improve the figure of merit, GRAPE [Kha+05] which uses forward and backward propagation to compute gradients and updates the amplitudes for a piece-wise constant control and GOAT [Mac+15], which uses an analytic parametrization of control functions and integrates the time-evolution gradients into the optimization. For the update of the control function these algorithms use gradient-based methods like ADAM or LBFGS, which are used if there exists already some knowledge about the system's behavior or differentials [ASK19] and stochastic search algorithms like Nelder-Mead based methods or CMA-ES, which are the options if no gradient information is available [Sør+18]. We will use the dCRAB algorithm which we introduce in the next section.

1.8.1. The dCRAB algorithm

One possibility to parameterize and put in the pulse constraints is the use of the dCRAB algorithm [Mül+22]. We proceed according to the instructions specified therein. The algorithm expands the envelope functions (we omit the index k here) $c(t)$ in a basis $\{f_i\}_{i=1,\dots,N_c}$ such that the total envelope takes the form

$$c(t) = E(t) \sum_{i=1}^{N_c} c_i f_i(t) \tag{1.94}$$

where c_i are the coefficients of the respective basis functions and $E(t)$ is some general envelop function which can be used to enforce the pulse to start and end at zero amplitude.
The optimization of the parameters c_i can now be done by choosing a suited optimization algorithm. However, the arbitrary choice of N_c basis functions can lead to

additional artificial minima in the control landscape and further constrains the possible functions $c_k(t)$ to the part of the infinite dimensional space which is reachable with the set of basis functions $\{f_i\}_{i=1,\cdots,N_c}$. This can be addressed by introducing super-iterations $j = 1, \cdots, N$ such that in the j-th super iteration we optimize the coefficients c_i^j of

$$f^j(t) = c_0^j f^{j-1}(t) + \sum_{i=1}^{N_c} c_i^j f_i^j(t) \tag{1.95}$$

where $f^{j-1}(t)$ is the result of the optimization of the previous super iterations and $f_i^j(t)$ are new basis functions which are chosen such that they do not have a great overlap in the search space.

1.9. Superconducting Qubits

Among the various physical realizations of qubits, circuits involving superconducting elements have emerged as one of the most advanced platforms due to their scalability, rapid gate operations, and strong interaction with microwave photons [CW08]. These artificial atoms, based on Josephson junctions, allow for precise quantum control and integration with classical electronic systems.

Unlike naturally occurring two-level systems, superconducting qubits are tunable in their frequency and coupling. This is mainly because the nonlinearity introduced by the Josephson effect enables anharmonic energy levels, allowing the isolation of two levels for qubit operations. The superconducting qubits are affected by charge noise, flux noise, and dielectric losses, leading to a limited coherence time of about $T_2 \approx 100\,\text{ns}$. There are two main circuit designs, each of which we will briefly discuss here. More details on the different types of superconducting qubits can be found here [Bun25] and in chapter 4 of this thesis.

1.9.1. Flux based qubits

The flux qubit derived architectures encode quantum information in circular supercurrents, where the direction encodes the qubit's basis states. Flux qubits have a high connectivity and are heavily used for quantum annealing. However, since the non-classic part highly depends on the tunneling coupling and is exponential in the fabrication parameters [Bun25] it is hard to reproduce good flux qubits and hence the platform is not very scalable.

1.9.2. Charge based qubits

Charge based qubits use the charge states as basis states, meaning the presence of excess Cooper pairs on the metallic electrode. Charge based qubits have the advantage that they are less sensitive to flux noise, which results in longer coherence times. The

transmon additionally reduces the amount of charge noise disturbing the system, such that it shields the qubit successively from the main sources of environmental noise. Further details can be found in [Kra+21].

1.10. Vacancy color center qubits

Vacancy center qubits use the spin states of a central electronic spin system as a qubit, while "surrounding nuclear spins could provide a range of functionalities such as acting as long-lived resources for information storage, deterministic entanglement, and error correction" [Gun+25, p.1]. They stand out because of "efficient photonic interfaces [...], coherence times up to seconds for electronic spins and minutes for nuclear spins, and solid-state hosts that are amenable to on-chip integration with semiconductor electrical and photonic circuits" [Aws+25, p. 3]. While they are promising candidates for quantum nodes, the number of qubits per node is very limited and hard to control [Gun+25]. Nevertheless, the platform is offering solid-state robustness with high-coherence, even at room temperature, leading to practical application in sensing and communication.

1.10.1. Nitrogen-vacancy center

Nitrogen-vacancy (NV) centers are build by substituting a nitrogen atom for a carbon atom in the diamond lattice, which leads to an adjoined vacancy. Additionally, the local defect is transformed into a NV^- state, which can be done by shifting the Fermi energy level with an external voltage. The resulting defect behaves as an electronic spin-1 system which can be initialized, manipulated and read out optically by the use of tailored laser systems. A good review on such a system is given in [Rem+20].

The Hamiltonian of the charged spin system can be written as [Sch+14; Rem+20]

$$H = D\left(S_z^2 - \frac{2}{3}\right) + \gamma_e \mathbf{B}\cdot\mathbf{S} + H_{\text{strain}} + H_{el} + H_{\text{hf}} \tag{1.96}$$

where D is the zero field splitting due to spin-spin interactions, $\mathbf{S} = (S_x, S_y, S_z)^T$ is the vector of spin operators, γ_e is the electron's gyromagnetic ratio, $\mathbf{B}$ is the external magnetic field, H_{el} accounts for electric interactions, H_{strain} for crystal strain effect and H_{hf} represents hyperfine interactions with the ^{14}N and or surrounding ^{13}C nuclear spins, the nuclear Zeeman interactions and the nuclear quadrupole interactions.

The spin-triplet ground state $|m_S = 0\rangle$ and $|m_S = \pm 1\rangle$ can be coherently manipulated using microwave fields that drive transitions between $|m_S = 0\rangle$ and $|m_S = +1\rangle$, and $|m_S = 0\rangle$ and $|m_S = -1\rangle$, while readout and initialization can be done optically. If the system is viewed as a qubit, where $|-1\rangle$ and $|0\rangle$ are interpreted as the common ground

state and $|1\rangle$ as the excited state, NV-centers can reach exceptional coherence times with T_2^* exceeding 100 µs [Her+19]. Using dynamical decoupling, this can be pushed to $T_2 \approx 0.6\,\mathrm{s}$ at cryogenic temperatures (77K) [Bar+13].

1.10.2. Germanium-vacancy center

Germanium-vacancy (GeV) centers in diamond belong to the class of group-IV vacancy centers, which caught scientific interest in the recent past [Iwa+15; HE24]. It consists of a germanium atom occupying an interstitial position between two adjacent vacancies, forming a split-vacancy configuration [Bra+19]. This symmetric structure results in reduced susceptibility to electric field noise and therefore enhanced optical properties, especially the strong zero-phonon line (ZPL) [Iwa+15]. Furthermore, the level structure of the spin orbits in this case is a doublet state.

While NV centers are widely used in quantum sensing, group IV vacancy centers such as SiV, GeV and SnV provide a higher optical coherence since the ZPL improves photon indistinguishability and allows for faster optical cycling, which leads to improved initialization and readout quality and duration [Bra+19]. However, GeV centers typically have decreased spin coherence times than NV centers, due to enhanced electron-phonon interactions [Bar+20] and because of their spin-1/2 rather than spin-1 ground state. This makes them less suitable for quantum memory but ideal for fast, optically mediated quantum gates and photonic quantum networks [Sen+24; Gri+25; Bra+19].

2. Optimal Microwave Control of a Multi-Qubit Germanium-Vacancy Node

2.1. Preface

This chapter relates to the publication [Gri+25] and its supplemental material, larger parts of this chapter contain information and formulations from there. While the experiment was done by the coauthors, the optimal control part was exclusively done by the author. The content of gate optimization onwards (subsection 2.8.2) goes beyond the scope of the paper. Two more publications from J.Frey et al. related to this are in preparation.

2.2. Motivation

Quantum computation and communication require the achievement of multiple technological and physical milestones. One of them is building a reliable repeater node, which can store quantum information for long timescales compared to the computational operations. Group-IV color centers in diamond serve as promising candidates, since the electronic spin of these systems have a coherent spin-photon interaction, which can be harvested to exchange quantum information between far distant systems via connection over optical fibers. One such spin system is a Germanium vacancy center, surrounded by ^{13}C carbon atoms. Ultimately, these nuclear spins should be used as storage for quantum information, since they naturally have great shielding of decoherence, allowing for coherent operation and long memory times of up to $T_2^* = 2.57\,\mathrm{s}$ [Gri+25]. These have a nuclear spin which interacts with the spin of the vacancy via Zeeman interactions. This in combination with optimal control allows us to manipulate the nuclear spin indirectly via the electron spin. This was first investigated in this thesis.
The goal of this chapter is to show how an experimental setup [Gri+25; Sen+24], can be described in a mathematical framework which explains the main features of the measurements done in a real world experiment. Furthermore, we want to show how to operate the system in such a way that we can efficiently transfer information from the spin of the vacancy to a surrounding nuclear spin and vice versa.

2.3. The experimental setup

In the experiment, a negatively charged GeV-center which is strongly coupled to a nearby nuclear spin is located in a diamond sample. A system of lenses combined with laser pulses are used for optical initialization and readout. The system is coupled to the control via copper wires which act as microwave antennas and incorporate the control lines. The sample is placed inside the magnetic field generated by vector magnet, which produces a variable magnetic field. The whole system is operated inside a dilution fridge, which cools down the system to a temperature of $T \approx 4\,\mathrm{K}$. A more detailed description of the experimental setup can be found in [Gri+25] and its supplementary material.

2.4. The model

We model the experimental system as an effective two-qubit spin system, which are coupled to each other due to Zeeman-interactions. In the following sections, we will call the spin of the negatively charged vacancy the electron spin and refer to the strongly coupled $^{13}\mathrm{C}$ system as the nuclear spin.

2.4.1. Static Hamiltonian

We model the two-qubit spin system, by a relatively simple model which describes both electron spin and nuclear spin as two-level systems, where $|\uparrow\rangle \hat{=} |0\rangle$ and $|\downarrow\rangle \hat{=} |1\rangle$. The static Hamiltonian in this context can be written in natural units($\hbar = 1$) as

$$H_0 = -\frac{\gamma_e B_z}{2}\sigma_z \otimes \mathbb{1} \tag{2.1}$$

$$-\frac{\gamma_n B_z}{2}\mathbb{1} \otimes \sigma_z \tag{2.2}$$

$$+\frac{1}{4}\sum_{i=x,y,z} A_{zi}\sigma_z \otimes \sigma_i, \tag{2.3}$$

where B_z, is the z-component of the magnetic field at the color center, γ_e and γ_n are the gyro-magnetic ratios of the Germanium vacancy and the nuclear spin and A_{zi} are tensors describing the coupling between the two systems. Furthermore, we can always define our frame of reference such that there is no A_{zy} contribution. In section 2.5 we try to extract the parameters directly from experimental data. Due to a non-Zero A_{zx} coupling, the Hamiltonian is not diagonal, and we rewrite it in the energy eigenbasis to get the transition frequencies between the energy levels. The four eigenvalues of the Hamiltonian are

$$\epsilon_{\pm\pm} = \frac{1}{4}\Big(\pm 2\gamma_e B \pm \sqrt{A_{zx}^2 + (A_{zz} - 2\gamma_n B)^2}\Big) \tag{2.4}$$

and they are related to eigenenergies over

$$\begin{aligned} \mathrm{MW1} &= \epsilon_{++} - \epsilon_{--} \\ \mathrm{MW2} &= \epsilon_{+-} - \epsilon_{-+} \\ \mathrm{RF1} &= \epsilon_{-+} - \epsilon_{--} \\ \mathrm{RF2} &= \epsilon_{++} - \epsilon_{+-}. \end{aligned} \tag{2.5}$$

Figure 2.1 illustrates the level structure related to the eigenenergies $\epsilon_{\pm\pm}$. The indicated microwave (MW) and radio-frequency (RF) transitions are given by the corresponding energy splittings between eigenstates, as in Equation (2.5). The respective normalized eigenvectors are thereby given through

$$v_1 = \begin{pmatrix} 1 \\ 0 \end{pmatrix} \otimes \frac{1}{\sqrt{1 + c_{--}^2}} \begin{pmatrix} c-- \\ 1 \end{pmatrix} \tag{2.6}$$

$$v_2 = \begin{pmatrix} 1 \\ 0 \end{pmatrix} \otimes \frac{1}{\sqrt{1 + c_{-+}^2}} \begin{pmatrix} c_{-+} \\ 1 \end{pmatrix} \tag{2.7}$$

$$v_3 = \begin{pmatrix} 0 \\ 1 \end{pmatrix} \otimes \frac{1}{\sqrt{1 + c_{+-}^2}} \begin{pmatrix} c_{+-} \\ 1 \end{pmatrix} \tag{2.8}$$

$$v_4 = \begin{pmatrix} 0 \\ 1 \end{pmatrix} \otimes \frac{1}{\sqrt{1 + c_{++}^2}} \begin{pmatrix} c_{++} \\ 1 \end{pmatrix}, \tag{2.9}$$

$$\tag{2.10}$$

where

$$c_{\pm\pm} = \frac{A_{zz} \pm 2\gamma_n B \pm \sqrt{A_{zx}^2 + (A_{zz} - 2\gamma_n B)^2}}{A_{zx}}. \tag{2.11}$$

We notice that the nuclear spin states depend now on the electron spin state. This means that if we prepare the state in one of the computational basis states we observe oscillations on the nuclear spin state and the strength of the oscillation depends on the electron spin state. However, the eigenstates are still product states, where the main difference is now that the nuclear spin has different eigenstates depending on the electron spin.
We further define the vectors

$$\tilde{v}_1 = v_1 \tag{2.12}$$

$$\tilde{v}_2 = v_2 \tag{2.13}$$

$$\tilde{v}_3 = (\sigma_x \otimes \mathbb{1}) v_1 \tag{2.14}$$

$$\tilde{v}_4 = (\sigma_x \otimes \mathbb{1}) v_2 \tag{2.15}$$

which we can use to characterize the polarization along the quantization axis if the electron is in the down-state.

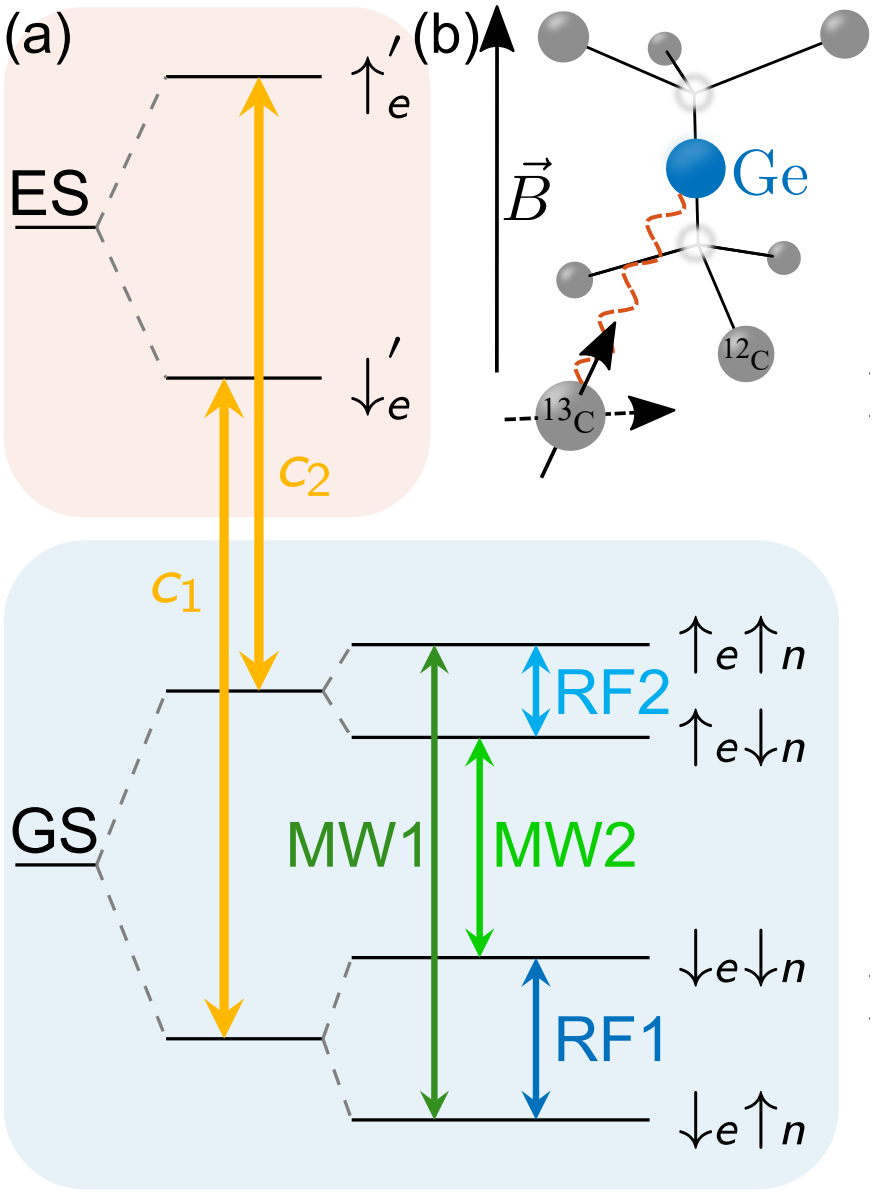

Figure 2.1.: a) Reduced level structure of the system. The simulation only refers to the light blue part of the figure. The laser transitions c_1 and c_2 are used to optically (re-) initialize the electron spin. b) Schematic of GeV aligned with external magnetic field, showing electron spin-state-dependent nuclear spin quantization axis (adapted from [Gri+25], © American Physical Society).

2.4.2. Drive Hamiltonian

The drive Hamiltonian in our model can be described via:

$$H_D = \Xi_{MW}(t)\sigma_x \otimes \mathbb{1} + \Xi_{RF}(t)\mathbb{1} \otimes \sigma_x. \tag{2.16}$$

We assume the driving fields have the form

$$\Xi_k = \Omega_k(t)\cos(\omega_k t - \phi), \quad k \in \{\text{MW, RF}\}, \tag{2.17}$$

where $\Omega_k(t)$ is the time-dependent Rabi frequency of the drive and is set to a constant value for simple pulses, ω_k is its frequency and ϕ is its phase which we set to $\phi = 0$ until further notice.
The amplitudes of the respective drives are here experimentally limited to $\Omega_{MW} \leq 2\pi \times 12\,\text{MHz}$ and $\Omega_{RF} \leq 2\pi \times 50\,\text{kHz}$.
The envelope function $\Omega_k(t)$ will later be modified to allow for gate and population transfer optimizations. To further improve the fidelity of those operations, it might also be useful to define more than two drive lines at a time in order to allow for driving all possible transitions apparent in the qubit both resonant and off-resonant at the same time.

2.4.3. Controllability

The total Hamiltonian of the system is now given as

$$\begin{aligned} H &= H_0 + H_D && (2.18)\\ &= -\frac{\gamma_e B_z}{2}\sigma_z \otimes \mathbb{1} && (2.19)\\ &\quad - \frac{\gamma_n B_z}{2}\mathbb{1} \otimes \sigma_z && (2.20)\\ &\quad + \frac{1}{4}\sum_{i=x,z} A_{zi}\sigma_z \otimes \sigma_i && (2.21)\\ &\quad + \Xi_{MW}(t)\sigma_x \otimes \mathbb{1} && (2.22)\\ &\quad + \Xi_{RF}(t)\mathbb{1} \otimes \sigma_x. && (2.23) \end{aligned}$$

With this, the control operator set has three independent elements,

$$S = \{H_0, \sigma_x \otimes \mathbb{1}, \mathbb{1} \otimes \sigma_x\}. \tag{2.24}$$

According to the methods introduced in section 1.6, the system is fully controllable if there are no constraints on the driving fields. An interesting observation is that even the Lie closure of the set without the drive on the nuclear spin already spans the entire space of two-qubit operations, $\mathfrak{su}(4)$. This implies that slow RF control is not required to efficiently control the nuclear spin qubit (see Appendix A.1 for a detailed proof).

2.4.4. Rotating frame

We now transform the system to a frame which is rotating at the drive frequency, $\omega_d = \omega_e + \Delta$ i.e.

$$R = \exp\left\{-\mathrm{i}\frac{\omega_d t}{2}\sigma_z \otimes \mathbb{1}\right\}, \tag{2.25}$$

where Δ is the detuning to the electron transition frequency when there would be no interactions present. The static Hamiltonian (because $\sigma_z \otimes \mathbb{1}$ commutes with the static Hamiltonian) changes in the rotating frame to

$$H'(t) = \mathrm{i}\dot{R}(t)R^\dagger(t) + R(t)H(t)R(t)^\dagger \tag{2.26}$$

$$= \frac{\Delta}{2}\sigma_z \otimes \mathbb{1} - \frac{\gamma_n B}{2}\mathbb{1} \otimes \sigma_z \tag{2.27}$$

$$+ \sum_{i=x,y,z} A_{zi}\sigma_z \otimes \sigma_i \tag{2.28}$$

However, the MW drive Hamiltonian does not commute with the frame transformation, and we get for the rotating drive term

$$H'_D = \Xi_{MW}(t)\begin{pmatrix} 0 & \mathrm{e}^{-\mathrm{i}\omega_d t} \\ \mathrm{e}^{\mathrm{i}\omega_d t} & 0 \end{pmatrix} \otimes \mathbb{1} + \Xi_{RF}(t)\mathbb{1} \otimes \sigma_x \tag{2.29}$$

instead.
If we now assume that our drive frequency is close to the electron transition, we can use the rotating wave approximation (RWA) and get

$$H'_D = \Omega_{MW}(t)\cos(\omega_d t - \phi_{MW})\begin{pmatrix} 0 & \mathrm{e}^{-\mathrm{i}\omega_d t} \\ \mathrm{e}^{\mathrm{i}\omega_d t} & 0 \end{pmatrix} \otimes \mathbb{1} + \Xi_{RF}(t)\mathbb{1} \otimes \sigma_x \tag{2.30}$$

$$= \frac{\Omega_{MW}(t)}{2}\begin{pmatrix} 0 & \mathrm{e}^{-\mathrm{i}\phi_{MW}} + \mathrm{e}^{-2\mathrm{i}\omega_d t + \mathrm{i}\phi_{MW}} \\ \mathrm{e}^{\mathrm{i}\phi_{MW}} + \mathrm{e}^{2\mathrm{i}\omega_d t - \mathrm{i}\phi_{MW}} & 0 \end{pmatrix} \otimes \mathbb{1} + \Xi_{RF}(t)\mathbb{1} \otimes \sigma_x \tag{2.31}$$

$$\overset{\text{RWA}}{\approx} \frac{\Omega_{MW}(t)}{2}\begin{pmatrix} 0 & \mathrm{e}^{-\mathrm{i}\phi_{MW}} \\ \mathrm{e}^{\mathrm{i}\phi_{MW}} & 0 \end{pmatrix} \otimes \mathbb{1} + \Xi_{RF}(t)\mathbb{1} \otimes \sigma_x \tag{2.32}$$

$$= \frac{\Omega_{MW}(t)}{2}\left[\cos(\phi_{MW})\,\sigma_x \otimes \mathbb{1} + \sin(\phi_{MW})\,\sigma_y \otimes \mathbb{1}\right] + \Xi_{RF}(t)\mathbb{1} \otimes \sigma_x \tag{2.33}$$

$$= \Omega_X(t)\,\sigma_x \otimes \mathbb{1} + \Omega_Y(t)\,\sigma_y \otimes \mathbb{1} + \Xi_{RF}(t)\mathbb{1} \otimes \sigma_x. \tag{2.34}$$

2.5. System characterization

There are many different schedules and experiments which can be done to characterize the system. The most common ones which were also performed in the related

Parameter	Measured value
$T^{*}_{2,\mathrm{RF1}}$	$(2.00 \pm 0.18)\,\mathrm{ms}$
$T^{\mathrm{Hahn}}_{2,\mathrm{RF1}}$	$(274 \pm 16)\,\mathrm{ms}$
$T^{\mathrm{XY8}}_{2,\mathrm{RF1}}$	$(1.49 \pm 0.10)\,\mathrm{s}$
$T^{\mathrm{CPMG8}}_{2,\mathrm{RF1}}$	$(1.36 \pm 0.14)\,\mathrm{s}$
$T^{\mathrm{CPMG16}}_{2,\mathrm{RF1}}$	$(2.57 \pm 0.19)\,\mathrm{s}$
T^{mem}_{2}	$18.1\,\mathrm{s}$

Parameter	Measured value
$T^{4K}_{1,e}$	$(3.41 \pm 0.20)\,\mathrm{ms}$
$T_{1,\lvert\downarrow_e\rangle}$	$(20.7 \pm 2.0)\,\mathrm{s}$
$T^{*}_{2,e}$	$1.43\,\mu\mathrm{s}$
$T^{\mathrm{Hahn}}_{2,e}$	$440\,\mu\mathrm{s}$
$T^{\mathrm{CPMG}}_{2,e}$	$(24.1 \pm 0.9)\,\mathrm{ms}$
$T^{\mathrm{XY8}}_{2,e}$	$(18 \pm 3)\,\mathrm{ms}$

Table 2.1.: Nuclear (left) and electron (right) spin coherence times, T^{mem}_{2} is a realistic estimate for an achievable memory time. The numbers are taken from [Gri+25] and [Sen+24].

experiment will be introduced and explained shortly in this section. We keep in mind that all readouts are done optically on the electron spin. The initialization fidelity in the upstate $|\uparrow_e\rangle$ here is 98 % [Gri+25]. Since the nuclear spin state has such a long coherence time, it is also very difficult to read it out directly. What is done instead is to transfer the information of the nuclear spin state to the electron spin and read this out instead.

T_1 and T_2 measurements

To measure the average lifetime of a qubit, we usually characterize it with two different decay times, i.e. T_1 and T_2. The first one describes how long the information of being in the excited state is preserved. In the related experiment, a coherence time of $T_{1,e} = (20.7 \pm 2.0)\,\mathrm{s}$ [Gri+25] was measured. The second time T_2 characterizes how long the phase information of a qubit is conserved. For this, one does a Ramsey experiment. I.e. if we apply a $\frac{\pi_x}{2}$-pulse, wait for a time τ, apply another $\frac{\pi_x}{2}$-pulse and measure the qubit, we can say something about the lifetime of a transverse spin state. In the experiment, $T^{*}_{2,e} = 1.43\,\mu\mathrm{s}$ [Gri+25] was observed. Another important information is how much of the measured dephasing noise can be decoupled by the use of decoupling sequences like CPMG or XY-sequences. Here, the application of well-timed π-pulses is used to remove the part of the noise which has some memory effect. This is possible because a single π-pulse inverts the phase accumulation direction. In the experiment, it was concluded that the highest achievable memory time for a transverse electron spin state is $T_{2,e} = 440\,\mu\mathrm{s}$ [Sen+24]. The same measurements can be done for the nuclear subspace, and the experimentally measured values are summarized in Table 2.1.
We conclude that the most important source of noise is dephasing noise, which is present on the electron. It is so strong compared to the other noise sources that we can in good approximation ignore the other noise sources for our simulation. We

further saw that the noise has a high memory component, since dynamical decoupling techniques showed that $T_{2,e} \gg T_{2,e}^*$. To incorporate this into our model, we add semi-classical pure dephasing noise on the electron qubit Hamiltonian to our model

$$H_{\text{noise}} = \beta(t)\sigma_z \otimes \mathbb{1} \tag{2.35}$$

where $\beta(t)$ is a random field whose statistics are governed by that of an Ornstein-Uhlenbeck process. The two parameters of the process, namely the coherence rate κ and the coupling strength σ can be derived from T_2, T_2^*:

$$\sigma = \frac{\sqrt{2}}{2T_2^*} \tag{2.36}$$

$$\kappa = \frac{6(T_2^*)^2}{T_2^3} \tag{2.37}$$

The detailed discussion of the random processes is done in section 1.5.

Measuring the nuclear transition frequencies RF1 and RF2

Instead of doing a Ramsey experiment, we can phase-shift the final $\pi/2$-RF pulse by π and extract from the resulting oscillation the radio transition frequencies $\omega_{\text{RF1}} = 2\pi \times (493.62 \pm 0.04)\,\text{kHz}$ and $\omega_{\text{RF2}} = 2\pi \times (2489.73 \pm 0.06)\,\text{kHz}$ [Gri+25]. These are directly related to the values of the coupling tensor through

$$A_{zz} = \frac{\omega_{\text{RF1}}^2 - \omega_{\text{RF2}}^2}{2\gamma_n B_z} \tag{2.38}$$

and

$$A_{zx} = \sqrt{4\omega_{\text{RF2}}^2 - (A_{zz} - 2\gamma_n B_z)^2}. \tag{2.39}$$

which makes it easier to extract the remaining free parameters γ_n and B.

ODMR-fits

A common technique for characterizing color center systems is to scan the system with a pulsed optically-detected magnetic resonance (pODMR). A good review on that is [Car09]. For each frequency step, the Germanium vacancy center is optically initialized, then a π-pulse is applied at the corresponding microwave frequency and the electron spin gets read out optically. This scheme is then repeated many times and the resulting florescence signal is plotted against the frequency signal. In Figure 2.2 (taken with description from supplementary material of [Gri+25]). We show how such an experimentally generated ODMR-sweep looks like and that we can reproduce the experimental data with high accuracy (with R^2 values ranging from 0.9328 to 0.9854) [Gri+25].

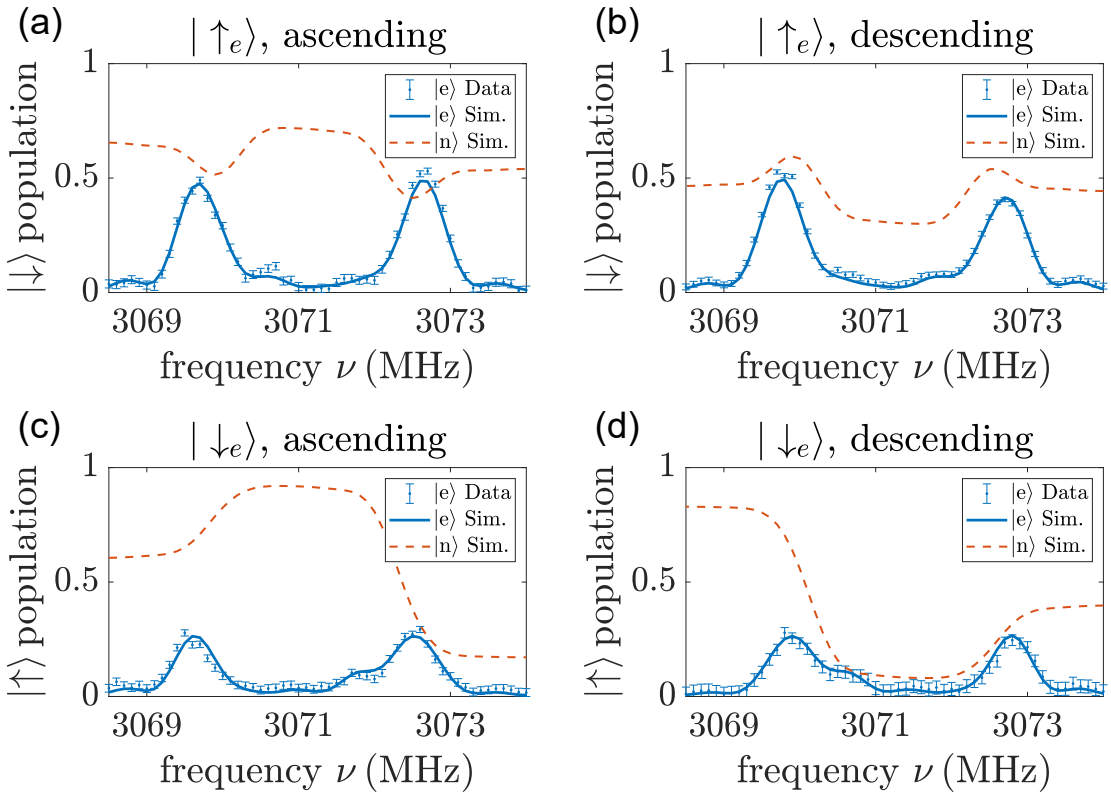

Figure 2.2.: R^2 of the model for different values of γ_e^{eff} and B_i. The images differ by their electron spin state of $|\uparrow_e\rangle$ for (a) ascending frequency sweep direction, (b) for descending frequency sweep direction and $|\downarrow_e\rangle$ for (c) ascending frequency sweep direction and (d) for descending frequency sweep direction. (e) Mean R^2 of the highest individually achieved R^2 of all four ODMR measurements for the respective γ_e^{eff}. The cross indicates the best mean R^2 value achieved in the simulation, which is slightly higher than the mean R^2 values in the sweep due to the finite sampling size of the sweep (adapted from [Gri+25], © American Physical Society.)

2.6. Narrowband pulses and gate synthesis

When we drive the system on resonance with one of the MW-transitions, we observe Rabi-oscillations. If there were no A_{zx}-coupling and no noise present in the system, the solution of the time dependent Schrödinger equation could be (after doing a RWA) solved analytically, and we would get for the time dependent populations (if we start in $\rho_I = 0.5\,|v_1\rangle\langle v_1| + 0.5\,|v_2\rangle\langle v_2|$)

$$c_1(t) = \mathrm{Tr}(\rho\,|v_1\rangle\langle v_1|) = \frac{1}{2}\cos^2\left(\frac{\Omega t}{2}\right) \tag{2.40}$$

$$c_2(t) = \mathrm{Tr}(\rho\,|v_2\rangle\langle v_2|) = \frac{\Omega'^2}{2\Omega^2}\cos^2\left(\frac{\Omega' t}{2}\right). \tag{2.41}$$

Here, Ω is the Rabi-frequency (drive strength), $\Omega' = \sqrt{\Omega^2 + \Delta^2}$ is the detuned Rabi-frequency and Δ is the frequency difference to the other transition frequency $\Delta = \omega_{00,10} - \omega_{01,11}$.
If we now want to do a π-pulse on one of the transitions and no rotation on the other transition we have to fulfil the following conditions:

$$\frac{\Omega t}{2} = \frac{\pi}{2} + k\pi \tag{2.42}$$

$$\frac{\Omega' t}{2} = l\pi. \tag{2.43}$$

This is the first time the case for $k = 0, l = 1$ leading to

$$\frac{\Omega}{\sqrt{\Omega^2 + \Delta^2}} = \frac{1}{2} \tag{2.44}$$

$$\Rightarrow \Omega = \pm\frac{\Delta}{\sqrt{3}} \tag{2.45}$$

meaning we can achieve a good inversion on the electron if we choose the Rabi-frequency as $\Omega = \frac{\Delta}{\sqrt{3}}$. In Figure 2.3 we show and discuss the simulations on how this can be used to implement a projective SWAP gate in the experimental setup.

2.7. Nuclear spin pumping

As we already saw in the pODMR plots, the polarization of the nuclear spin can be affected by applying a combination of pulses on the electron spin transitions and on the optical transitions. We can capitalize on this effect by searching for a sequence of optical and electron pulses which allow us to initialize the nuclear spin. The reason that this should be possible is that the strong hyperfine coupling (compared to the Larmor frequency), allows us to simultaneously alter the electron and the nuclear spin state, which is normally forbidden [Jef60]. In section 2.10 we show in more detail how this works. We start by initializing the nuclear spin state in $|\downarrow_e\rangle$. We

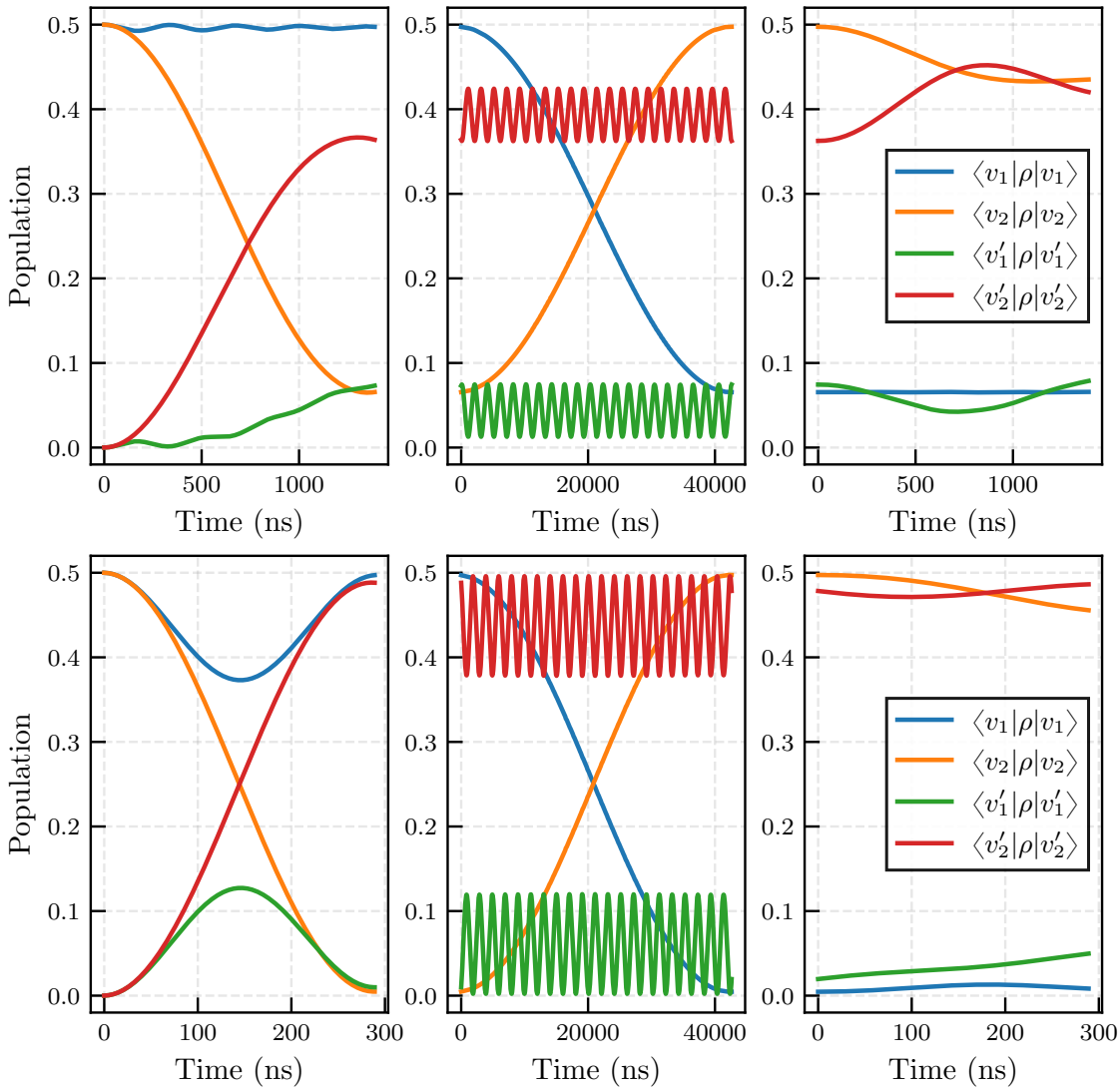

Figure 2.3.: Simulation of a projective SWAP gate realized by three consecutive projective CNOT gates. The electron is initially in $|\downarrow_e\rangle$ and the nuclear spin is in a completely mixed state. In the top row we show an implementation with a drive amplitude of $\Omega_e = 2\pi \times 0.360\,\mathrm{MHz}$, while the second row shows the time evolution with the constant but optimized drive amplitude $\Omega_e = \frac{\Delta}{\sqrt{3}} = 2\pi \times 1.722\,\mathrm{MHz}$. The simulated resulting polarization of the nuclear spin improves from 85.6 % for the top row to 94.2 %. The imperfections likely stem from a combination of A_{zx} and the dephasing present on the electron. In the experiment the bottom row strategy was implemented to initialize the nuclear spin.

then apply a π-pulse on the MW1 or MW2 transition and re-initialize the electron spin with a suited laser pulse and repeat this process N times. Afterward, one can look at another pODMR-measurement and observe only one peak, indicating the nuclear spin state is indeed initialized. However, since the pODMR itself changes the nuclear spin polarization, it is not easy to estimate a fidelity with it. Instead, in the experiment, the nuclear spin state was equally initialized with a projective SWAP operation (compare Figure 2.3) by applying a sequence of narrowband microwave and radio frequency pulses which lead to conditional flips on the electron and nuclear spin states. With this strategy an estimated fidelity of 95 % for $N = 15$ (+1 readout pulse) is achieved, while the simulation gives a similar polarization estimate of 94 % and estimates that a polarization of 98.7 % is achievable if $N = 50$ [Gri+25]. In Figure 2.4 the dynamics of the spin states during such a spin pumping scheme are shown and discussed.

2.8. Optimal Control for GeV-Center

We will use optimal control to optimize given experimental procedures by modifying the shape of the control pulses. After using the rotating wave approximation, the drive Hamiltonian on each of the electron transitions can be written as

$$H_d(t) = \frac{\Omega_e(t)}{2}[\cos\phi(t)X \otimes \mathbb{1} + \sin\phi(t)Y \otimes \mathbb{1}]. \tag{2.46}$$

We now implement the dCRAB algorithm (compare section 1.8) for the two accessible control fields $\Omega_e(t)$ and $\phi(t)$ to achieve different goals.

2.8.1. Optimizing MW-Pulse for polarizing the nuclear spin

The first goal we want to achieve with optimal control is to successfully polarize the nuclear spin. The nuclear spin eigenstate depends on the electron state, so we have to decide along which of the electron states we want to polarize. We decide for the quantization axis which aligns with the electron spin down $|\downarrow_e\rangle$ and we can now define a figure of merit as

$$\text{FoM} = 1 - \langle v_2|\,\rho\,|v_2\rangle - \langle v_2'|\,\rho\,|v_2'\rangle \tag{2.47}$$

where v_2 is the eigenvector of the Hamiltonian corresponding to $|\downarrow_e\uparrow_n\rangle$ and $v_2' = (X \otimes \mathbb{1})v_2$, which points for the nuclear subspace in the same direction as the eigenvectors in the $|\downarrow_e\rangle$-subspace but has a flipped electron spin state. For the optimization we search in the Fourier basis of functions, set the number of superiterations to $N_{\text{super}} = 10$ and evaluate the function up to $n_{\text{eval}} = 1000$ times per superiteration and repeat this process for different pulse durations. The results are discussed in Figure 2.5. The simulations suggest that we can indeed initialize the nuclear spin with a high average polarization of 99.9 %. Furthermore, this approach has in contrast to nuclear spin pumping (section 2.7) the advantage that we do not need to repetitively reinitialize the electron, which allows not only for more precise but also faster operation.

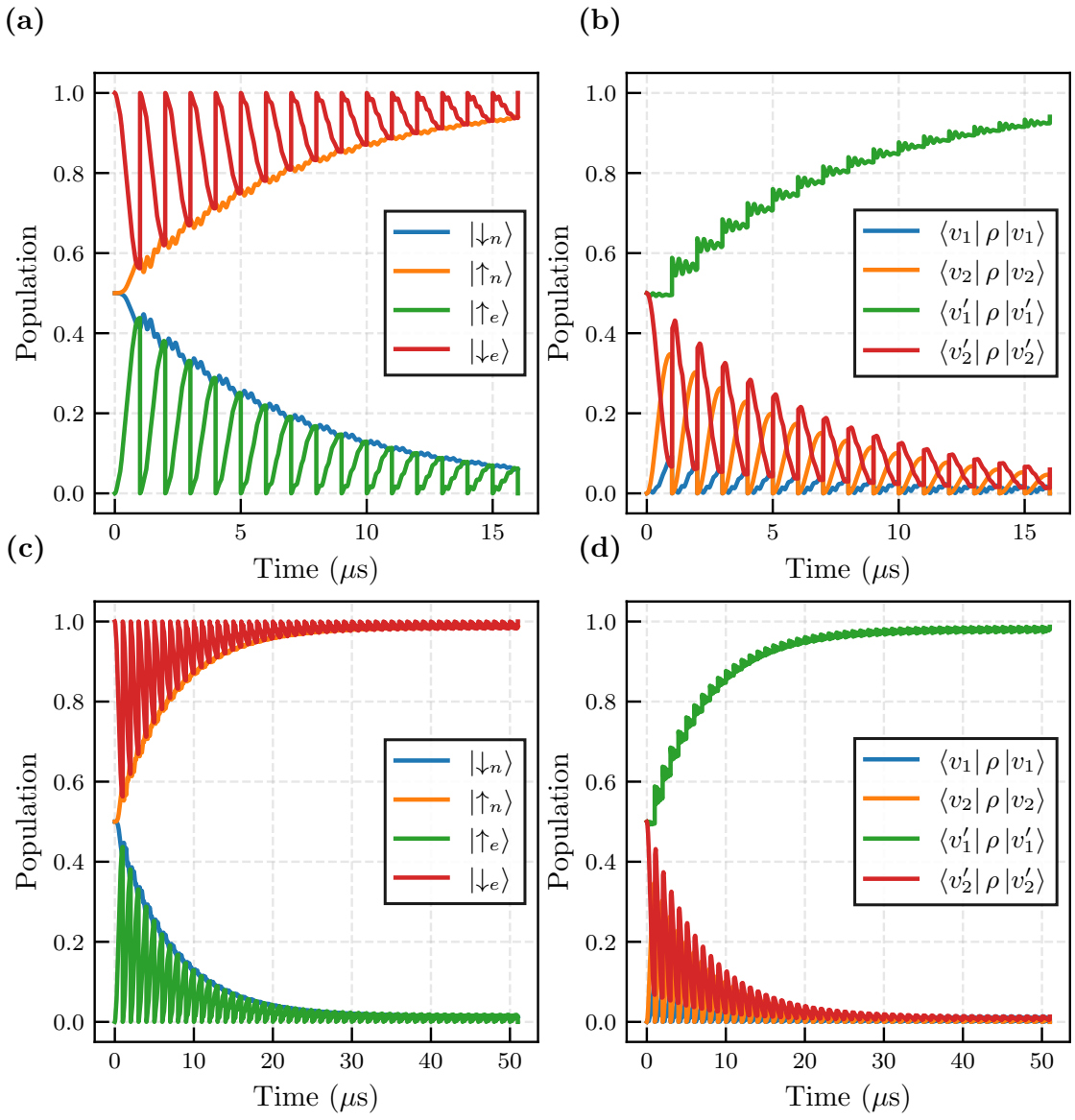

Figure 2.4.: Simulated nuclear spin pumping scheme with electron resets. (a) and (c) show the dynamics of the system if we trace out the other spin for $N_{(a),(b)} = 15{+}1$ and $N_{(c),(d)} = 50{+}1$ while in (b) and (d) the dynamics in the eigenbasis within the $|\downarrow_e\rangle$ sub-manifold, with v_i denoting the eigenvectors and v_i' their electron flipped counterpart (adapted from [Gri+25], © American Physical Society.)

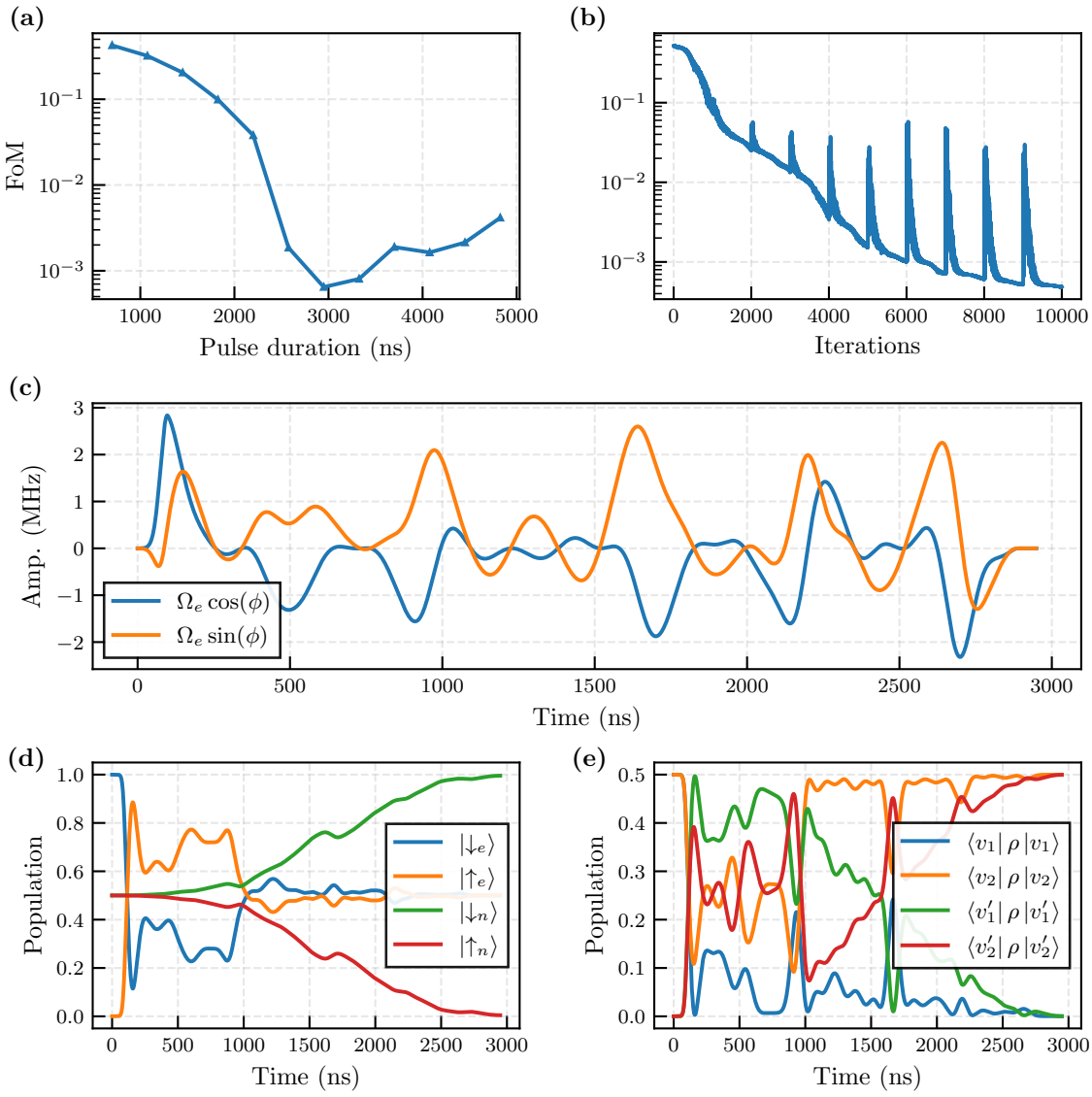

Figure 2.5.: Optimization of the nuclear spin state polarization with a single optimized MW pulse. (a) Resulting polarization infidelity of the nuclear for different pulse durations, where each point was optimized separately (averaged over 5000 OU noise realizations). (b) Optimization progress for a fixed pulse duration (Optimization is done for 100 fixed OU noise realizations). (c) Resulting driving pulse shapes for one optimized duration. (d)-(e) Time evolution (d) while tracing out the other spin, (e) populations along the nuclear quantization axis defined by $|\downarrow_e\rangle$ during the application of an optimized pulse. (b) - (e) relate to the pulse with the minimal FoM which occurred at a duration of 2950 ns (adapted from [Gri+25], © American Physical Society).

2.8.2. Optimal Control for phase-accurate CNOT gates

We already saw in section 2.6 that the projective CNOT gates work well if we choose the drive amplitude accordingly. Here, we want to see if we can even do phase-accurate operations on the qubits. The controlled NOT operation acts only on the second qubit if the first qubit is in the $|1\rangle$-state. In the computational basis its unitary takes the form,

$$\mathrm{C}_n\mathrm{NOT}_e = \begin{pmatrix} 1 & 0 & 0 & 0 \\ 0 & 0 & 0 & 1 \\ 0 & 0 & 1 & 0 \\ 0 & 1 & 0 & 0 \end{pmatrix}. \tag{2.48}$$

This is the first time we care about relative phases. Therefore, it is important to specify in which rotating frame the gates are realized. Since we want to ideally implement multiple gates, they should all refer to the same frame of reference. We choose the frame such that it rotates with the mean of the two microwave transitions $\omega_f = \omega_e = (\mathrm{MW1} + \mathrm{MW2})/2$. We use the Frobenius measure to define the figure of merit in this case as

$$\mathrm{FoM} = \frac{1}{N}\sum_{k=1}^{N}\left[1 - \frac{1}{16}\left|\mathrm{Tr}\left\{U_k^\dagger(T)\mathrm{C}_n\mathrm{NOT}_e\right\}\right|^2\right], \tag{2.49}$$

where U_k is the unitary resulting from a single noise trajectory. In Figure 2.6 we discuss the result of the pulse optimizations. The inversion on the nuclear spin however has the more familiar matrix representation

$$\mathrm{C}_e\mathrm{NOT}_n = \begin{pmatrix} 1 & 0 & 0 & 0 \\ 0 & 1 & 0 & 0 \\ 0 & 0 & 0 & 1 \\ 0 & 0 & 1 & 0 \end{pmatrix}. \tag{2.50}$$

The corresponding results are discussed in Figure 2.7. We note that by using the internal strong A_{zx} coupling we can use the MW drive to control the nuclear spin, allowing both for faster and more accurate manipulation as it is possible with the traditional narrowband RF control.

2.8.3. Optimal Control for phase-accurate SWAP gate

Another important operation in quantum communication is the SWAP gate which allows swapping states between different qubits, i.e.

$$\mathrm{SWAP}\,|\phi_1\rangle \otimes |\phi_2\rangle = |\phi_2\rangle \otimes |\phi_1\rangle\,. \tag{2.51}$$

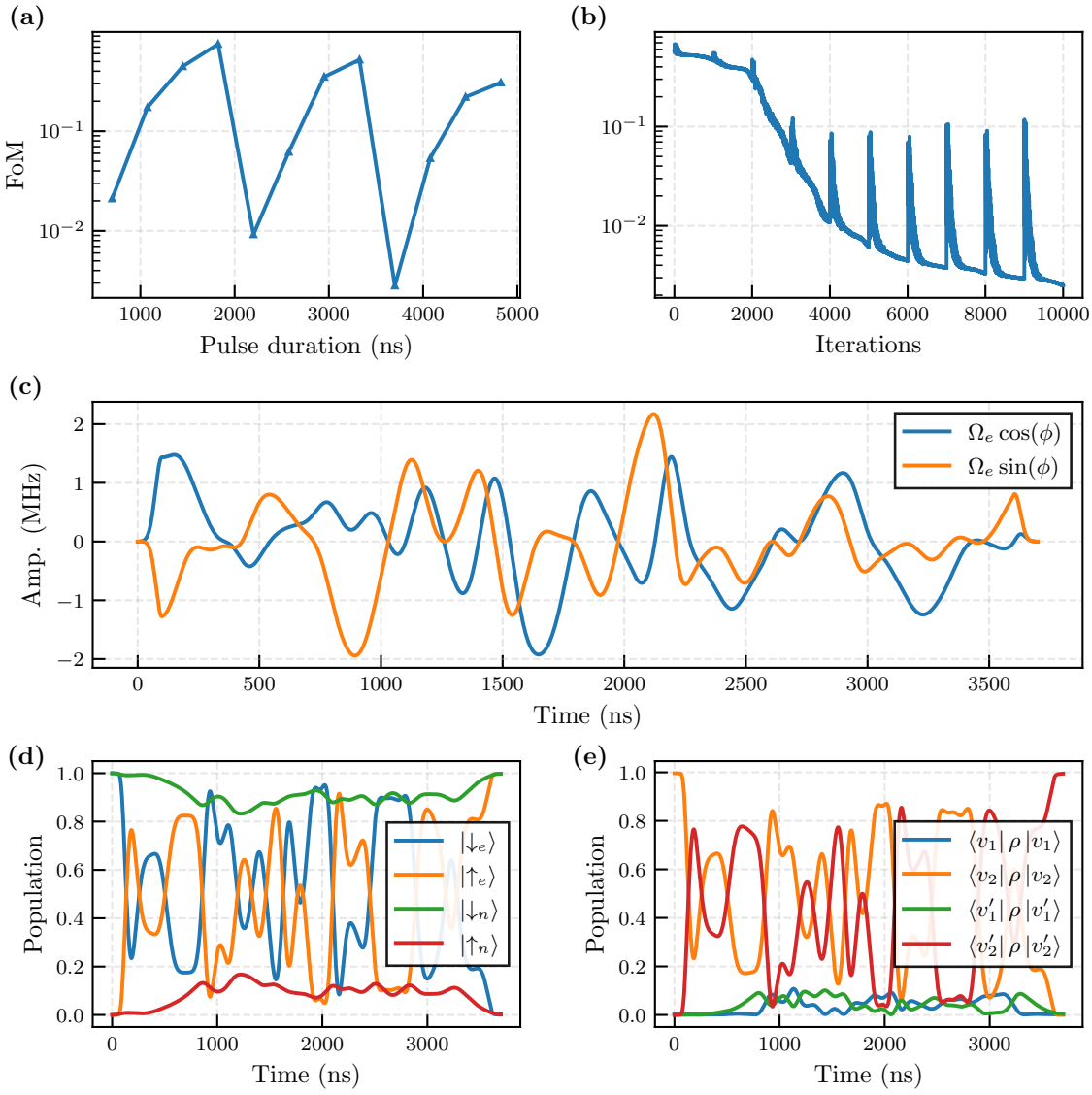

Figure 2.6.: Optimization process for the C_nNOT_e gate (a) shows the reached figure of merit for different gate durations, the best reached fidelity is $F = 99.7\,\%$ at a gate duration of $3.7\,\mu s$, (b) is the progress of one optimization, (c) shows the resulting pulse, (d) the populations tracing out the other spin and (e) the populations in the eigenbasis of the electron.

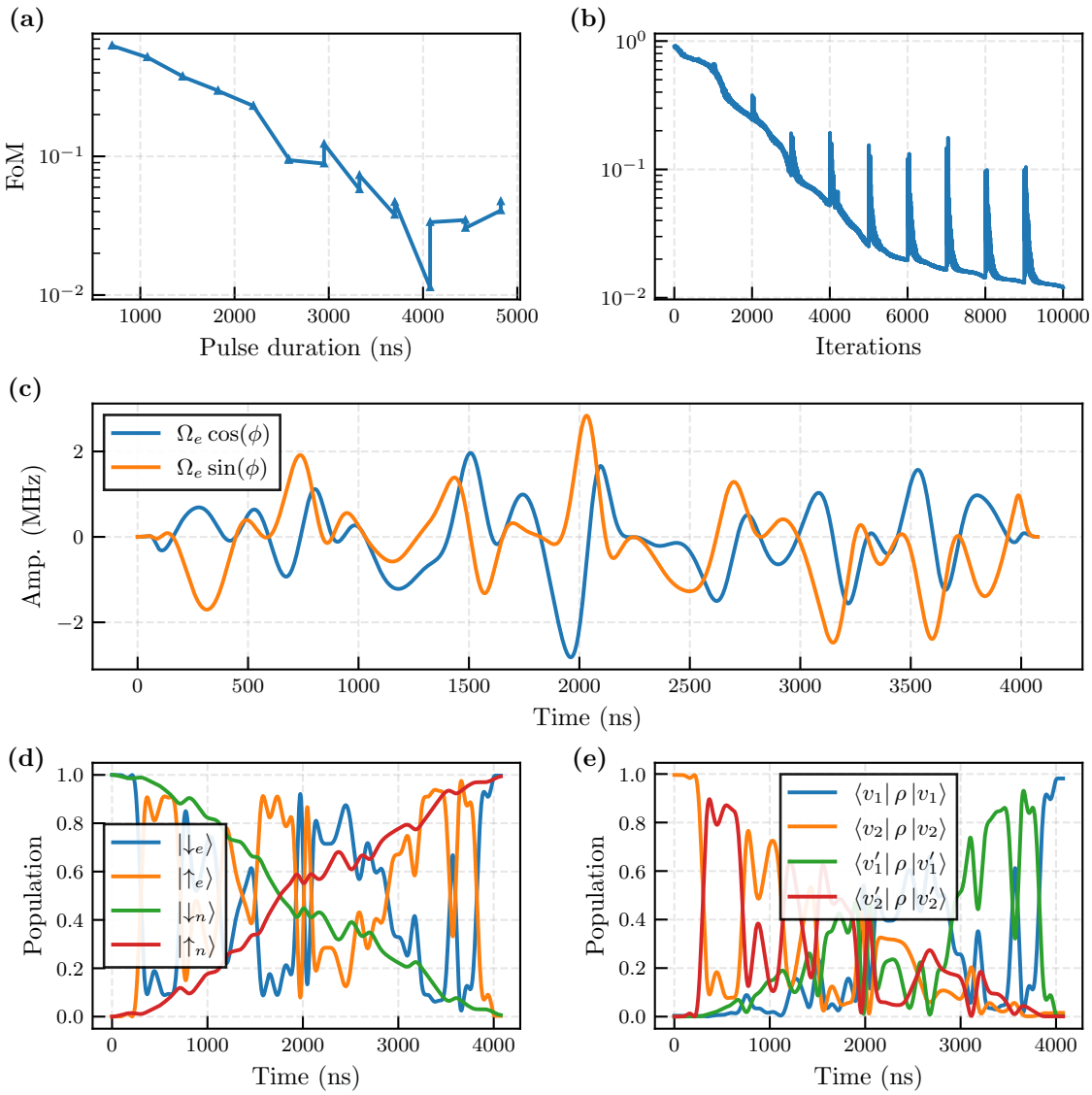

Figure 2.7.: Optimization process of a C_eNOT_n gate (a) shows the reached figure of merit for different gate durations, the best reached fidelity was $F = 98.82\,\%$ at a gate duration of $4.075\,\mu s$ (b) is the progress of the optimization for the best reached infidelity, (c) shows the resulting pulse, (d) the populations tracing out the other spin and (e) the populations in the eigenbasis of the electron.

This is especially useful for moving quantum information into a subspace where they are not as strongly affected by the environment, e.g. from the electron to the nuclear spin. The previously optimized CNOT gates allow us to implement a SWAP operation by using three of them in a series. Building a swap gate this way would result in a fidelity of $F_{\mathrm{SWAP},1} \approx F(\mathrm{C_eNOT_n})F(\mathrm{C_nNOT_e})F(\mathrm{C_eNOT_n}) \approx 97.3\,\%$ with a duration of $T_{\mathrm{SWAP},1} \approx 11.775\,\mu\mathrm{s}$ or $F_{\mathrm{SWAP},2} \approx F(\mathrm{C_nNOT_e})F(\mathrm{C_eNOT_n})F(\mathrm{C_nNOT_e}) \approx 98.2\,\%$ with a duration of $T_{\mathrm{SWAP},2} \approx 11.475\,\mu\mathrm{s}$ (result is obtainend by mutliplying the respective fidelities). However, if specifically this gate is required in a greater circuit, we might also implement a version by optimizing it directly. We again use the Frobenius measure to define the figure of merit in this case as,

$$\mathrm{FoM} = \frac{1}{N}\sum_{k=1}^{N}\left[1 - \frac{1}{16}\left|\mathrm{Tr}\{U_k^\dagger(T)V\}\right|^2\right] \tag{2.52}$$

where $V = \mathrm{SWAP}$ and U_k is the unitary resulting from a single noise trajectory. In Figure 2.8 we discuss the process of pulse optimization for the coherent SWAP gate. While the fidelities are slightly worse we can implement the gate much faster. Later optimizations (compare chapter 3) showed that there was still room for improvement, by allowing for more oscillations in the regarded intervall, increasing the function evaluations per superiteration and increasing the number of optimized parameters.

2.8.4. Robust Optimal Control

The optimized gates here are already robust against dephasing noise. However, since in a real experiment we have to deal also with other uncertainties in the system's parameters, we try to incorporate these as well. We estimate uncertainties Δ_j in the four Hamiltonian parameters $\omega_d, B, A_{zx}, A_{zn}$ (the value for γ_n is well known in the literature and γ_e is strictly known if B is certain, so both do not influence the fidelities too much). With that we can define the robust FoM as

$$\mathrm{FoM} = 1 - \frac{1}{M}\sum_{j\in\{\pm\}^4}\frac{1}{N}\sum_{k=1}^{N}\left[\frac{1}{16}\left|\mathrm{Tr}\{U_{k,j}^\dagger(T)V\}\right|^2\right] \tag{2.53}$$

where $U_{k,j}$ is the resulting unitary assuming for each Hamiltonian parameter $P = P_0 \pm \Delta_j$, the number of noise realizations was reduced to $N = 8$ because the machine used has $16 \times 8 = 128$ cores such that the figure of merit can be evaluated in parallel. In Figure 2.9, we compare the performance of a pulse optimized with the normal FoM and the robust FoM. We notice that including uncertainties into the optimization process is a good idea when precise control can be applied.

2.9. Decoupling gates for Germanium Vacancy centers

For the following section, we ignore for a moment the influence of the dephasing and look at the basic math describing our system. First, we demonstrate how dynamical

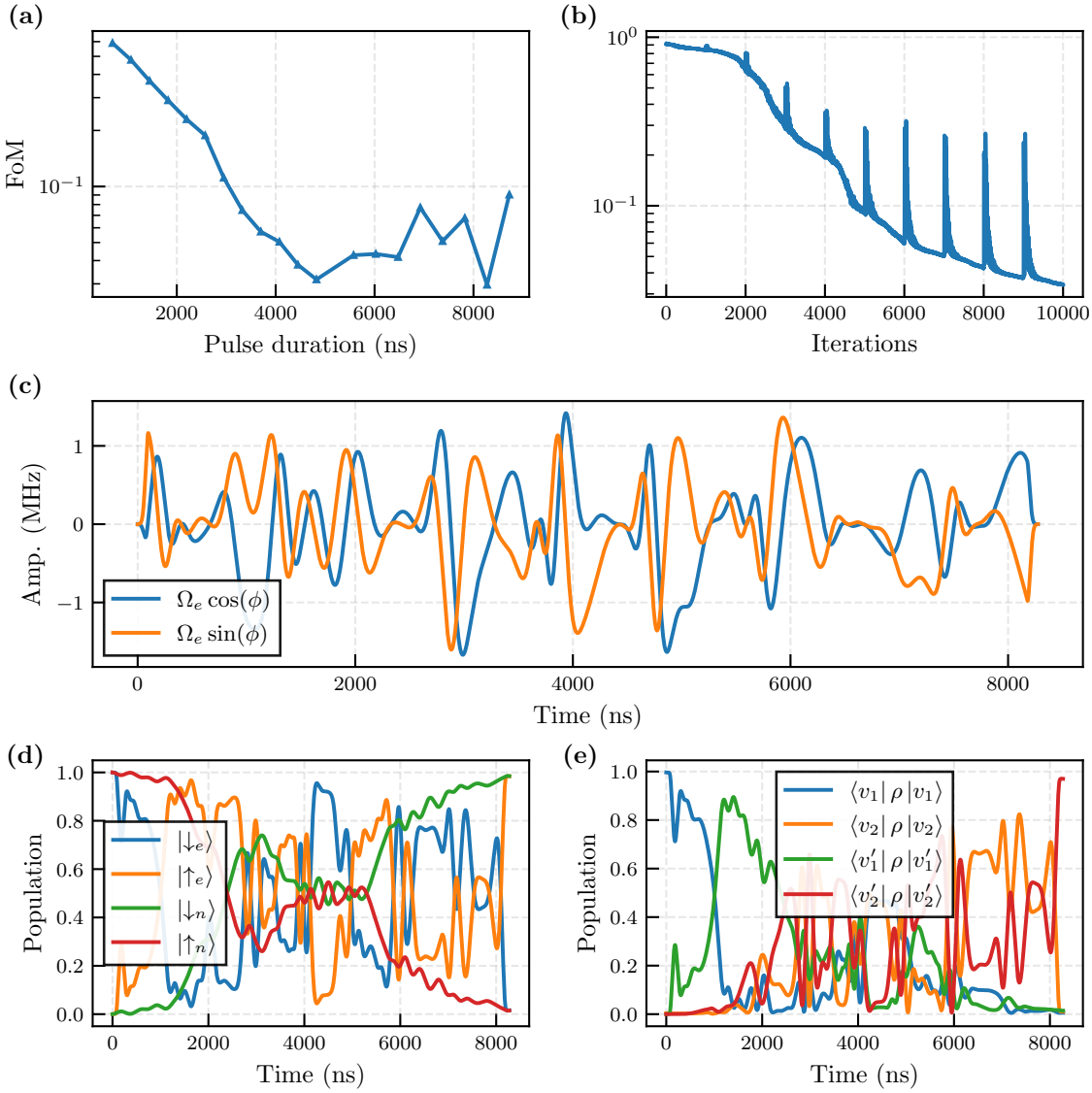

Figure 2.8.: Optimization process of a SWAP gate (a) shows the reached figure of merit for different gate durations, the best reached fidelity was $F = 97.0\,\%$ at a gate duration of $8.275\,\mu s$ but there is also a much faster and only slightly worse implementation available with a fidelity of $F = 96.5\,\%$ at a gate duration of $4.825\,\mu s$ (b) is the progress of the optimization for the best reached infidelity, (c) shows the resulting pulse, (d) the populations tracing out the other spin and (e) the populations in the eigenbasis of the electron.

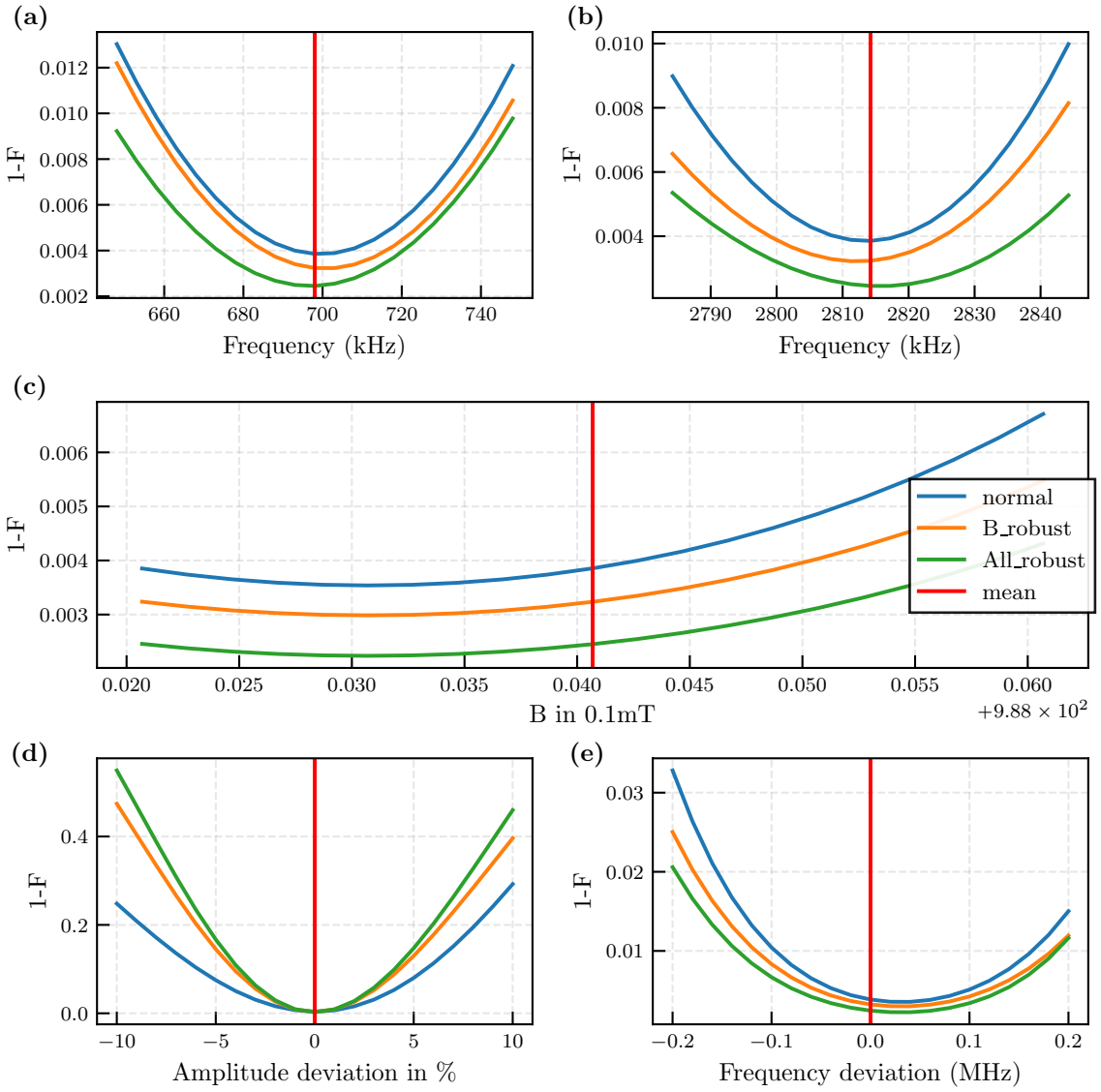

Figure 2.9.: Robustness check of a SWAP gate which was optimized with different figures of merit. We compare three different optimization processes The green lines represent the result were the FoM included an average over the most relevant parameters of the experiment, the orange line included an average over the magnetic field fluctuations and the blue one did only acknowledge the presence of dephasing noise. a) Shows the robustness against the A_{zx} deviations, (b) against A_{zz} deviations, (c) against magnetic field (d) against the amplitude error of the drive and (e) against the frequency deviation of the drive. We observe that it is in general a good idea to include robust figures of measure, the only case where it underperforms the normal figure of merit is regarding the drive amplitude, since it seems to rely on precise execution of the found pulse.

decoupling can be used to implement a ZX gate. This was already done for other spin quatum systems [Bar+25; CWP17]. We transform into the interaction frame in which the Hamiltonian takes the form

$$\begin{aligned}\tilde{H}(t) &= \mathrm{e}^{\mathrm{i}\omega_I t I_z} H \mathrm{e}^{-\mathrm{i}\omega_I t I_z} - \omega_I I_z \\ &= A_{zz} S_z I_z + A_{zx}(\cos(\omega_I t) S_z I_x - \sin(\omega_I t) S_z I_y).\end{aligned} \tag{2.54}$$

We see that the hyperfine interaction terms oscillate with the nuclear Larmor frequency. This suggests that properly timed control pulses can selectively average into an effective ZX coupling [MG58]. However, if we do not apply control fields, the oscillating terms will average out over a full period and therefore implement an effective ZZ gate. The conditions for implementing such a ZZ/2 gate are

$$\omega_I = 2A_{zz}, T = \frac{\pi}{A_{zz}}. \tag{2.55}$$

The new part here is that we allow the magnetic field to be tuned and thus enabling the first condition, this unfortunately only works for one nuclear spin. To get a method for implementing the interacting gate we can use average Hamiltonian theory [HW68], the Hamiltonian over a pulse interval $\delta_j \le t \le \delta_{j+1}$ is

$$\begin{aligned}H_{\mathrm{avg}}(\delta_{j+1}, \delta_j) &= \frac{1}{\delta_{k+1} - \delta_k} \int_{\delta_k}^{\delta_{k+1}} H(t)\mathrm{d}t \\ &= A_{zz} S_z I_z + \frac{A_{zx} S_z}{\omega_t(\delta_{j+1} - \delta_j)} \\ &\quad [\cos(\omega_I \delta_{j+1}) - \cos(\omega_I \delta_j) I_x \\ &\quad + \sin(\omega_I \delta_{j+1}) - \sin(\omega_I \delta_j) I_y].\end{aligned} \tag{2.56}$$

Our target is to generate the gate

$$\mathrm{ZX}/2 = \mathrm{e}^{\mathrm{i}\frac{\pi}{4}\sigma_z \otimes \sigma_x} = \mathrm{e}^{\mathrm{i}\pi S_z I_x}, \tag{2.57}$$

which is achieved by a n-pulse Carr–Purcell–Meiboom–Gill (CPMG) sequence with pulse locations $\delta_j = T\frac{j-1/2}{n}$, $\delta_0 = 0$, and $\delta_{n+1} = T$. In this case, the toggling-frame Hamiltonians add up to

$$\int_0^T H(t)\mathrm{d}t \approx \sum_{j=0}^{n} (-1)^j H_{\mathrm{avg}}(\delta_j, \delta_{j+1}). \tag{2.58}$$

If the magnetic field and therefore the Lamor frequency are tuned such that $\frac{T\omega_I}{n} \stackrel{!}{=} \pi$ and the number of pulses n is even, this expression simplifies to

$$\int_0^T H(t)\, dt \;\approx\; \frac{2}{\pi} A_{zx} T S_z I_x \;\stackrel{!}{=}\; \pi S_z I_x. \tag{2.59}$$

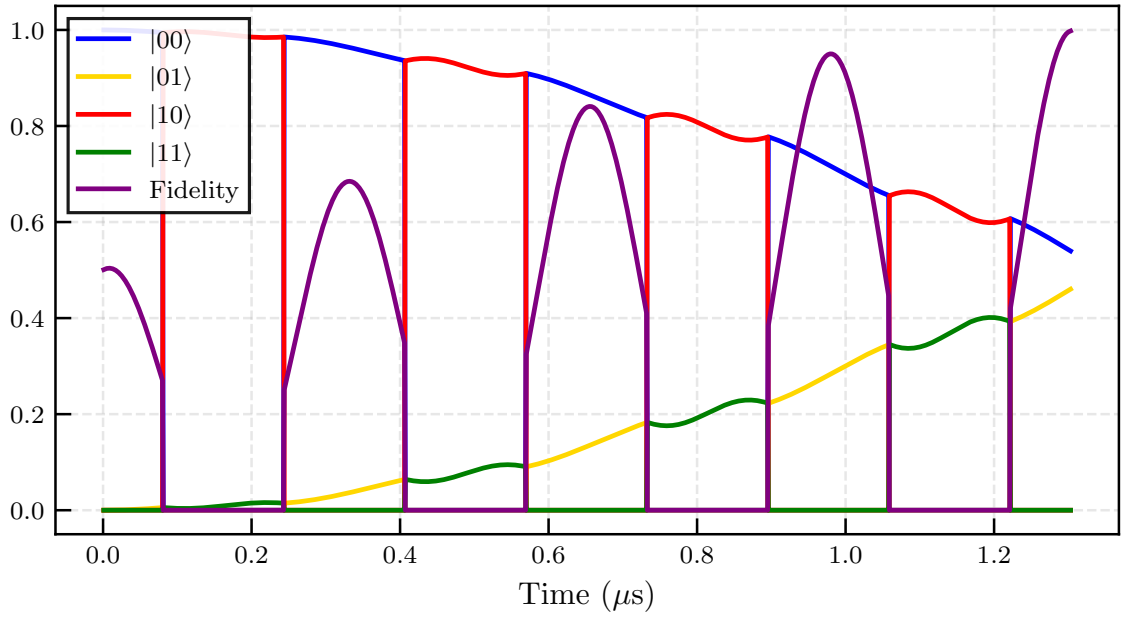

Figure 2.10.: Population dynamics during a dynamical decoupling gate implemented with $n = 8$ instantaneous π-pulses. The gate realizes the entangling ZX/2 operation. The purple line shows the unitary fidelity, which reaches $\mathcal{F} = 99.87\%$ for only eight pulses, and can be systematically improved by increasing n.

Thus, the required Larmor frequency and gate duration have to be chosen as

$$\omega_I = \frac{2nA_{zx}}{\pi}, \qquad T = \frac{\pi^2}{2A_{zx}}, \tag{2.60}$$

showing that the achievable gate speed is in this case limited by the transverse coupling A_{zx}. In practice, however, the usefulness of this approach is restricted by experimental limitations: high-fidelity DD gates require rapid and precise π-pulses on the electron spin, which are challenging to realize with available microwave control in strongly coupled systems [Gri+25; Res+25; Klo+22]. As a result, while conceptually appealing and useful for weakly coupled systems (there the dynamics are much slower and thus the MW-π pulses are fast enough) DD-based entangling gates are unlikely to be the most practical route for strongly coupled group IV systems.

2.10. Double-Quantum-Transition (YY) Gate

Now, we want to focus on the Double-Quantum-Transition (DQT) mechanism, which couples electron–nuclear spin states through simultaneous spin flips, mediated by the transverse hyperfine term A_{zx}. We care because they enable direct, noise-robust and spectrally selective control of two-spin-flip dynamics providing access to entangling

operations and give deeper inside in the fundamental limitations regarding gate speed. We will now show how the interaction is providing a resource for entangling gates. The static Hamiltonian in the electron frame reads

$$H_{\text{static}} = -\omega_I I_z + A_{zz} S_z I_z + A_{zx} S_z I_x \tag{2.61}$$

$$= \begin{pmatrix} a & b & 0 & 0 \\ b & -a & 0 & 0 \\ 0 & 0 & c & -b \\ 0 & 0 & -b & -c \end{pmatrix} \tag{2.62}$$

with

$$a = \frac{1}{4}(A_{zz} - 2\omega_I), \quad b = \frac{1}{4}A_{zx}, \quad c = -\frac{1}{4}(A_{zz} + 2\omega_I). \tag{2.63}$$

This form is block-diagonal, reflecting the fact that the nuclear spin Hamiltonian depends on the electron spin state.
For the electron $|\uparrow_e\rangle$ subspace, the eigenenergies are

$$E^{\pm}_{\uparrow_e} = \pm\sqrt{a^2 + b^2}, \tag{2.64}$$

with eigenvectors

$$v^{(+)}_{\uparrow_e} = \begin{pmatrix} \cos(\Theta_{\uparrow_e}/2) \\ \sin(\Theta_{\uparrow_e}/2) \end{pmatrix}, \quad v^{(-)}_{\uparrow_e} = \begin{pmatrix} \sin(\Theta_{\uparrow_e}/2) \\ -\cos(\Theta_{\uparrow_e}/2) \end{pmatrix}, \tag{2.65}$$

where $\tan(\Theta_{\uparrow_e}/2) = \frac{E^{+}_{\uparrow_e} - a}{b}$.
For the $|\downarrow_e\rangle$ subspace, we obtain

$$E^{\pm}_{\downarrow_e} = \pm\sqrt{c^2 + b^2}, \tag{2.66}$$

with corresponding eigenvectors

$$v^{(+)}_{\downarrow_e} = \begin{pmatrix} \cos(\Theta_{\downarrow_e}/2) \\ \sin(\Theta_{\downarrow_e}/2) \end{pmatrix} \text{and} \quad v^{(-)}_{\downarrow_e} = \begin{pmatrix} \sin(\Theta_{\downarrow_e}/2) \\ -\cos(\Theta_{\downarrow_e}/2) \end{pmatrix} \tag{2.67}$$

and $\tan(\Theta_{\downarrow_e}/2) = (c - E^{+}_{\downarrow_e})/b$. Thus, in the joint eigenbasis of the nuclear-spin Hamiltonian, the diagonalized static Hamiltonian reads

$$\tilde{H} = V^{\dagger} H V = \text{diag}(E^{+}_{\uparrow_e}, E^{-}_{\uparrow_e}, E^{+}_{\downarrow_e}, E^{-}_{\downarrow_e}) \tag{2.68}$$

where V is the matrix diagonalizing H in the shown way. Thus, the S_x-control is in this basis given as

$$V^{\dagger} \Omega S_x V = \Omega[\cos(\vartheta/2) S_x - 2\sin(\vartheta/2) S_y I_y], \tag{2.69}$$

meaning dependent on the drive we are not only driving the normal S_x part but also introduce, depending on ϑ, entangling operations. This is remarkable because driving double-quantum transitions is otherwise forbidden in the absence of A_{zx} [Gri+25; Pat+24]. For large nuclear Larmor frequencies ω_I, the effective Rabi frequency of the DQT channel is approximately

$$\Omega_{\mathrm{DQT}} \approx \frac{A_{zx}}{\omega_I}\Omega, \tag{2.70}$$

driving $\Omega_{\mathrm{DQT}} S_y I_y$, where the sign of Ω is chosen accordingly. If $|\Omega_{\mathrm{DQT}}|$ is small enough such that we can drive DQT selectively and not also the single quantum transition S_x, we can implement the corresponding two-qubit entangling gate

$$U = \exp\left(\mathrm{i}\tfrac{\pi}{4}\,\sigma_y \otimes \sigma_y\right) \tag{2.71}$$

which thus can be implemented in a characteristic time

$$T_g \approx \frac{\pi}{|\Omega_{\mathrm{DQT}}|}. \tag{2.72}$$

A lower bound on the time required to implement the target operation is given by

$$T \geq \frac{\pi}{\sqrt{A_{zx}^2 + A_{zz}^2}} \approx 170\,\mathrm{ns}, \tag{2.73}$$

derived using results from [BJG23] and [IG25]. This bound assumes that simultaneous control over both the electron and nuclear spins allows the combined hyperfine interaction to be rotated to the YY direction, thereby achieving an efficient evolution. In our case, however, we restrict ourselves to limited power microwave control of the electron spin, as fast nuclear spin manipulation is experimentally unfeasible. For the investigated GeV center rectangular microwave pulses with $\Omega = 2\pi \times 11\,\mathrm{MHz}$ lead to gate durations of a few microseconds. This is below the coherence times reachable in the experimental setting and therefore testable. In Figure 2.11 this behavior is shown. The fidelity of a DQT gate increases with increasing nuclear Larmor frequency, consistent with the scaling expected by Equation (2.70) and Equation (2.72). The corresponding dynamics for a Larmor frequency of $\omega_I = 10\,\mathrm{MHz}$ and a gate duration of $T = 1.9\,\mu\mathrm{s}$ is displayed in Figure 2.12. The figure shows coherent oscillations between $|\uparrow_e\uparrow_n\rangle$ and $|\downarrow_e\downarrow\rangle_n$ which are driven by the DQT. We see fast oscillations in both the populations and in the Fidelity, likely stemming from the Larmor frequency, and a slower modulation with a frequency of approximately 1 MHz. Furthermore, we also did an optimization of the DQT YY-gate. First, we modulated the envelope of the applied pulses by a Gaussian raise time of 100 ns to ensure that the pulse starts and ends at zero amplitude, second, we limited both Ω and ω_I to 15 MHz, and pre-optimized these two values for a flat-top pulse. Afterward, we optimized this initial guess envelope with dCRAB, for reaching better fidelities. The Larmor frequency ω_I was also included in the optimization process, since it is important to time the respective peak of the fidelity. The results are depicted in Figure 2.13. We see that we can significantly improve the reached fidelity to $F = 99.85\%$, while at the same time gaining insight in what is limiting the speed in which we can implement the gate. This is what we will investigate in more detail in the next section.

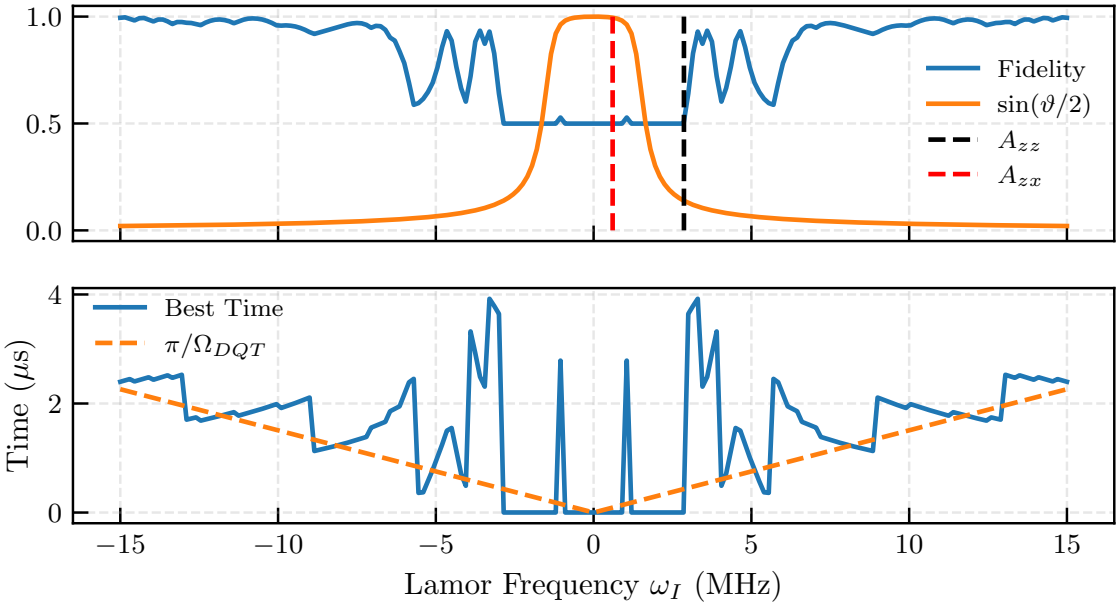

Figure 2.11.: Shown is the performance of the double-quantum transition (DQT) gate as a function of the nuclear Larmor frequency ω_I. In the top panel, the maximum gate fidelity reached with rectangular microwave pulses with a Rabi frequency of $\Omega = 2\pi \times 11\,\mathrm{MHz}$ is shown. Thereby, the gate duration is varied between 0 and 4 µs. In the bottom panel, the corresponding gate times at which the highest fidelity was achieved is shown. The dashed orange line represents the characteristic time from Equation (2.72) showing good agreement with the observed scaling.

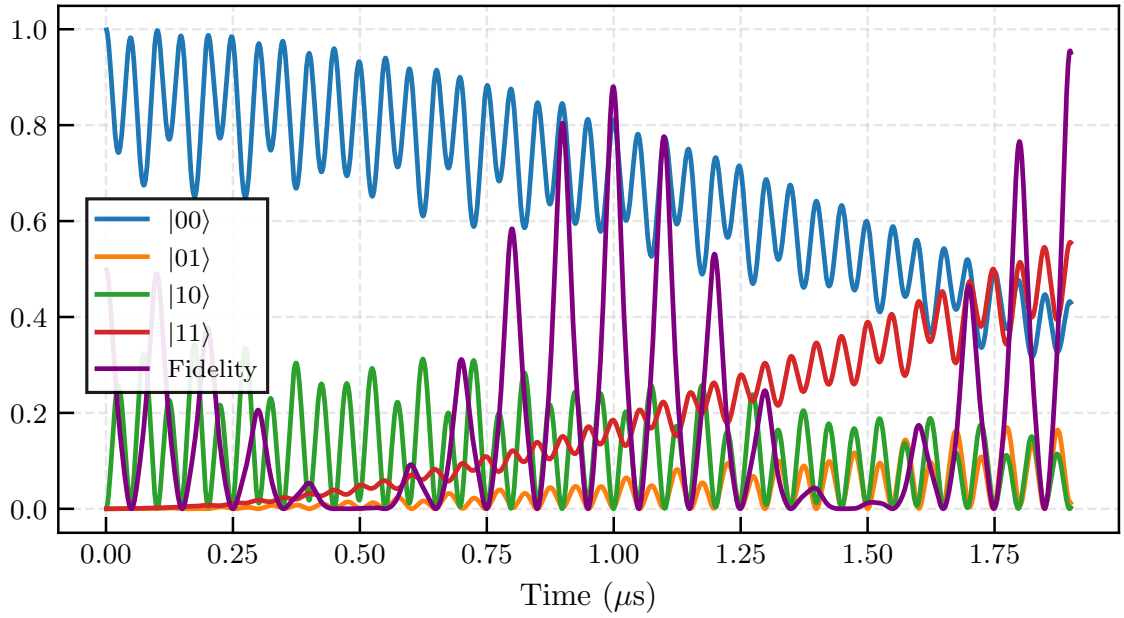

Figure 2.12.: Time evolution of a two-qubit system under DQT driving, shown in the rotating frame of the electron spin after applying the RWA. The control field is of the form $\Omega(t) = \Omega_0 \cos(\omega_I t)\cos(\omega_e t)$, leading to coherent population oscillations between $|\uparrow_e\uparrow_n\rangle$ and $|\downarrow_e\downarrow_n\rangle$ mediated by the A_{zx} coupling.

2.11. Speed-Limits

Finding the limitations in operating quantum systems has been and still is an interesting field of research, since it covers the fundamental rules of how our universe works, a good overview over the topic is given in [DC17], where quatum speed-limits and relativistic information flow touch. Coming back to our system if we assume that arbitrary strong drive fields are available, we can discuss how the interaction strength still limits the time we need to implement a desired non-local operation. A speed limit for an arbitrary state-transfer with constant Hamiltonian is given by a result from Giovannetti, Lloyd, and Maccone [GLM03a; GLM03b; GLM04]

$$\tau_{\mathrm{QSL}} = \max\left(\frac{\Theta(\rho_0,\rho_\tau)}{\Delta H}, \frac{2}{\pi\langle H\rangle}\Theta^2(\rho_0,\rho_\tau)\right). \tag{2.74}$$

Here, Θ is the Bures angle [Kak48; Bur69].

$$\Theta(\rho_0,\rho_\tau) = \arccos\left(\sqrt{F(\rho_0,\rho_\tau)}\right) \tag{2.75}$$

$$\overset{\text{pure states}}{=} \arccos\left(|\langle\psi_0|\psi_\tau\rangle|\right) \tag{2.76}$$

and ΔH is the variance of the Hamilton operator, and $\langle H\rangle$ is its expectation value. Under the assumption of infinitely fast single qubit operations we can implement the

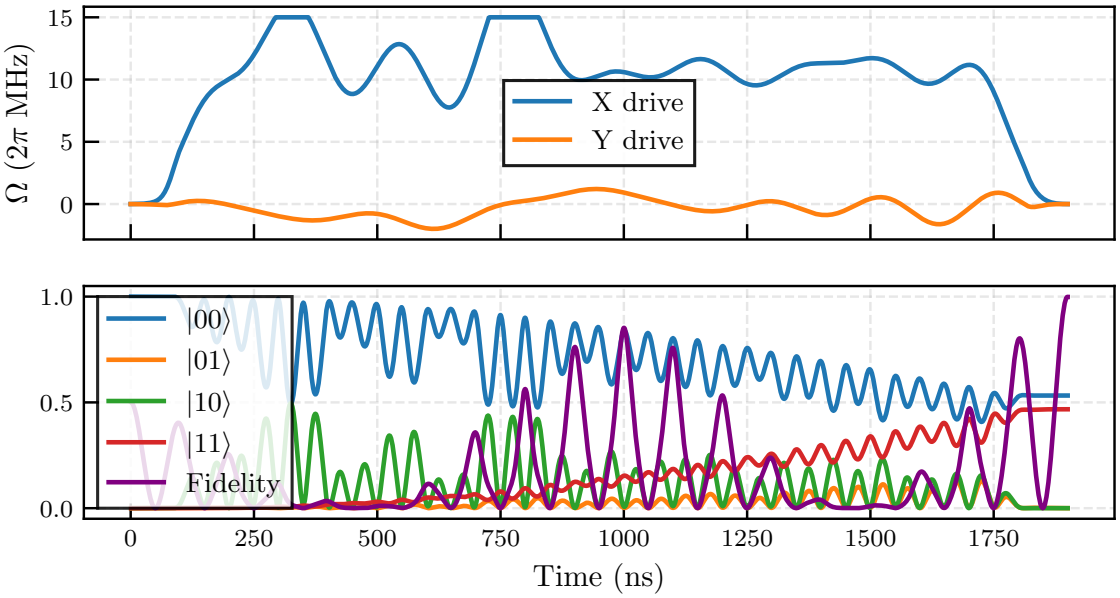

Figure 2.13.: Optimization of a YY/2 gate with the optimal control method. The top plot shows the resulting optimal control pulses which were bandwidth limited to $\Omega_{\max} = 15\,\mathrm{MHz}$, the start was a DQT gate with smooth envelope and a pure X-drive. The lower plot shows the population of the two-qubit system, as well as the fidelity during the pulse. It peaks at 99.85% at the end of the evolution.

CNOT, iSWAP and SWAP operations in:

$$\tau^{\mathrm{CNOT}} = \frac{\pi}{\sqrt{A_{zx}^2 + A_{zz}^2}} \tag{2.77}$$

$$\tau^{\mathrm{iSWAP}} = 2\frac{\pi}{\sqrt{A_{zx}^2 + A_{zz}^2}} \tag{2.78}$$

$$\tau^{\mathrm{SWAP}} = 3\frac{\pi}{\sqrt{A_{zx}^2 + A_{zz}^2}} \tag{2.79}$$

we note that for iSWAP this is the speed limit calculated in [BJG23]. We can visualize this behavior by looking at the dynamics modulo single qubit rotations, i.e. in the Weyl representation introduced in section 1.7. Therefore, we take the undriven Hamiltonian and calculate the resulting unitary evolution $U(t)$. For each unitary we then calculate the Weyl coordinates via the algorithm introduced in section 1.7. We notice that the result is a sawtooth like oscillation in c_1, where its value is building up till a CNOT equivalent gate is reached and afterward drops again with the same speed. At the first peak, the resulting native unitary is very close to a controlled, phase shifted Z gate (CiZ). If we now want to implement another gate in the Weyl chamber we have to apply corresponding local-rotations such that after reaching the peak, c_2 can be increased. If we wait till $c_2 \approx c_1 \approx \pi/2$ we have implemented a iSWAP equivalent, now we again have to perform single qubit rotations, to move the entangling power of the interaction to the third Weyl coordinate c_3. After again waiting for a time τ^{CNOT} we have implemented a SWAP equivalent. This can be accomplished by implementing three CNOTs with single-qubit rotations

$$\mathrm{SWAP} = \mathrm{C}_e\mathrm{NOT}_n\mathrm{C}_n\mathrm{NOT}_e\mathrm{C}_e\mathrm{NOT}_n, \tag{2.80}$$

where

$$\mathrm{C}_e\mathrm{NOT}_n = (S^\dagger \otimes H)(\mathrm{CiZ})(\mathbb{1} \otimes H) \tag{2.81}$$

$$\mathrm{C}_n\mathrm{NOT}_e = \left(\left(HS^\dagger\right) \otimes \mathbb{1}\right)(\mathrm{CiZ})(H \otimes \mathbb{1}). \tag{2.82}$$

We notice that this strategy not only implements a very fast SWAP operation but also should give reasonable fidelities, furthermore since fast single-qubit rotations are required we suggest this method to be used in weakly coupled systems, because there fast single qubit operations are easier to implement.

2.12. Conclusion and Outlook

In this chapter, we showed that optimal control can be used to implement arbitrary gate operations with reasonably high fidelity, in a robust manner. We find that instead of relying on gate decomposition as it is done in earlier works, it is often advantageous, i.e. shorter gate time and potential gain in fidelity, to directly optimize the gate which is needed in an algorithm. This observation is consistent with recent trends in the

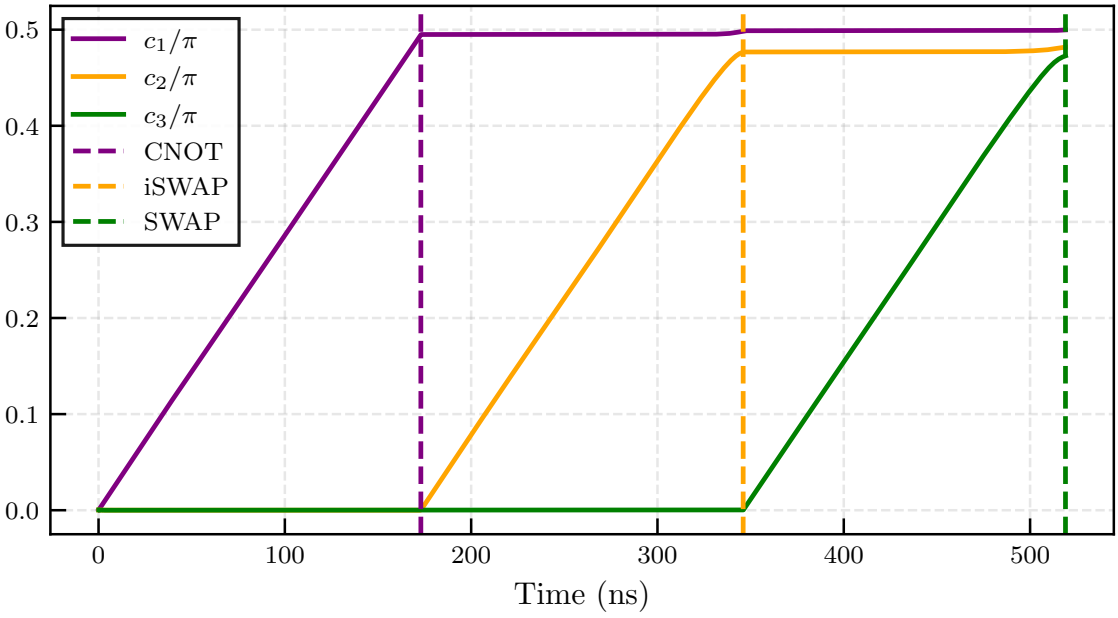

Figure 2.14.: Shown is the evolution of the Weyl coordinates without any drive. At the position of the dashed vertical lines $\tau_{qsl}^{\mathrm{CNOT}}$ and $\tau_{qsl}^{\mathrm{iSWAP}}$ we applied accordingly chosen, instantaneous single-qubit rotations.

quantum computing literature. Additionally, we showed that if all other control constraints are saturated, the limitation of gate times for nonlocal gates is ultimately set by the strength of the interaction. Physically, the shown gate-time bounds reflect the fact that entangling operations require exchange via the interaction terms. In a weak coupling system this exchange becomes very slow compared to local dynamics and therefore waiting strategies combined with fast local operations become preferable. While this is intuitively clear, we also derived exact formulas for the speed limit of the most important two-qubit gates. Summarizing, we learned three important insights: strongly coupled systems are a useful resource for realizing high-fidelity gates. The Larmor frequency and maybe potentially other system parameters should be included in the optimization process, or at least it is a resource to look at. If the system is weakly coupled instead, waiting, combined with fast local operations, might be the best way to implement two-qubit operations.

Building on these results, several avenues for future research emerge to further enhance the capabilities of these systems. One immediate direction involves extending the current methods to address and control multiple ^{13}C nuclear spins. See [Gun+25] where two more ^{13}C spins were found in the discussed setup. This opens the possibility to implement a small quantum register, and thereby enable advanced protocols such as entanglement purification in quantum networks. Furthermore, a photon-nuclear entanglement (PHONE) gate was already demonstrated and used in [Sta+22;

Kna+24]. Larger quantum networks heavily rely on these gates because they enable the possibility of generating entanglement between distant nodes. Together, these improvements can lead to the future realization of a reliable quantum network on a large scale [Kna+24].

3. Noise dependent optimization of few qubit systems

3.1. Motivation

Many quantum devices are solid-state devices, including superconducting quantum chips, quantum dots and vacancy centers in diamond. All of them suffer from slow and correlated noise originating from the coupling to the environment. These noise sources disturb the computational operations and effectively limit the number of computations which can be applied until the information about the gate or the current state of the device is unrecoverable [Reb+09]. Over the last decades, numerous techniques and protocols have been invented to accommodate this type of problem. This includes pulsed protocols such as dynamical decoupling, NMR inspired techniques such as composite pulses and last but not least quantum optimal control in a variety of new algorithms such as GOAT [Mac+15; Mac+18], GRAPE [Kha+05; Sch+05] and dCRAB [Rac+15; Mül+22]. While the community got a better understanding of quantum speed limits and the controllability of quantum systems, there are still open questions such as how can we effectively detect and circumvent the slow, intermediately slow and fast noise, all at the same time. The following chapter is organized as follows, first we shortly discuss a few existing techniques and show their implementation. Afterward, we discuss the application of optimizing single qubit gates under the effect of different noisy environments, show how this technique can be used to optimize a gate for an experimental demonstration in a Germanium vacancy center and round of with the demonstration of optimizing random state transfers in a n-qubit Ising chain.

3.2. Compensation for Off-Resonance with a Pulse Sequence (CORPSE)

The CORPSE family of composite pulses [CLJ03] mitigates first-order off-resonance errors by expanding the single-qubit dynamics in the presence of a constant but unknown detuning and canceling the leading-order contributions. In contrast, composite-pulse schemes such as BB1 target systematic pulse amplitude errors. In the following we show the detailed implementation of CORPSE: For a general controlled Hamiltonian with detuning Δ

$$H(t) = \Omega_x(t)X + \Omega_y(t)Y + \Delta Z \tag{3.1}$$

the target rotation $U(\Theta,\Phi) = \exp\left(-i\frac{\Theta}{2}[\cos(\Phi)X + \sin(\Phi)Y]\right)$ is split into three distinct pulses with equal duration $T/3$:

$$U(\Theta,\Phi) = U(\Theta_3,\Phi_3)U(\Theta_2,\Phi_2)U(\Theta_1,\Phi_1). \tag{3.2}$$

Where the parameters are chosen as:

$$\Theta_1 = \frac{\theta}{2} - \kappa + 2\nu_1\pi \tag{3.3}$$
$$\Theta_2 = 2\nu_2\pi - 2\kappa \tag{3.4}$$
$$\Theta_3 = \frac{\theta}{2} - \kappa + 2\nu_3\pi \tag{3.5}$$
$$\Phi_1 = \phi \tag{3.6}$$
$$\Phi_2 = \phi + \pi \tag{3.7}$$
$$\Phi_3 = \phi \tag{3.8}$$
$$\kappa = \arcsin\left(\frac{\sin(\Theta/2)}{2}\right). \tag{3.9}$$

such that the control takes the form

$$\Omega_k(t) = \begin{cases} \Omega_k^{(1)}, & 0 \le t \le \frac{T}{3}, \\ \Omega_k^{(2)}, & \frac{T}{3} < t \le \frac{2T}{3}, \\ \Omega_k^{(3)}, & \frac{2T}{3} < t \le T, k \in \{x,y\} \end{cases} \tag{3.10}$$

with $\Omega_x^{(j)} = \frac{3\Theta_j}{2T}\cos(\Phi_j)$ and $\Omega_y^{(j)} = \frac{3\Theta_j}{2T}\sin(\Phi_j)$. For short-CORPSE we choose $\nu_1 = 0, \nu_2 = 1, \nu_3 = 0$ [KKK22]. A very nice introduction to the technique and some constructional details can be found in [AJ07]. We use this as a reference point for our optimization strategy, since the so constructed sequence is robust against detuning error Δ which is constant in time for a single realization, but randomly chosen between distinct realizations.

3.3. Gate optimization for a single qubit

We assume to have a single qubit under pure dephasing noise, its dynamics for a single noise realization is described by the Hamiltonian

$$H = \beta_k(t)Z + \Omega_x(t)X + \Omega_y(t)Y, \tag{3.11}$$

where $\beta_k(t)$ is the k-th realization of a random process and $\Omega_k, k \in \{x,y\}$ are the respective control functions. The time evolution U_k for a specific noise realization $\beta_k(t)$ is found by solving the Schrödinger equation for unitaries and average over the super operators induced by U_k, such that the implemented channel is given as

$$S_{\mathcal{E}} = \frac{1}{N}\sum_{k=1}^{N} U_k^* \otimes U_k. \tag{3.12}$$

The goal is to find control functions $\Omega_k, k \in x, y$ such that on average we get as close as possible to a target operator $S_{\mathcal{F}}$ which is usually the superoperator originating from a specific unitary $S_{\mathcal{F}} = U^*_{\text{target}} \otimes U_{\text{target}}$. The closeness is measured by the average gate fidelity, which can be written as

$$F = \frac{\Re(\operatorname{Tr} S_{\mathcal{E}}^{\dagger} S_{\mathcal{F}}) + d}{d(d+1)}, \tag{3.13}$$

where d is the dimension of the underlying Hilbert space. We do the optimization for two different gates, namely the identity operation, such that the qubit state is protected from the influence of the semi-classical noise source, and a NOT operation (X gate). The optimization is performed using the dCRAB algorithm with automatic differentiation and using the gradient descent L-BFGS algorithm. Further details are provided in section 1.8. For the optimization, we use two different strategies, the first is to implement the noise traces from an Ornstein-Uhlenbeck process. This involves generating many random numbers and also needs a high number of realizations until the found channel converges to a stable operator. The second strategy is to work with constant but distributed noise, this has the advantage that less random numbers are needed and therefore less quantum trajectories have to be simulated. In Figure 3.1 and Figure 3.2 we show and discuss the parameters and details of the optimization, once the noise power, i.e. the prefactor in the power spectrum ($\frac{\sigma^2}{2\kappa}$) is kept constant (see Figure 3.1) and once where the decay function of the undriven Ornstein-Uhlenbeck process is constant (see Figure 3.2).

In these figures we compared four different optimization strategies for realizing the identity gate and the Pauli X gate. These are: the naive strategy where we just use a constant pulse to implement the gates, CORPSE, an optimization with constant noise and an optimization with OU noise. In the figures, we evaluate the performance of the so gained pulses against OU noise, constant noise (labeled const OU noise) and random telegraph noise (RTN). We see that in almost all cases the optimized pulses outperform CORPSE and the simple strategy. Interestingly, the pulses which were optimized with random constant noise seem to perform similarly to the ones optimized with the full noise knowledge. The full OU optimization seems to only have an edge for a small regime of very fast noise. In the concluding sections, we want to investigate this further.

3.4. Random N-qubit state transfer

Another task for finding pulses is to implement state transfers efficiently. This is needed for state preparation and allows us to study larger systems. We start with the example of a N qubit Ising chain Hamiltonian which takes the form

$$H = \Omega_x(t) \sum_{i=1}^{N} X_i + \Omega_y(t) \sum_{i=1}^{N} Y_i + \sum_{i=1}^{N} (\Delta_i + \beta_k(t)) Z_i + \sum_{i=1}^{N-1} Z_i Z_{i+1} \tag{3.14}$$

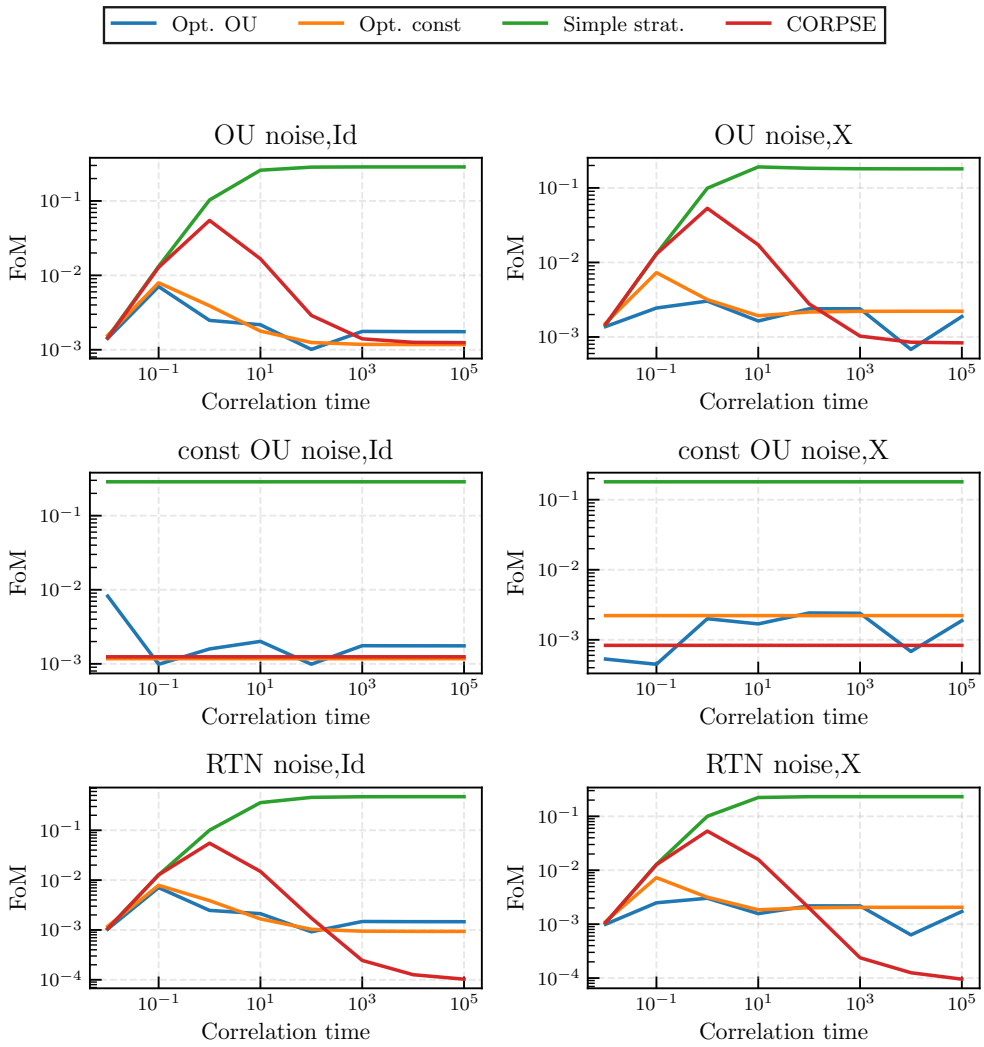

Figure 3.1.: Comparison of different strategies for realizing an identity operation (left) and an X gate (right) under the influence of different noisy environments. The green curves show the reached infidelities for the intuitive solutions (For Id: $\Omega_1 = \Omega_2 = 0$, $X : \Omega_1 = \frac{\pi}{2T}, \Omega_2 = 0$), the red lines show the result for the CORPSE technique, the blue (orange) curves were found by using dCRAB with automatic differentiation under averaging $N = 5000$ OU ($N = 100$ constant) evolutions on an A100 GPU. The noise was designed such that the ratio $\frac{\sigma^2}{2\kappa} = 0.1$ was kept constant, and the 100 constant noise traces were sampled from a normal distribution $\sim N(0, \frac{\sigma^2}{2\kappa})$. For evaluating the RTN noise, the parameters were chosen such that the spectra of the OU-process and the RTN noise coincided. We see that it is most of the time sufficient to optimize with constant noise realizations, since this is enough to integrate a robustness. The parameters for this plot were $T_{\text{gate}} = 10, \mathrm{d}t = 0.01, \left|\Omega^{X,Y}_{max}\right| = 200$ and for the optimization $N_{\text{super}} = 10$ and $N_{\text{basis}} = 5$ sigmoid basis functions per super iteration.

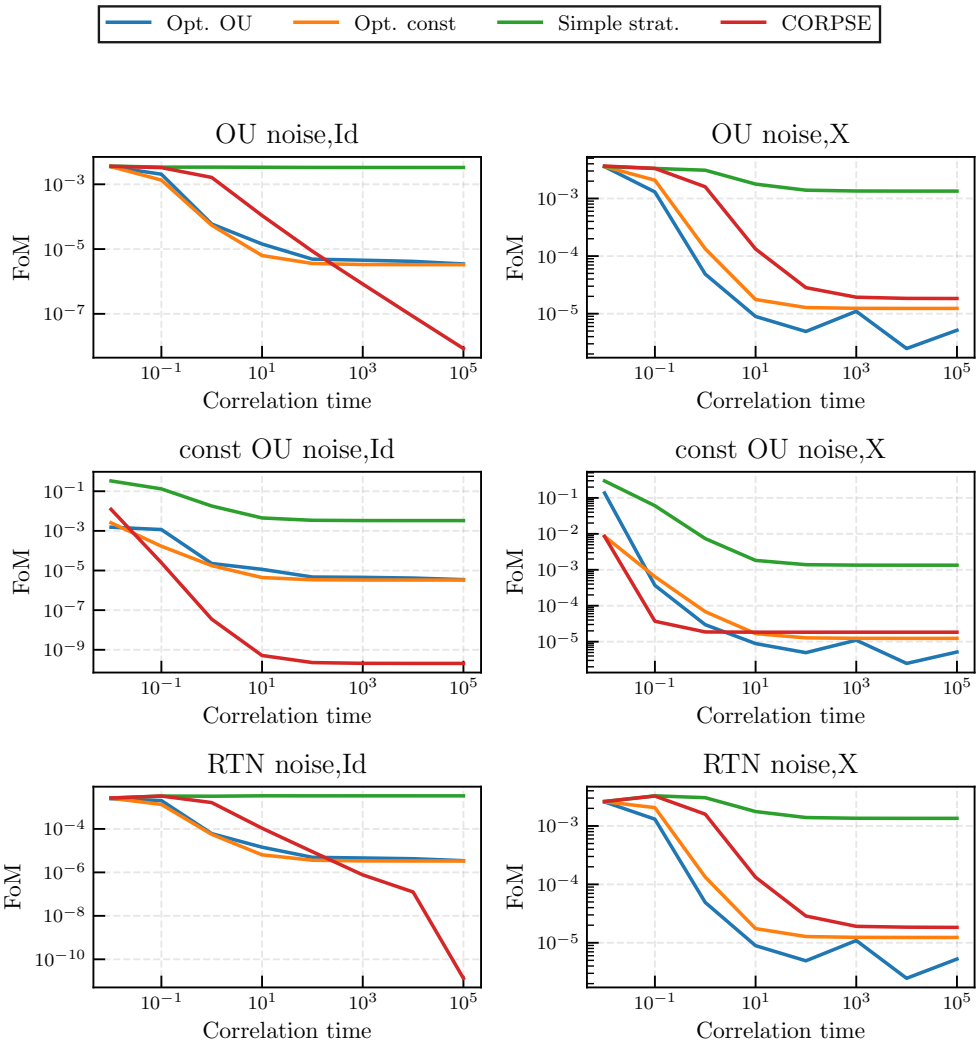

Figure 3.2.: Same as in 3.1 but the condition for the noise amplitude σ was both during the optimization and the evaluation chosen such that the free decay after the gate time without drive was constant, meaning $\frac{2\sigma^2}{\kappa^3}(e^{-\kappa T_{\text{gate}}} + \kappa T_{\text{gate}} - 1) = 1$. This did lower the average noise strength but did not change the observation, that optimizing with constant noise does not perform much worse than optimizing with the full OU process.

where $\Omega_x(t)$ and $\Omega_y(t)$ are the control functions, Δ_i is the frequency of the i-th qubit and $\beta_k(t)$ is a random dephasing field acting globally on every qubit in the same way, this could for example origin from some globally fluctuating magnetic field.
The goal is to optimize a random state transfer where both the initial state and the final state are chosen uniformly out of all possible n qubit states. To measure the success of the optimization, we define the following figure of merit which directly corresponds to the infidelity between the reached state $\rho = \frac{1}{N}\sum_k |\psi_k\rangle\langle\psi_k|$ and the target state $\rho_{\text{target}} = |\psi_{\text{target}}\rangle\langle\psi_{\text{target}}|$:

$$\text{FoM} = 1 - \text{Re}\{\text{Tr}\{\rho\rho_{\text{target}}\}\}. \tag{3.15}$$

From this we use the strategy of optimizing the figure of merit with constant noise and evaluate the resulting pulses against many realizations of the Ornstein-Uhlenbeck process for different correlation times. The results are shown in Figure 3.3. We notice two main things: while the controls were optimized just at the red dot, the resulting pulses are robust also for other correlation rates. Second, we notice that the performance when replacing the constant noise with OU noise does not suffer significantly, indicating again that for finding a good pulse the exact structure of the noise is not important.

3.5. Application: Germanium vacancy center

We redid the optimization of the SWAP gate to show two things, first in section 2.8 we did not go to the limits of the optimization problem because of time constraints and second we wanted to show that optimization with constant noise works equally well. We increased the number of allowed oscillations during the gate time from $n = 10$ to $n = 40$, doubled the number of basis vectors per superiteration and increased the number of function evaluations per superiteration from $N_{\text{eval}} = 1000$ to $N_{\text{eval}} = 5000$. The results are depicted in Figure 3.4.

We observe, that the reached fidelity indeed increased from $F \approx 97\%$ to, $F \approx 99.90\%$ just by the changes made in the optimization process and improved this to $F \approx 99.95\%$ with constant noise optimization. Overall, the optimization with constant noise works comparably well to that of the optimization with the full OU process, which again confirms our main statement that the exact structure of the noise is often not needed for building robust gate implementations.

3.6. Conclusion

In this chapter we have shown, in agreement to previous works, that optimal control offers little to no advantage against fast fluctuating noise, and is very effective against quasi-static, slow noise. From the physics perspective, this can be understood in the following way: noise which is fast compared to the control averages out, and the information contained in the system is reduced. However, if the noise is slow it can be

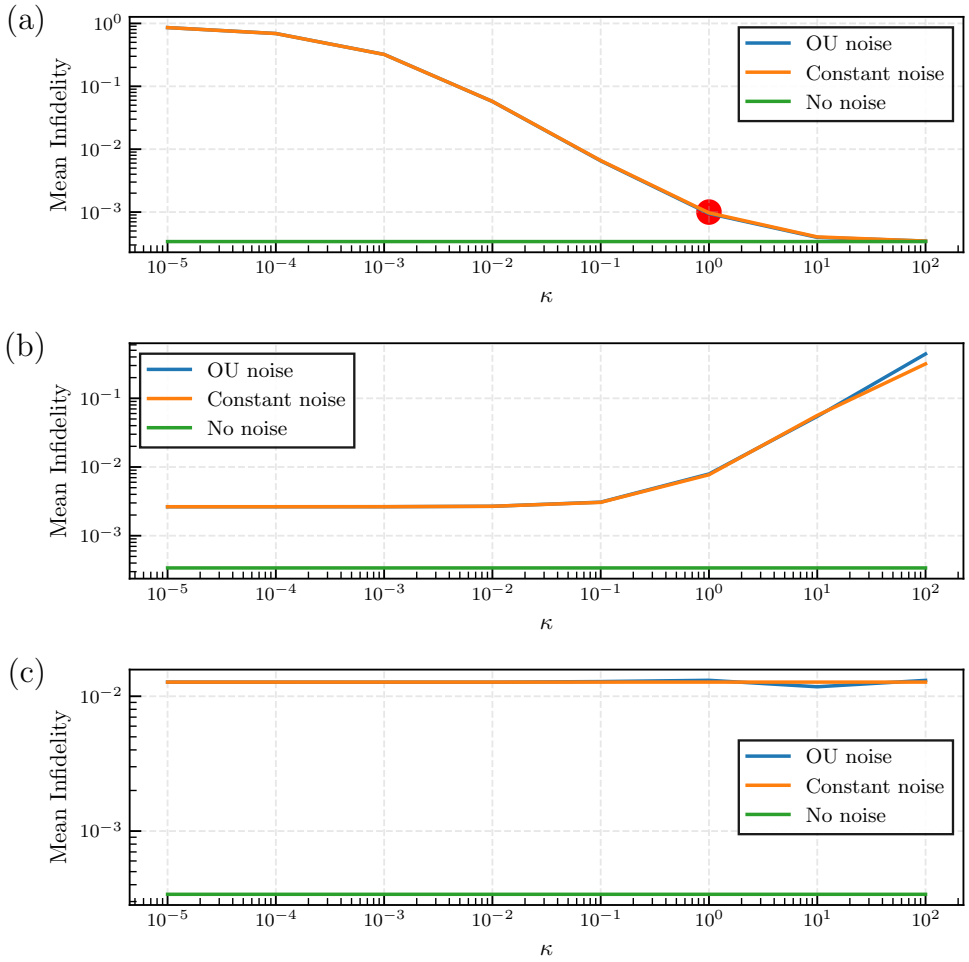

Figure 3.3.: Shown is the average performance (averaged over $m = 10$ random state transfers) of an optimized pulse compared in different noisy environments. In (a) the noise strength is set to $\sigma = 0.1$ and the correlation rate κ is varied. The red dot indicates the noise level at which the pulses were optimized. Each optimization stopped if the reached infidelity dropped below $1 - F = 1 \times 10^{-3}$. (b) shows the average performance of the pulses, while in this case the noise amplitude was chosen such that the decay after the gate time was kept constant, i.e. $\sigma = \sqrt{\frac{\kappa^3}{2(\exp(-\kappa T_{\text{gate}}) + \kappa T_{\text{gate}} - 1)}}$. (c) shows the performance of the pulses while the noise ratio $\frac{\sigma^2}{2\kappa}$ is kept constant, i.e. $\sigma = \sqrt{0.2\kappa}$. We notice two things first optimizing at a single constant noise point, gives robust pulses over a wide range of noise parameters, second the exact structure of the noise does not matter much, but it is enough to optimize over an average of constant detunings for design of robust pulses.

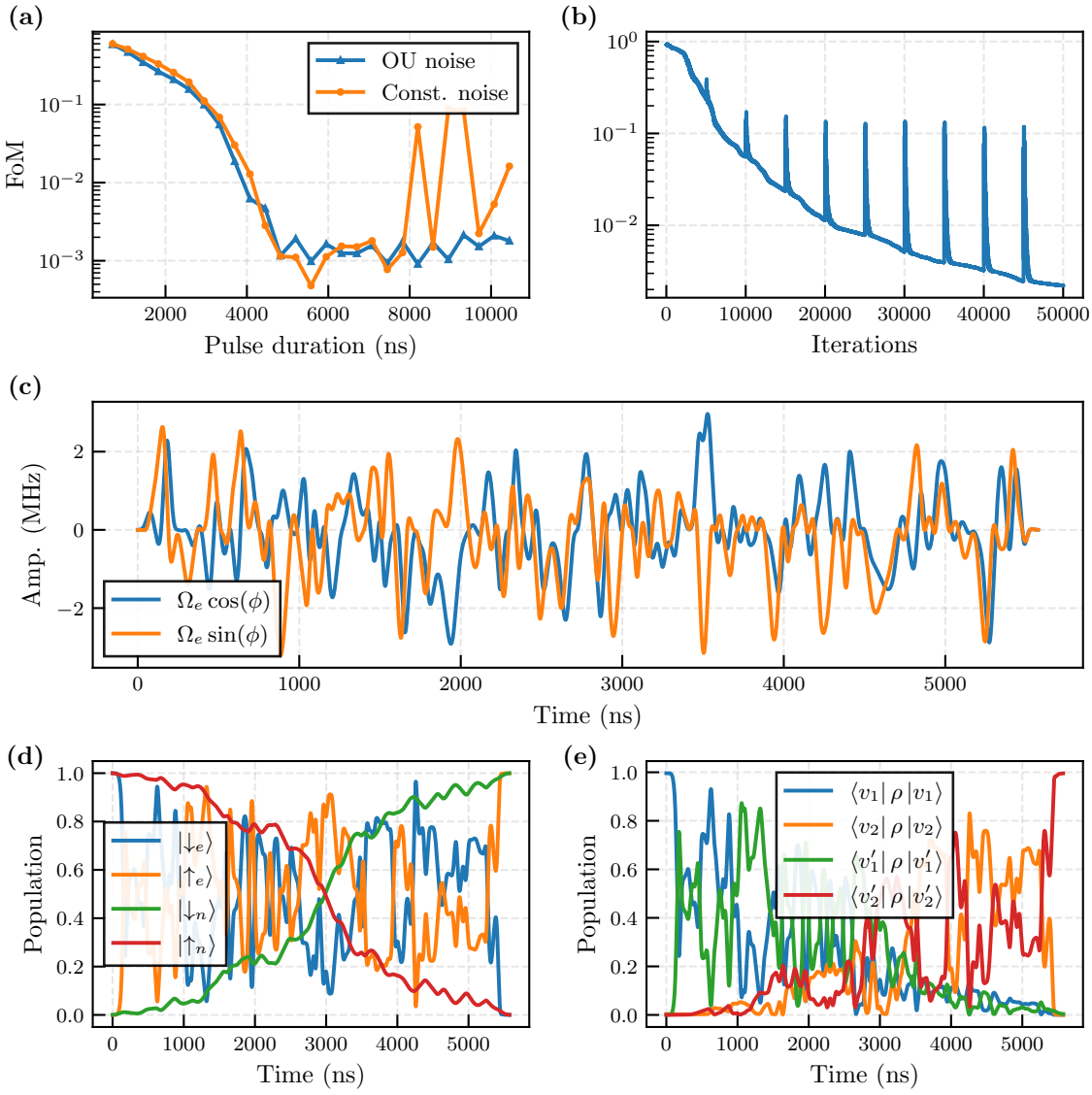

Figure 3.4.: Optimization process of a SWAP gate (a) shows the reached figure of merit for different gate durations, evaluated with 5000 independent OU realizations, ones optimized with OU noise and once with constant noise, the best reached fidelity was $F = 99.95\,\%$ at a gate duration of $5.575\,\mu s$ reached with the pulse which came from the constant noise optimization. (b) is the progress of the optimization for the best reached infidelity (for the constant noise), (c) shows the resulting pulse, (d) the populations tracing out the other spin and (e) the populations in the eigenbasis of the electron.

interpreted as an effective parameter shift, which can be corrected or accounted for. Additionally, we have shown that between the two extreme cases of very fast and very slow or even constant noise, there is not much room for optimal control to leverage the structure of the underlying noise correlations. While this is mostly a new but negative result for using optimal control in the intermediate noise regime, it at least gives a clear instruction plan on choosing the suitable control strategy dependent on the noise correlation timescale.

As a positive result, at least from a numerical perspective, we found out that while the exact structure of noise is physically eventually interesting, the full knowledge is not needed for reducing its impact. Indeed, for the intermediate correlation time regime, the shown examples suggest making the found solution robust by incorporating constant shifts into the optimization process. Summarizing, we found that against fast noise we can essentially do nothing but being faster or use error mitigation [Cai+23], for slow noise we can incorporate techniques such as CORPSE or dynamical decoupling and for the intermediate regime we propose robust pulse optimization by adding multiple, constant parameter shifts.

Overall, the found results imply that future work should focus less on exploiting temporal noise structure, but instead on choosing the control strategy accordingly to the noise timescale. Another interesting research direction would be to focus on deriving analytic performance limitations considering interaction strength, noise correlation timescale and noise strength.

4. Superconducting qubit/Nanowire

4.1. Motivation

Superconducting qubits are a leading platform for quantum computing due to their excellent coherence and controllability properties [Kja+20; Kra+19; Sid21]. Recent research has made significant progress in developing bigger and more reliable superconducting quantum circuits [NKa24; Abu25]. One of the interesting platforms are qubits based on superconducting nanowires because they may include Majorana zero modes, which Microsoft recently claimed to use for their scalable quantum computing chip [Agh+25; Aas+25]. These are theoretical quasi-particles, which might provide robustness against local decoherence due to topological protection, making them a candidate for fault-tolerant quantum computing. This chapter should provide an introduction to key concepts and models necessary for characterizing these kinds of quantum circuits. It is structured in the following way, first we derive and discuss the model of a Cooper-Pair-Box, including noise simulation. Afterward, we characterize the experiment and choose the model parameters such that we can reproduce the experimental data. Next, we show how the system can be operated, do gate optimizations for single qubit gates and discuss different strategies to detect the parity state of the system.

4.2. Experimental Setup

The experimental setup is in detailed explained in Figure 1 and Appendix A of [Kra+24]. Here, we just give a short summary of what is published there. The system consists of a 3D transmon embedded in a copper cavity, with dispersive readout and gate biasing to enable charge dispersion measurements. The transmon is realized as a SQUID with asymmetric Al/AlOx/Al tunnel junctions, leading to different superconducting gaps across the junction. A vector magnet provides both flux bias and in-plane magnetic field control, enabling exploration of parity switching under magnetic fields of up to $B = 0.41\,\mathrm{T}$. To probe single-quasiparticle tunneling events (parity changes), Ramsey-type pulse sequences are employed on charge-sensitive transitions, from which parity lifetimes are extracted. The measured lifetimes show a non-monotonic dependence on the in-plane field, with a maximum around $B = 0.2\,\mathrm{T}$, consistent with competing quasiparticle tunneling and photon-assisted pair-breaking mechanisms. Additional temperature-dependent measurements reveal a cascade-like reduction of parity lifetime beginning already near 50 mK [Kra+24].

4.3. General derivation of a model for superconducting qubits

To provide some intuition about superconducting circuits, we start with an introductory derivation of the energy relations for several relevant circuits, thereby arriving at a model that describes our experiment. The section follows the corresponding chapter in [Kra+19].

4.3.1. Harmonic Oscillator

The simplest electronic system is an LC-circuit, which contains only a capacity C and an inductance L as components. We can calculate the energy of each component E_C, E_L by integrating the power of each component over time.

$$E^{L/C}(t) = \int_{-\infty}^{t} dt' V^{L/C}(t') I^{L/C}(t'). \tag{4.1}$$

where $V^{L/C}(t')$ and $I^{L/C}(t')$ "denote the voltage and current of the capacitor or inductor" [Kra+19, p.3]. We introduce our generalized coordinate flux via

$$\Phi^{L/C}(t) = \int_{-\infty}^{t} V^{L/C}(t') dt'. \tag{4.2}$$

Now, we define $V^{L/C} = L\frac{dI^{L/C}}{dt}$ and $I^{L/C} = C\frac{dV^{L/C}}{dt}$. With these we can write the potential and kinetic energy of the system as

$$\mathcal{T}_C = \frac{1}{2} C \dot{\Phi}^2 \tag{4.3}$$

$$\mathcal{V}_L = \frac{1}{2L} \Phi^2. \tag{4.4}$$

The Lagrangian of the system can now be calculated as

$$\mathcal{L} = \mathcal{T}_\mathcal{C} - \mathcal{V}_\mathcal{L} \tag{4.5}$$

$$= \frac{1}{2} C \dot{\Phi}^2 - \frac{1}{2L} \Phi^2. \tag{4.6}$$

We define the charge Q as the conjugate variable of the flux:

$$Q = \frac{\partial \mathcal{L}}{\partial \dot{\Phi}} \tag{4.7}$$

$$= C\dot{\Phi}. \tag{4.8}$$

Therefore, the Hamiltonian of our LC-circuit can now be written as

$$H = Q\dot{\Phi} - \mathcal{L} = \frac{1}{2C} Q^2 + \frac{1}{2L} \Phi^2. \tag{4.9}$$

If we introduce the reduced flux $\phi = 2\pi\frac{\Phi}{\Phi_0}$ and the reduced charge $n = \frac{Q}{2e}$ we can rewrite this Hamiltonian as

$$H = 4E_C n^2 + \frac{1}{2}E_L\phi^2, \tag{4.10}$$

"where $EC = e^2/(2C)$ is the charging energy required to add each electron of the Cooper-pair to the island and $E_L = \frac{\Phi_0^2}{4\pi^2 L}$ is the inductive energy, where $\Phi_0 = h/2e$ is the superconducting magnetic flux quantum" [Kra+19, p.4].
Reformulating this in second quantization with $\omega_r = \sqrt{8E_L E_C}/\hbar$ the Hamiltonian takes the well known form of a harmonic oscillator

$$H = \hbar\omega_r(a^\dagger a + \frac{1}{2}) \tag{4.11}$$

where we used the definitions

$$n = i[E_L/(32E_C)]^{\frac{1}{4}}(a - a^\dagger) \tag{4.12}$$

$$\phi = [2E_C/E_L]^{\frac{1}{4}}(a + a^\dagger). \tag{4.13}$$

or equivalently

$$a = \sqrt[4]{\frac{E_L}{32E_C}}\Phi - \mathrm{i}\sqrt[4]{\frac{2E_C}{E_L}}n. \tag{4.14}$$

This first simple model contains already quantum levels and introduces creation and annihilation operators to switch between them. However, the levels are all separated by the same energy $E_r = \hbar\omega_r$ and can therefore not be addressed individually, disabling the possibility of implementing individual quantum bits.

4.3.2. Josephson circuit

To solve the problem of individual addressability of the energy levels in the harmonic oscillator, we have to introduce some non-linear component into our circuit. One way of doing this is to replace the linear inductance of the quantum harmonic oscillator by a Josephson junction. Such a component is described by the Josephson relations

$$I = I_C \sin(\phi) \tag{4.15}$$

$$V = \frac{\hbar}{2e}\frac{\mathrm{d}\phi}{\mathrm{d}t}. \tag{4.16}$$

We can use Equation (4.1) to see that the energy of the replaced inductor E_J is now given through,

$$E^J(t) = \int_{-\infty}^{t} V(t')I(t')dt' \tag{4.17}$$

$$= \int_{-\infty}^{t} \frac{I_c \hbar}{2e} \sin(\phi(t'))\dot{\phi}(t')dt' \tag{4.18}$$

$$= -\frac{I_c \hbar}{2e} \cos(\phi). \tag{4.19}$$

Therefore the Hamiltonian of the Cooper-Pair-Box takes the form

$$H = 4E_C n^2 - E_J \cos(\phi) \tag{4.20}$$

where $E_C = e^2/2(C_s + C_J)$ and $E_J = I_c \Phi_0 / 2\pi$.

By tuning E_J and E_C we can differentiate between different regimes with different properties. We will now go through these possible choices and discuss the properties of the different designs.

4.3.3. Transmon

Choosing $C_s \gg C_J$ is resulting in an energy regime $E_J \gg E_C$ (typically $E_J/E_C \approx 10$), which makes the circuit less sensitive to charge noise, because the circuit behaves in this regime much more like an inductive element and not like a capacity. This design is called transmon qubit or just transmon and had tremendous success in the field of quantum computation because it effectively suppresses flux noise [Koc+07].

To understand this design a bit better, we rewrite the Hamiltonian in terms of creation and annihilation operators

$$\hat{\phi} = \sqrt{\eta}(\hat{a}^\dagger + \hat{a}) \tag{4.21}$$

$$\hat{n} = \frac{\mathrm{i}}{2\sqrt{\eta}}(\hat{a}^\dagger - \hat{a}) \tag{4.22}$$

where $\eta = \sqrt{2E_C/E_J}$ is a dimensionless smallness parameter of the perturbation Ansatz for the harmonic oscillator. Since we will most likely not excite any state higher than the 3rd energy level, we can assume that the operators are bounded through

$$\|a\| \leq \sqrt{3} \tag{4.23}$$

$$\left\|a^\dagger\right\| \leq \sqrt{3}. \tag{4.24}$$

With this bound we perform a Taylor expansion of the cosine from Equation (4.20) up to the fourth order (this is valid because $E_J \gg E_C$) and get

$$H \approx \omega_q a^\dagger a + \frac{\alpha}{2} a^\dagger a^\dagger a a. \tag{4.25}$$

Where $\omega_q = (\sqrt{8E_J E_C} - E_C)/\hbar$ is the qubit frequency and $\alpha = -E_C$ is called its anharmonicity.

A more detailed description of this calculation and other models can be found in [Jon+21]. To give a reason that you have to be cautious with such approximations we will now show how many orders we have to include for sufficient convergence, if we assume to guess the qubit frequency with a precision of at least $\Delta f_{max} = 1\,\mathrm{MHz}$. This means that we have to (dependent on the ratio E_C/E_J) include many different orders. The error we make by expanding the cosine to $2k$-th order is given as

$$R_{2k+2}(\phi) = |T_{2k}\cos(\phi, 0) - \cos(\phi)| \tag{4.26}$$

$$\leq \frac{|\phi|^{2k+2}}{(2k+2)!} \tag{4.27}$$

$$= \frac{(2\sqrt{3\eta})^{2k+2}}{(2k+2)!} \overset{!}{\leq} \omega_{max}\hbar/E_J, \tag{4.28}$$

where R_{2k+2} denotes the error of the $2k$-th Taylor expansion T_{2k}. For example, if our ratio is $\eta = 10$ and $E_J \approx 1 \times 10^{-22}\,\mathrm{J}$ we would have to include at least

$$\frac{2\sqrt{30}^{2k+2}}{(2k+2)!} \leq 6.7 \times 10^{-6} \tag{4.29}$$

$$\Rightarrow k \approx 18 \tag{4.30}$$

terms in our calculation demonstrating that one should either consider a higher E_J/E_C-ratio or use different ways of computing the energies. While transmons are in general more insensitive to charge noise, it comes at the cost of decreased anharmonicity leading to longer gates and more leakage into unwanted levels. However, there exist techniques like optimal control to counteract these disadvantages.

4.3.4. Charge qubit

A charge qubit operates in the regime $E_C \gg E_J$. If the ratio is large enough, we can completely neglect the Josephson energy, which leads to a trapping of the Cooper pairs on the superconducting island. The Hamiltonian then takes the form

$$H_{cq} \approx E_C(n - n_g)^2. \tag{4.31}$$

Using again the ladder operator representation this can be rewritten as

$$H_{cq} \approx -\frac{1}{2}\big(\epsilon(aa^\dagger - a^\dagger a) + \Delta(a + a^\dagger)\big) \tag{4.32}$$

$$= -\frac{1}{2}\big(\epsilon\mathbb{1} + \Delta(a + a^\dagger)\big) \tag{4.33}$$

with $\epsilon = -2\sqrt{E_J E_C/8}$ and $\Delta = -\mathrm{i}n_g\sqrt{8E_J E_C}$. Instead, projecting the full Cooper-Pair-Box Hamiltonian onto the two charge states $|0\rangle, |1\rangle$ leads to the very simple, but also very well known expression

$$H_{cq} \approx -\frac{1}{2}(\epsilon\sigma_z + \Delta\sigma_x) \tag{4.34}$$

where $\epsilon = E_C(1 - 2n_g)$ and $\Delta = E_J$, showing again how careful we have to be if a harmonic approximation is justified.

However, even though this seems to be an easily controllable system, the leading energy contribution E_C is highly affected by charge noise which is hard to circumvent because it is present in all electric devices and therefore is in terms of coherence outperformed by transmon designs. Instead, the system can be used as a great quasi particle detection tool.

4.3.5. Quantronium

There have been made many attempts to improve the transmon design in coherence. One approach was to combine multiple junctions. For example, the quantronium design included two small junctions in a loop with a larger junction. Its Hamiltonian is given as [Sid+06]

$$H_{\text{qtr}} = 4E_C\left(\hat{n} - \frac{1}{2} + \frac{C_g U(t)}{2e}\right) - E_J \cos\left(\frac{\hat{\delta}}{2}\right)\cos\left(\hat{\Theta}\right), \tag{4.35}$$

where $\hat{\delta}$ and $\hat{\Theta}$ are the generalized positions. The so gained increase in parameters can be tuned such that if the device is operated at its sweet spot it is both first-order insensitive to charge and flux fluctuations, leading to an increased coherence. However, the design complexity (three instead of one junction) and the sensitivity apart from the sweet spot made it less attractive in terms of scalability.

4.3.6. Cooper-Pair-Box (CPB)

The design of the intermediate regime $E_J \approx E_C$ is often referred to as Cooper-Pair-Box qubits. This design is also sensitive to charge noise, which leads to strong dephasing and therefore short T_2^* times, indicating that transmons perform way better regarding stability and gate fidelity [NPT99; Ith+05; Pal+14].
However, the increased charge sensitivity can also be advantageous for charge sensing and for studying quasi particle effects [Aum+04]. In the subsequent sections, we will use this model (with a few modifications) to describe an experiment which tries to detect the parity state of a nanowire system at the University of Cologne.

Analytic expression for the energy states

Because we cannot use any harmonic approximations because of the E_J/E_C ratio, we have to find different ways of calculating the systems energies. We start again with the CPB Hamiltonian Equation (4.20) which has the form

$$H_{CPB} = 4E_C(\hat{n} - n_g)^2 + E_J \cos(\hat{\varphi}). \tag{4.36}$$

With $[\hat{\varphi}, \hat{n}] = i$, the phase representation leads to the differential equation

$$\left[4E_C\left(-\frac{\partial^2}{\partial\varphi^2} + 2in_g\frac{\partial}{\partial\varphi} + n_g^2\right) - E_J\cos(\varphi)\right]\psi(\varphi) = E\psi(\varphi). \tag{4.37}$$

The static Schrödinger equation is solvable analytically in terms of Mathieu functions in the following way. First we make the Ansatz

$$\tilde{\psi}(\varphi) = \mathrm{e}^{-\mathrm{i}\varphi n_g}\psi(\varphi). \tag{4.38}$$

Then we have

$$\frac{\partial}{\partial\varphi}\tilde{\psi} = -\mathrm{i}n_g\mathrm{e}^{-\mathrm{i}n_g\varphi}\psi(\varphi) + \mathrm{e}^{-\mathrm{i}n_g\varphi}\frac{\partial}{\partial\varphi}\psi(\varphi) \tag{4.39}$$

and therefore

$$\frac{\partial^2}{\partial\varphi^2}\tilde{\psi} = \mathrm{e}^{-\mathrm{i}n_g\varphi}\left[\frac{\partial^2}{\partial\varphi^2} - 2in_g\frac{\partial}{\partial\varphi} - n_g^2\right]\psi(\varphi). \tag{4.40}$$

If we put this back in our differential equation and multiply it with $\mathrm{e}^{-\mathrm{i}n_g\varphi}$ from the left we get

$$\left[-4E_C\frac{\partial^2}{\partial\varphi^2} - E_J\cos(\varphi)\right]\tilde{\psi}(\varphi) = E\tilde{\psi}(\varphi). \tag{4.41}$$

This is a known differential equation and the eigenenergies are given by Mathieu functions

$$E_n = E_C\mathcal{M}_A\left(\mu_n, -\frac{E_J}{2E_C}\right) \tag{4.42}$$

and the wave functions can be expressed as [Did+18]

$$\tilde{\psi}_n(\varphi) = \frac{1}{\sqrt{2\pi}}\left[\mathcal{M}_C\left(\frac{E_n}{E_C}, -\frac{E_J}{2E_C}, \frac{\varphi}{2}\right) - \mathrm{i}^{2n+1}\mathcal{M}_S\left(\frac{E_n}{E_C}, -\frac{E_J}{2E_C}, \frac{\varphi}{2}\right)\right]. \tag{4.43}$$

where "$\mathcal{M}_A$ is the Mathieu characteristic value, $\mathcal{M}_\mathcal{C}$ is the even Mathieu function, $\mathcal{M}_S$ is the odd Mathieu function, and $\mu_n = (-1)^{n+1}n + [n_g \bmod 2]$ the indexes for the eigenenergies" [Did+18, p.2].

Numeric approximation

Instead of solving the eigenvalue problem analytically, we can also use a numeric method. This is especially needed because the Mathieu functions are not easy to evaluate, and they depend heavily on the boundary conditions. Therefore, we move to the so-called charge basis, where we count the number of charges on the island in terms of cooper-pairs. The charge operator is defined in this representation as

$$\hat{n}\,|N\rangle = N\,|N\rangle \tag{4.44}$$

$$\Rightarrow \hat{n} = \sum_{N=-\infty}^{\infty} N \left|N\right\rangle\!\left\langle N\right| . \tag{4.45}$$

Because $\hat{\phi}$ and $\hat{n}$ are conjugated variables, they obey the commutation relation $[\hat{\phi}, \hat{n}] = -i$. Which we can use to see that $e^{i\hat{\phi}} \hat{n} e^{-i\hat{\phi}} = N + 1$. This is useful because we can now find the expression

$$\hat{n} e^{-i\hat{\phi}} \left|N\right\rangle = e^{-i\hat{\phi}} e^{i\hat{\phi}} \hat{n} e^{-i\hat{\phi}} \left|N\right\rangle \tag{4.46}$$

$$= (N+1) e^{-i\hat{\phi}} \left|N\right\rangle \tag{4.47}$$

$$\Rightarrow e^{-i\phi} \left|N\right\rangle = \left|N+1\right\rangle . \tag{4.48}$$

This allows us to reformulate the cosine of the phase operator in the charge basis, as

$$E_J \cos(\phi) = -\frac{E_J}{2} \sum_{N=-\infty}^{\infty} \left(\left|N\right\rangle\left\langle N+1\right| + \left|N+1\right\rangle\left\langle N\right|\right) . \tag{4.49}$$

We can then truncate this representation and diagonalize the resulting Hamiltonian. The eigenenergies are now given by the eigenvalues of the resulting matrix, and the populations in the energy basis can be calculated by projections to the respective eigenspace. This approach yields good agreement with existing theory and gives convergence within $N = 20$ included symmetrical levels. However, recent developments showed that there are small discrepancies in the level splitting and one might include higher orders of charge tunnelling. The adjusted Hamiltonian in this case takes then the form

$$\hat{H} = 4E_C(\hat{n} - n_g)^2 + \sum_{k=1}^{\infty} E_{J,k} \cos\left(k\hat{\phi}\right). \tag{4.50}$$

where $E_{J,k}$ is the k-th Josephson energy, which has alternating sign. Nevertheless, it is often sufficient, to just include one or two orders. In the charge basis, this can then be written as

$$\hat{H} = \sum_{N=-\infty}^{\infty} N \left|N\right\rangle\!\left\langle N\right| - \sum_{k=0}^{\infty} \frac{E_{J,k}}{2} \sum_{N=-\infty}^{\infty} \left(\left|N\right\rangle\left\langle N+k\right| + \left|N+k\right\rangle\left\langle N\right|\right) . \tag{4.51}$$

4.4. Specifics of the Cooper-Pair-Box setup

4.4.1. Dispersion relation and driving the system

First, we look at how the E_C/E_J ratio affects the system's energy levels. In figure Figure 4.1, we vary the E_J/E_C-ratio and the plot the four lowest energy eigenlevels dependent on n_g. We can also measure the qubits frequencies in the experiment to gain insight to the existent E_J/E_C-ratio.

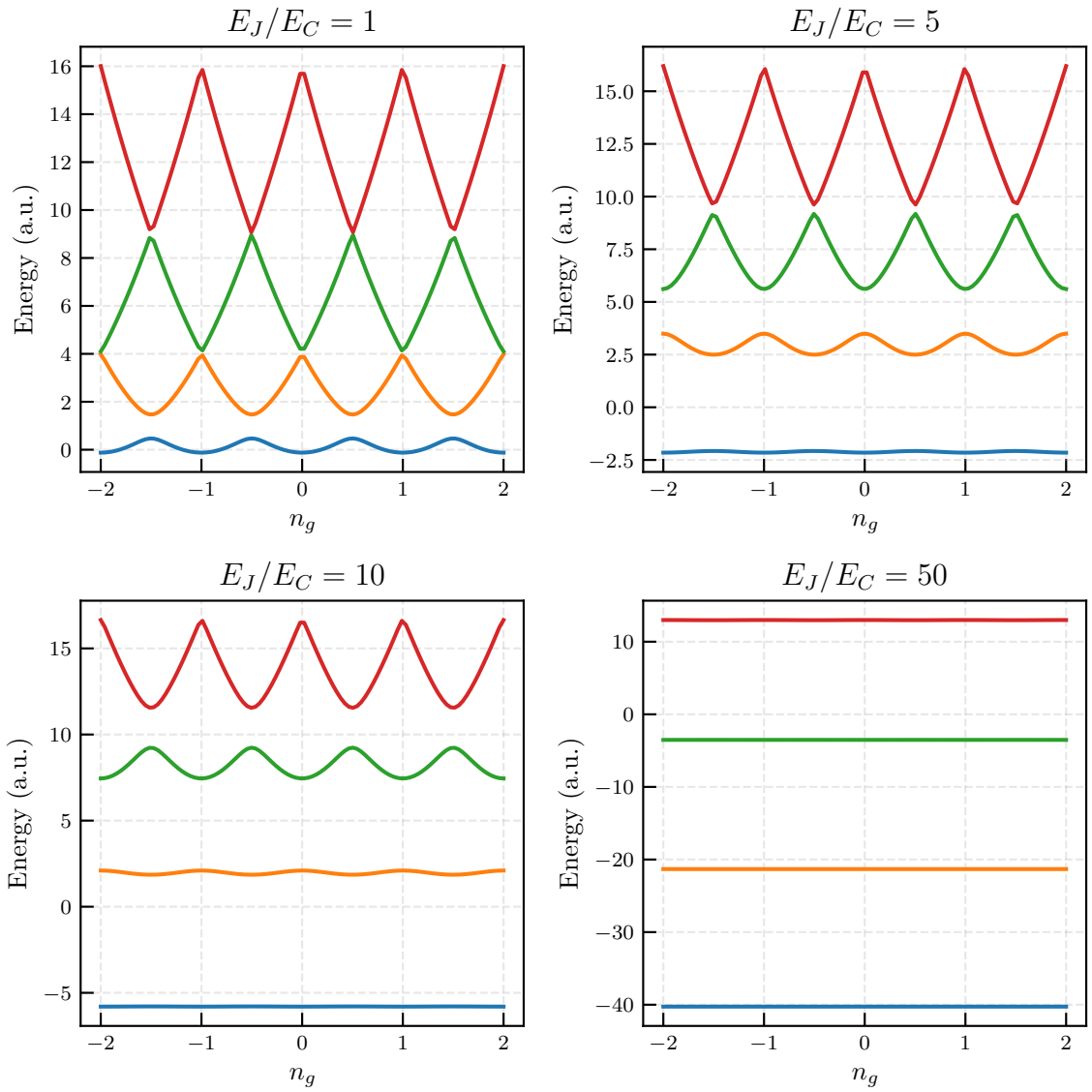

Figure 4.1.: Shown is the dispersion relation of the Cooper-pairbox with only the four lowest Josephson-energy considered for different E_J/E_C-ratios. The top left plot corresponds to a Cooper-Pair-Box setup, the upper right plot shows some intermediate regime and the lower row is in the transmon regime. While the transmon is clearly insensitive to charge fluctuations in n_g, the price paid is loosing anharmonicity and interesting dynamics.

4.4.2. Dynamics

In reality, there are noise sources disturbing our ideal system. In order to simulate this behavior, we have to adjust our model in such a way that it can reproduce data from a real world experiment. In this chapter, we will introduce methods of simulating (quantum) noise. The first method averages over certain noise realizations, which will be either implemented by approximating a given spectrum by two level fluctuators (with a Lorentzian spectrum) or generate a time series directly from a spectrum by using inverse Fourier transformation with random phases.

Another method of introducing (Markovian) noise is to do a Lindblad evolution. We will here do a combination of those two with the benefit of still being able to model non-Markovian dynamics and at the same time let some experimental insights like T_1, T_2^* influence the system, but have the drawback of computationally costly time evolution.

4.4.3. Charge Noise

Charge noise is probably generated by charges sitting at the surface of electronic devices and shows normally a pink power spectrum [Chr+19]. For example, in electron transistors (SETs) and first generation charge qubits the power-spectrum has the form $S(\omega) = A/f^\alpha$ with $\alpha = 1.0 - 1.25$ and a noise magnitude of $S(1\,\mathrm{Hz}) = 10^{-5}$–$10^{-7}\,\mathrm{e}^2/\mathrm{Hz}$. Charge noise directly influences the n_g-parameter in our Hamiltonian. We will simulate it by setting

$$n_g = n_g^p + n_g^n(t) + n_g^d(t). \tag{4.52}$$

Where $n_g^p = 0 \vee n_g^p = 0.5$ define the even/odd parity case (because the number of electrons on the island is even or odd), $n_g^n(t)$ is a single noise realization which can be treated as a random field and $n_g^d(t)$ is the signal we apply via an external voltage. In Figure 4.2 we compare the measured and generated noise spectra. The algorithms to generate the noise traces are found in Appendix A.2.

4.4.4. Flux noise

Flux noise has a smaller influence on our system, especially if the system is operating at the sweet spot $n_g^0 = 1/2$. This is why we will not consider it here. However, in other situations, one might simulate flux noise by treating E_J as a non-constant system parameter.

4.4.5. Parity noise

Parity noise is most likely induced by the creation of quasi particles (QP) by high energy radiation [Pan+22; Liu+24]. In difference to charge noise, the effect of parity noise is not only to shift n_g by 1/2, but also to relax the underlying qubit. However,

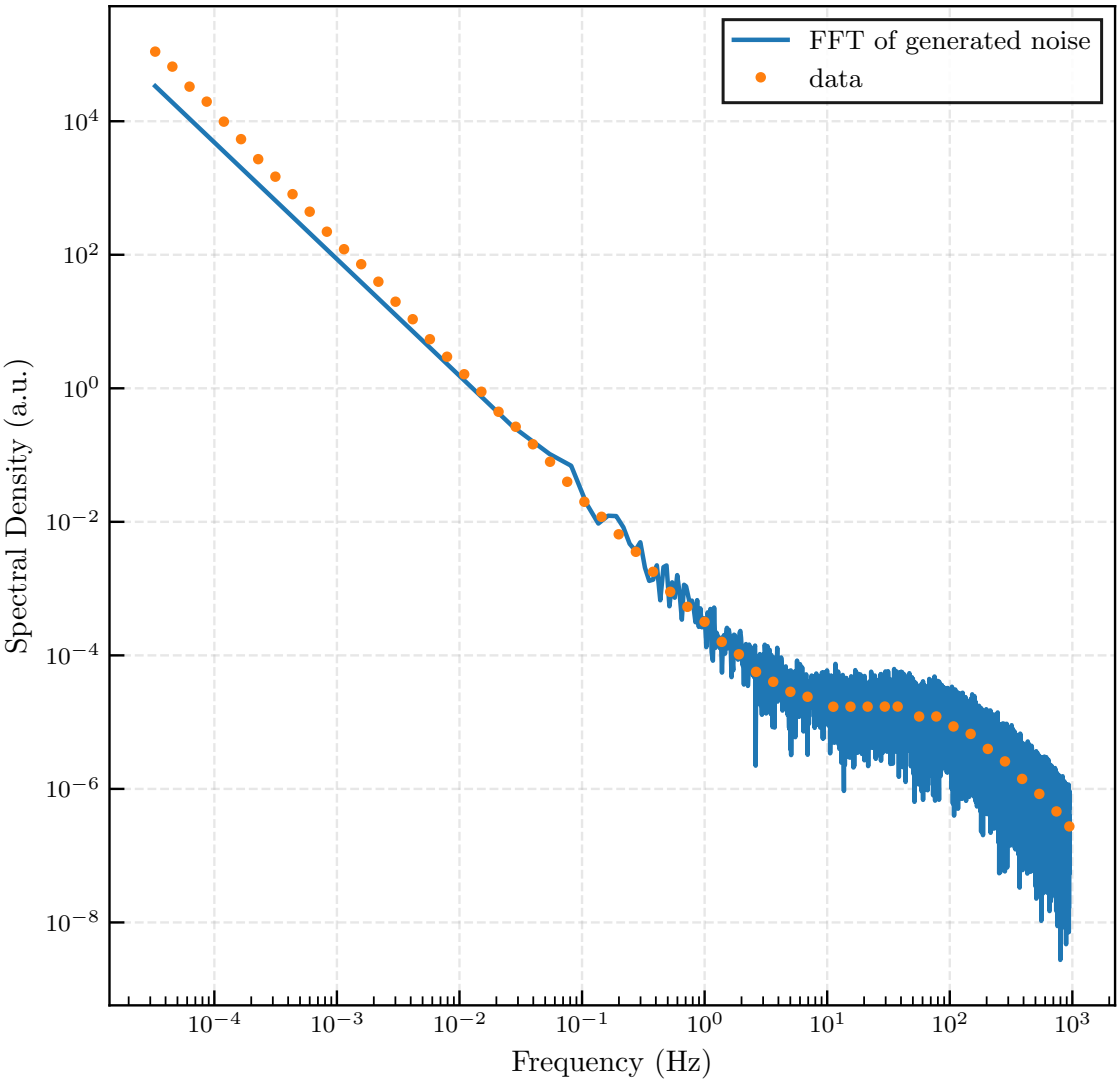

Figure 4.2.: Comparison of measured vs simulated charge noise spectral density, the simulation noise traces were generated via inverse Fourier transform with random uniform phases. While the simulated noise seems to capture the overall behavior, for very low frequencies, the simulated gate time is not enough to have enough data to sample, which explains the deviation from the original data.

the power spectrum of QP parity noise is also given in [Chr+19] and we can do a fit with a single Lorentzian spectrum. The fit with its parameters is shown in Figure 4.3.

4.5. Emulating the experiment

4.5.1. Hamiltonian

We let $N = 10$ be the number of charge values we look at in the simulation of the CPB-Hamiltonian. Then the truncated CPB-Hamiltonian with two Josephson energies takes the form

$$H = 4E_C \sum_{j=-N}^{N} (j - n_g)^2 \, |j\rangle\langle j| - \frac{E_{J,1}}{2} \sum_{j=-N}^{N} |j+1\rangle \langle j| + |j\rangle \langle j+1| \tag{4.53}$$

$$+ \frac{E_{J,2}}{2} \sum_{j=-N}^{N} |j+2\rangle \langle j| + |j\rangle \langle j+2| \,, \tag{4.54}$$

where the energy parameters of the experiment are $E_J = 12.35\,\mathrm{MHz} \times 2\pi$, $E_C = 323\,\mathrm{MHz} \times 2\pi$ and $E_{J,2} = -8 \times 10^{-4} E_{J,1}$. We set $n_g^0 = 0$ and calculate with $n_g^p = 0 \vee n_p^0 = 0.5$ the Hamiltonian of the even/odd parity case in the charge basis. These two do in general not commute, which means that the diagonalization of the Hamiltonians for both parities will result in different energy basis with different eigenenergies. However, after we (numerically) diagonalize the Hamiltonian such that

$$H_{e/o}^E = V_{e/o} H_{e/o}^Q V_{e/o}^\dagger. \tag{4.55}$$

We keep all eigenvectors for later usage but cut the number of levels we look at to the lowest four energy eigenvalues, because higher energy levels are very unlikely to be populated.

4.5.2. Characterization of the system

To get a better understanding of the system, we will introduce here a few techniques that we can apply to characterize our system. We will discuss resonances, subspace operations as well shaping and optimization of pulses.

4.6. Controlling the system

As control, we can use an external voltage which can drive a specific transition of the system. One simple way to accomplish this would be to set the signal of the voltage to

$$V(t) = V_0 \cos(\omega_d t + \phi). \tag{4.56}$$

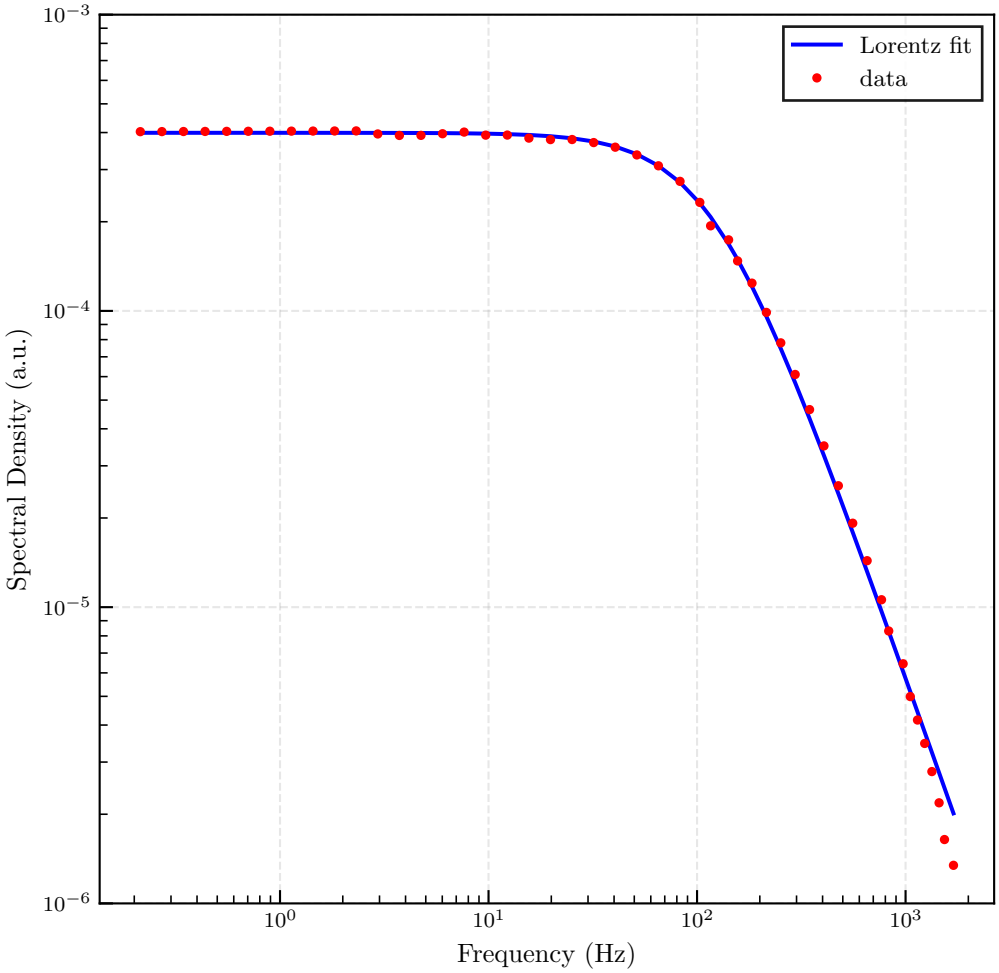

Figure 4.3.: Spectral density of parity shot noise (red). The blue curve shows a Lorentzian fit, which can be simulated by charge flips of a two level fluctuator.

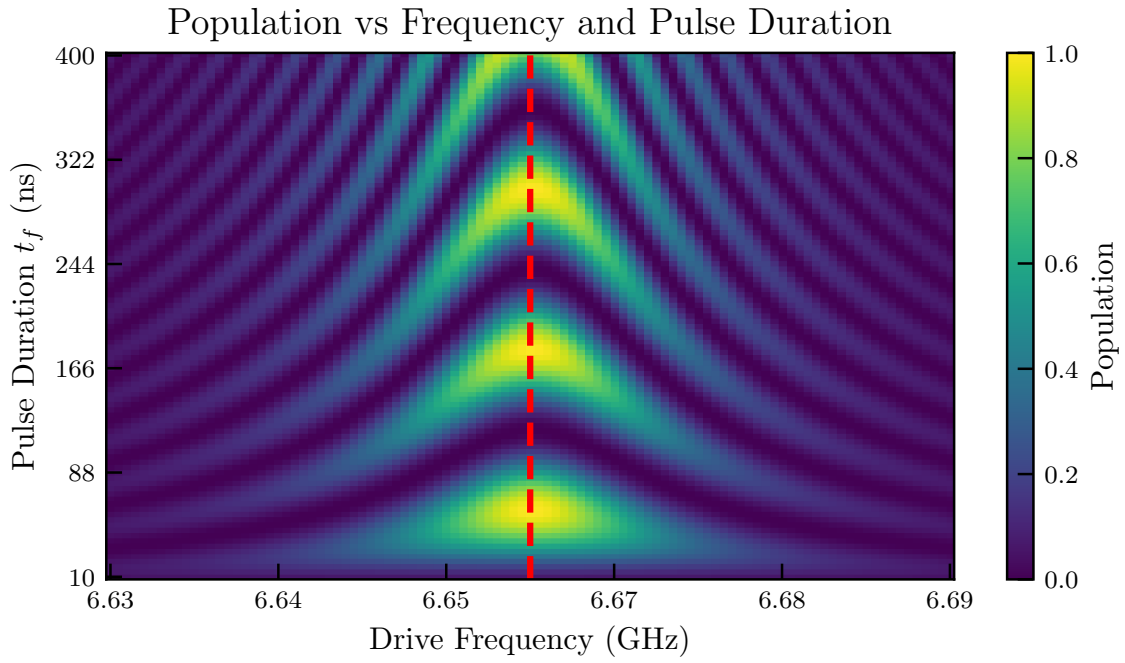

Figure 4.4.: Time-frequency chevron map for a CPB with $E_C = 270.8\,\text{MHz}$, $E_J = 22.5\,\text{GHz}$ and a pulse amplitude of $n_g^d(0) = \frac{1}{2\pi}7.5\,\text{MHz}$. Shown is the population of the $|1\rangle$ energy state, while the red line indicates the qubits frequency.

We can now see how the system reacts to a given drive by scanning through both the frequency ω_d and the drive amplitude V_0. The signal arriving in the hamiltonian from Equation (4.36) is then proportional to the voltage

$$n_g^d(t) = kV(t). \tag{4.57}$$

For simplification we turn off the noise for a moment to calibrate our model optimally. For $\Phi = 0$ the drive moves the qubits state in X-direction. We can choose now a drive strength of A and vary the evolution time and the drive's frequency. Starting in the energy ground state, we evolve the system according to trotterization of the time-dependent Schrödinger equation. The result is a so called time-chevron map, which can be seen in Figure 4.4. For optimization purpose, we also fix the evolution time to a $\tau = 20\,\text{ns}$ and scan through amplitude and frequency again. The result can be seen in Figure 4.5.

4.6.1. Pulse shaping

Gaussian pulses

Driving with a steady cosine is a rather unrealistic model. Physically, it is more convenient to define a pulse shape or envelop. Often we choose Gaussian profiles,

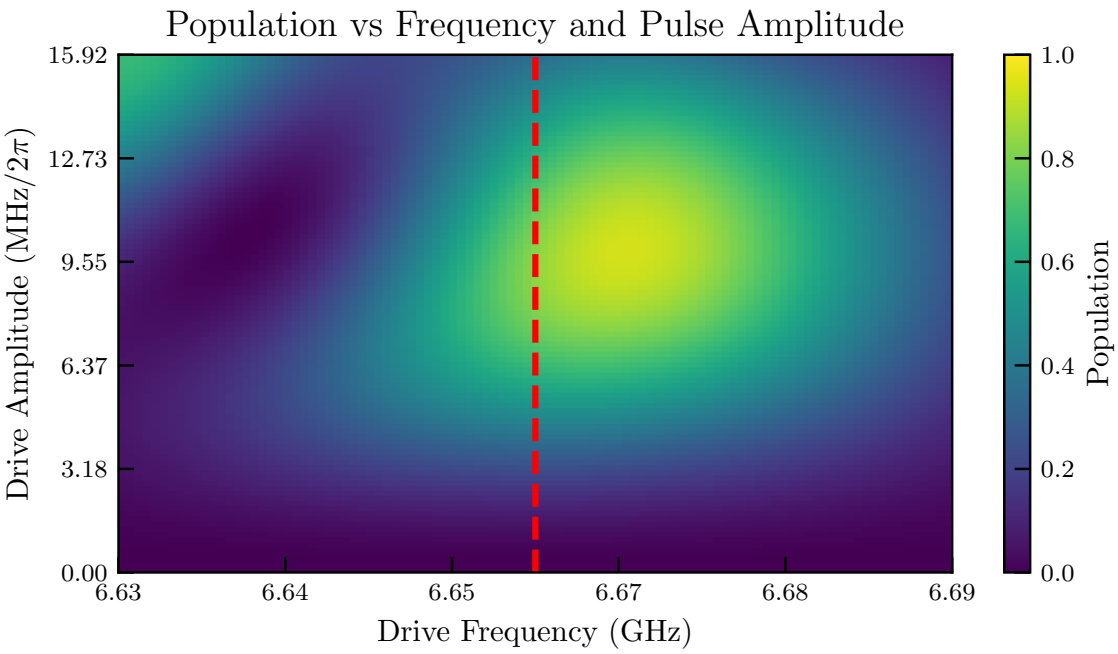

Figure 4.5.: Amplitude-frequency chevron map for $E_C = 270.8\,\text{MHz}$, $E_J = 22.5\,\text{GHz}$, $n_g = 0$ and an evolution time of $T = 20\,\text{ns}$. Shown is the population in the $|1\rangle$ energy state. The red line indicates the qubit frequency.

which have the advantage that they are well described in both frequency and time domain. Ideally, the Gauss function describing the envelope enures that the amplitude vanishes at both the beginning and the end, and thus takes the form [MW13]:

$$\Omega(t) = A\left(\exp\left[-\frac{(t-T/2)^2}{2\sigma^2}\right] - \exp\left[-\frac{(T/2)^2}{2\sigma^2}\right]\right)^m \tag{4.58}$$

where σ is the standard deviation and m ensures that $m-1$ derivatives are also starting and ending at zero amplitude. A is a normalization constant, which ensures that the desired amount of rotation is implemented by the pulse. Both A and σ can in an optimization setup be understood as free parameters.

4.6.2. Pulse optimization

We can now emulate the time evolution and adjust the drive parameters to gather the possibility of achieving high fidelity operations on the subspace of the two lowest energy levels. To avoid leakage into higher levels, we use the well cited DRAG scheme [Mot+09]. For the optimization of the parameters, we start with a Gaussian pulse envelope ($m = 1$) plus its DRAG correction, that is,

$$n_g^d(t) = \Omega(t)\cos(\omega_d t) - \frac{\dot{\Omega}(t)}{\Delta}\sin(\omega_d t) \tag{4.59}$$

Gate name	Fidelity
$RX90_{01}$	99.89 %
$RY90_{01}$	99.89 %
X_{01}	99.90 %
Y_{01}	99.90 %
$RX90_{12}$	99.33 %
$RY90_{12}$	99.97 %

Table 4.1.: Fidelities of the optimized gates.

and use a combination of a non-gradient based optimization (CMA-ES) for a broad search and a gradient based algorithm (LBFGS-B) for fine-tuning on the parameter set $\{A, \sigma, \omega_d, \Delta\}$ to implement basic single qubit gates, i.e. X90, Y90, X and Y. The fidelity which is used in this case is the gate fidelity on the lowest three level energy subspaces. That is

$$F = \frac{1}{3^2}\left|\mathrm{Tr}\left\{U^\dagger U^j_{\mathrm{target}}\right\}\right|^2 \tag{4.60}$$

where

$$U^{01}_{\mathrm{target}} = \begin{pmatrix} \cos\frac{\Theta}{2} & -\mathrm{i}e^{-\mathrm{i}\phi}\sin\frac{\Theta}{2} & 0 \\ -\mathrm{i}e^{\mathrm{i}\phi}\sin\frac{\Theta}{2} & \cos\frac{\Theta}{2} & 0 \\ 0 & 0 & 1 \end{pmatrix} \tag{4.61}$$

and

$$U^{12}_{\mathrm{target}} = \begin{pmatrix} 1 & 0 & 0 \\ 0 & \cos\frac{\Theta}{2} & -\mathrm{i}e^{-\mathrm{i}\phi}\sin\frac{\Theta}{2} \\ 0 & -\mathrm{i}e^{\mathrm{i}\phi}\sin\frac{\Theta}{2} & \cos\frac{\Theta}{2} \end{pmatrix}. \tag{4.62}$$

Z-gates can be implemented by either combining X and Y rotations, by letting the qubit evolve in time or virtually (details can be found here [McK+17]). The resulting dynamics are shown in Figure 4.6. For later purposes, we repeat the pulse optimizations also for the 90 degree rotations on the 12-transition. The reason for this is that higher levels have a larger parity splitting and therefore allow for a quicker separation between the parity states. The fidelities of the optimized gates are summarized in Table 4.1.

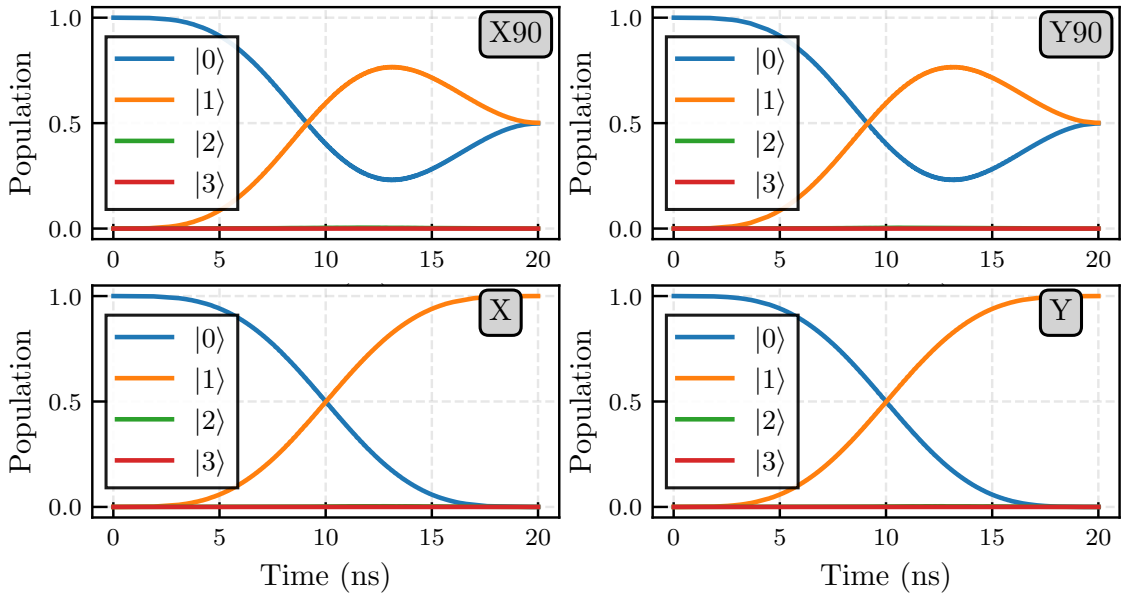

Figure 4.6.: Dynamics of the noise-free CPB after parameter optimization. Shown are the populations of the four lowest energy eigenstates, i.e. of $|0\rangle, |1\rangle, |2\rangle, |3\rangle$. We reach very high fidelities, which are summarized in Table 4.1.

4.7. Matching theory and experiment

Since the goal is to simulate the experiment and predict future outcomes, it is necessary to bring the experimental data and the simulation together. This will be done by comparing the results from the experiment directly with simulated data.

4.7.1. T_1 Decay

The first thing to match is the decay time T_1 which indicates how much of the population will decay into lower states. This happens because quantum systems tend to lower energy states in order to minimize their energy. In Figure 4.7 we show that a value of $T_1 = 17.39\,\mu s$ achieves great accordance to the experimental data.

4.7.2. T_2 and T_2^{Echo}

What was done in the experiment to gain information about the dephasing rate is that they did a Ramsey experiment, i.e. a pulse sequence consisting of a $X90$-pulse a wait time and another $X90$-pulse. Resulting in a decay of the phase information during the wait period. However, to eliminate the parity influence, they also performed a Ramsey-Echo experiment. Where after half of the wait period a refocussing X-pulse is applied to remove not only parity difference but also slow frequency noise.

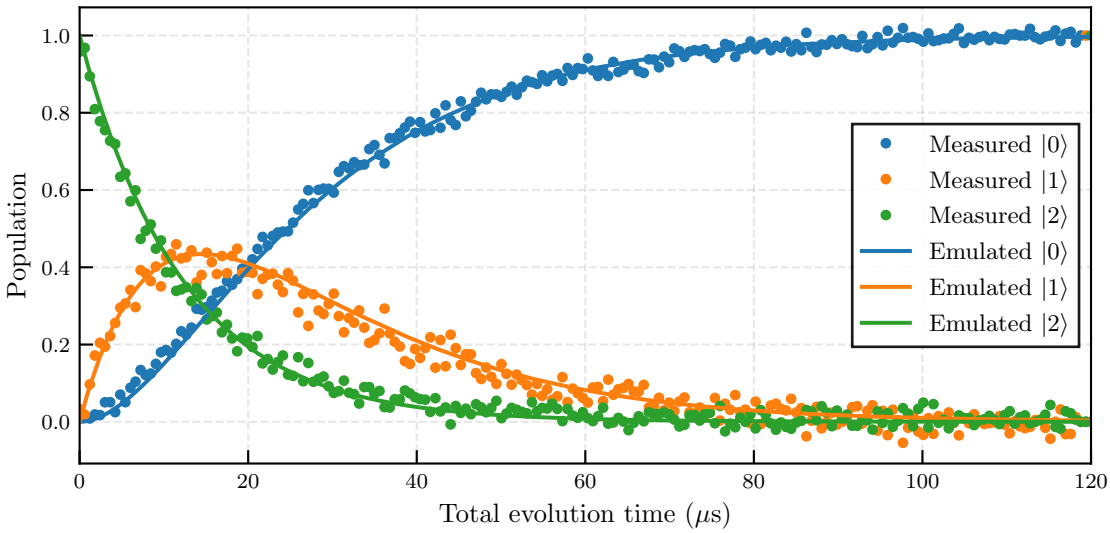

Figure 4.7.: Starting with a fully populated $|2\rangle$ state we let the system evolve under the influence of a T_1-Lindblad operator. The dotted points are obtained by the experiment, while the lines represent the results from the simulation. We see good agreement between theory and experiment.

In Figure 4.8 we check that the simulation works properly and show how experimental data can be interpreted, while in Figure 4.9 we show the results for the echoed variant.

4.8. Parity detection

Being able to detect the parity of the Cooper-Pair-Box systems is useful because it gives insight into quasi particle poisoning, which can strongly affect coherence and dynamics. By tracking the parity state of the system, one can better understand when and how non-equilibrium quasi particles enter or leave and how this impacts relaxation and dephasing. Also, there have been made attempts to detect Majorana Zero modes using similar techniques [Agh+25].

4.8.1. Ramsey-Strategy

The first possibility of detecting the parity state is performing a Ramsey like sequence. I.e. we prepare the qubit in the ground state (which should have roughly the same frequency). Afterward, we apply a $\pi_x/2$-Pulse to the qubit. In the Bloch sphere representation, this prepares the qubit at the equator of the Bloch sphere. Here we let the qubit oscillate for a time $\Delta t = \frac{1}{4\Delta_f}$. Where $\Delta_f = f^{01}_{even} - f^{01}_{odd}$ is the frequency difference between the first excitations of the even and the odd parity. This separates both parity states by an azimuth angle of $\frac{\pi}{2}$. To map the parity to the poles, we

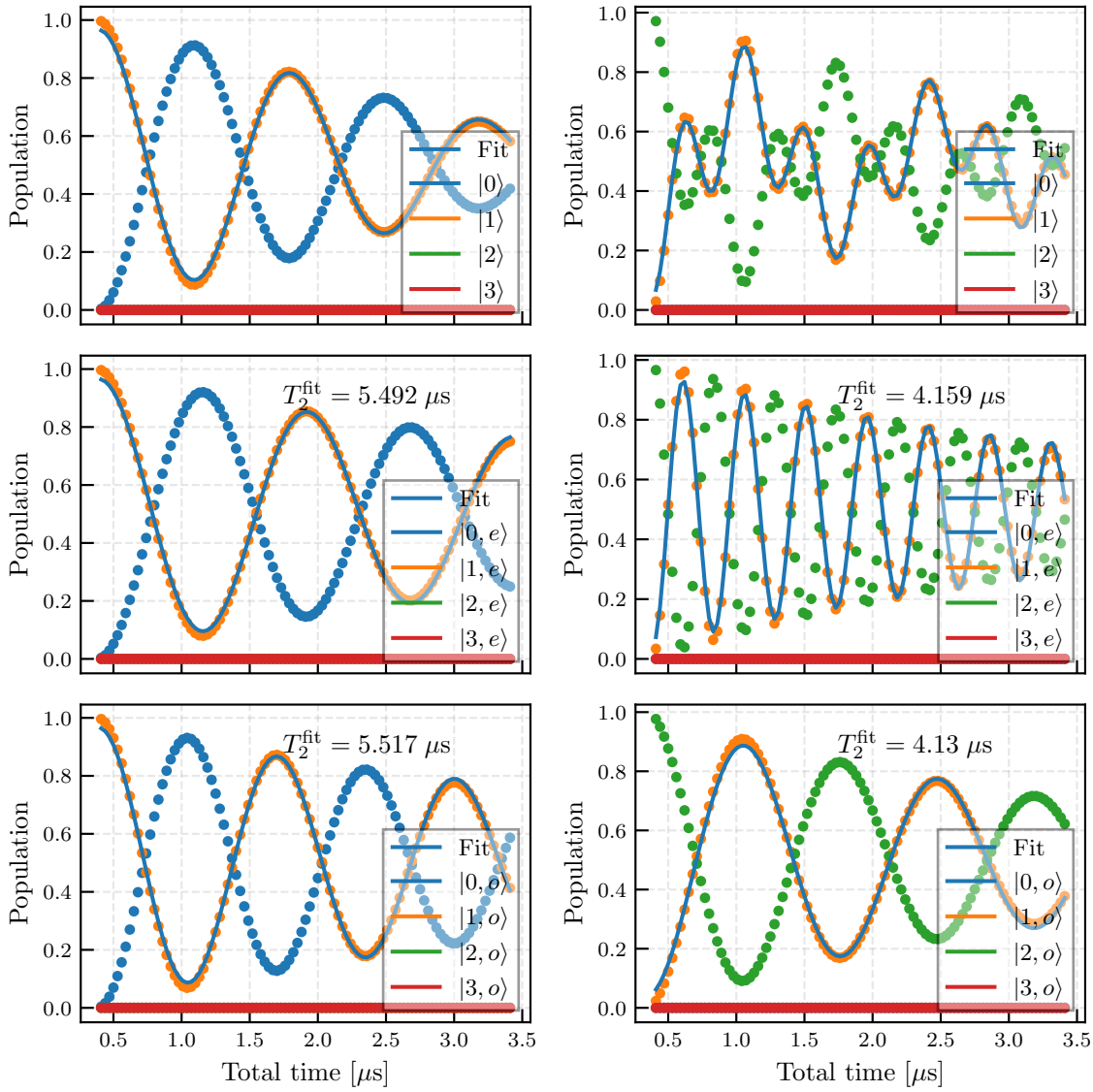

Figure 4.8.: Depicted is the resulting population for a Ramsey sequence on the 01 (12) transition vs their duration (right plot). The upper part is the oscillations for the combined dynamics, while the lower part shows the oscillations for even (middle) and odd (bottom) parity state.

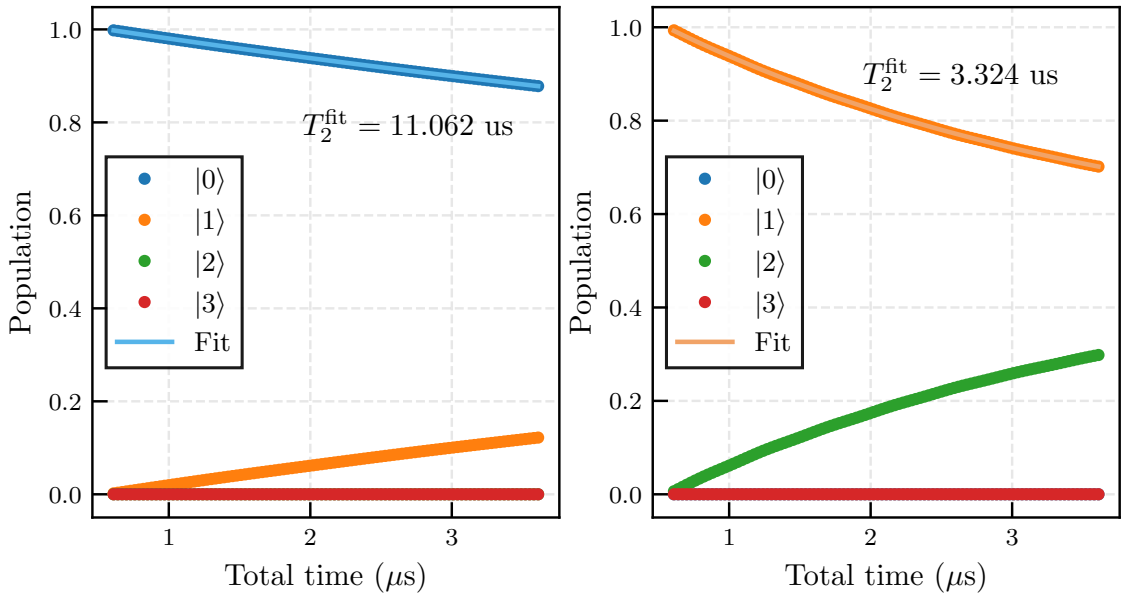

Figure 4.9.: Depicted is the emulated population for an echoed Ramsey sequence on the 01 (12) transition vs their duration (right plot).

apply a $\pi_y/2$-pulse such that when we read out the qubit the measurement result is '0' for the even and '1' for the odd parity. Given the optimized single-qubit gates (we optimized the single-qubit gates for the even parity case) we can directly implement this method. However, the problem with this method, is that we do not know if it is optimal in terms of separation speed and fidelity.

4.8.2. Rabi-Strategy

If we want to detect the parity of a state, it might be not the optimal strategy to wait till the two parity states separate in the equatorial plane of the Blochsphere. This is because leaving the system untouched can make it more susceptible to certain error sources. Instead, we propose to drive the system continuously to take advantage of decoupling effects due to continuous drive. Therefore, we try to do an X-gate for the even parity and an identity gate for the odd parity. The procedure to do so is to first prepare the system in a state that has a reasonable parity splitting, i.e. T_1 should not exceed one over the splitting frequency. The correct choice of the initial state should be calculated in advance by looking at how the parity splitting grows with the increase of the chosen sublevel system, while at the same time T_1 decreases with it. If we found a suitable configuration of the system, we drive the qubit at the frequency of transition we want to drive (in this case, the i-th transition of the even parity qubit), such that the other level is detuned by the splitting. Without additional parameters, the optimal time to separate both parities should be roughly one over the splitting frequency. In our example, this results in a total pulse duration

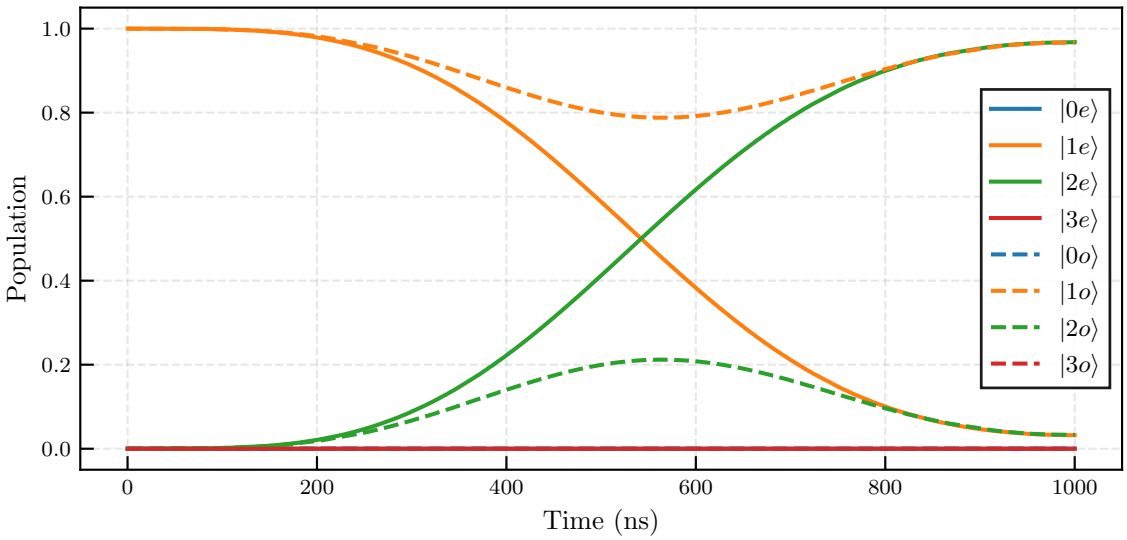

Figure 4.10.: Time evolution of the even (e) and odd (o) parity state during a continuous application of a DRAG corrected drive. We see that we can separate the two parities without using a Ramsey experiment.

of $t_{tot} = \frac{1}{\Delta} \approx 1\,\mu s$. However, with the use of DRAG this time can be reduced, while maintaining a reasonable fidelity. With the use of first order DRAG correction, we were able to increase the (noise free) parity detection fidelity to 99.6% within our simulation. Figure 4.10 shows the idea of this strategy.

4.9. Comparison of the two strategies

In Figure 4.11 we compare two strategies for parity detection. These are a Ramsey-type free evolution and a driven Rabi protocol. The objective is to infer the parity of the state with high fidelity while minimizing the total evolution time. The comparison shows that the Rabi-strategy is in general preferable, as it reaches a higher maximum fidelity for correctly identifying the parity state. Furthermore, it is able to identify the parity relatively independent of the total evolution time, while the fidelity for Ramsey strategy is oscillating because it is relying on the accumulation of a relative phase during the free evolution time. However, for very short evolution times the Ramsey strategy performs better since the system has not yet done the full Rabi oscillation, whereas a short free evolution in the equatorial plane of the Blochsphere is already providing a measurable separation of the parity states.

4.10. Conclusion

In this chapter we have developed a comprehensive framework for understanding, modeling, and controlling superconducting nanowire qubits, with a particular focus

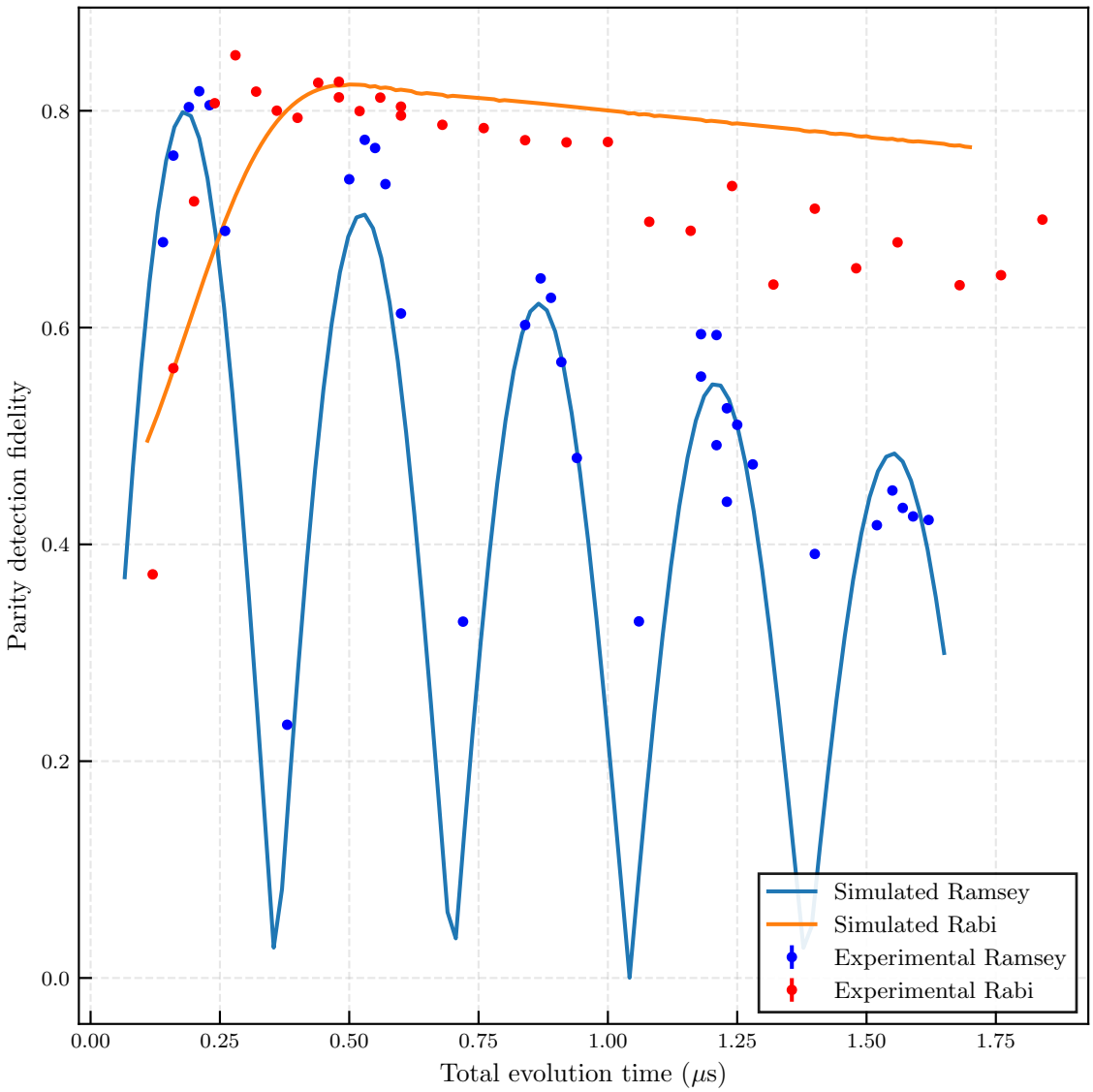

Figure 4.11.: Parity detection fidelity of a Ramsey and a Rabi experiment, dotted points are experimental data and solid lines are from the simulation. While the model is not perfectly reproducing the experimental data, we can still get some qualitative insight: We can reproduce the overall structure of the Ramsey oscillations and see that the Rabi strategy can perform better than the used Ramsey strategy.

on the Cooper-Pair-Box regime. Starting from basic circuit quantization, we derived effective Hamiltonians for various superconducting qubit designs and established both analytic and numerical methods to obtain their energy spectra and main noise sources. Further, we showed that our theoretical model is consistent with experimental measurements. We focused on noise and decoherence by integrating charge and parity noise into our simulations, enabling us to match our theoretical model to the experimentally obtained data. Here, parity noise, i.e. the tunneling events of quasi-particles, changes the charge configuration and influences the coherence. Overall, the combination of stochastic noise modeling and Lindblad dynamics proved to be crucial for capturing both non-Markovian effects and experimental decay constants such as T_1 and T_2. In a physical context, this demonstrates that in a real world experiment, both fast relaxation noise processes appear simultaneously with slow fluctuations in the system parameters.

We additionally demonstrated that parametrized pulse shaping and optimization enable high-fidelity control of the low energy subspace. This was possible even in the presence of leakage channels, Lindblad decay and stochastic dephasing noise. Especially useful were Gaussian envelopes with DRAG corrections: they were shown to implement elementary single-qubit operations with fidelities of 99.8%, obedient with experimentally reported values. Physically, this works so well because DRAG effectively suppresses the leakage into higher levels induced by the relatively small anharmonicity present in the system.

Together with fitting theoretical simulations to experimental data, these results show that the CPB-based model with two Josephson energy terms is a valid description of nanowire parity-sensitive qubits. This is consistent with previous works. However, the model is still limited to the low-energy subspace and depends on precise noise description. Apart from that, we implemented a novel technique which measures the parity state of the system by applying optimized Rabi-pulses and compared it to the existing Ramsey method.

Summarizing, this chapter reduces the discrepancy between theoretical modeling and experimental characterization and shows the opportunity of optimized pulse control for measuring the parity state. Future work could try to use dCRAB type algorithms to improve the parity detection schemes even further.

5. Conclusion

We started our journey by introducing quantum optimal control theory and related topics. The focus was on understanding noise processes and how to lower their impact in small quantum systems. During the work this goal spread into many related topics. Some of them were specific to the respective system and others seemed to be valid in a more general context. What connected all the ideas was the concept of reliable modelling and control of quantum systems.

The first non-introductory part investigated coherent and phase-accurate control of a system consistent of strongly coupled nuclear spin in a Germanium vacancy center. Here we used theoretical insights such as the Weyl chamber, controllability arguments and optimization techniques to both understand and improve experimental results. The techniques helped us to develop a deeper understanding of the control in group IV vacancy systems. We showed that optimized control pulses on the electron transitions are enough to fully control the two spin system. Furthermore, we demonstrated that high precision one- and two-qubit gates can be implemented in strongly coupled systems and this despite strong dephasing noise present on the electron spin. Future work can concentrate on using more native gates in the vacancy centers, including also system parameters such as the Larmor frequency in the optimization process and using the results for implementing small repeater protocols.

In the second part, we showed that the concrete structure of colored noise is not necessary for designing robust control pulses. We learned that the regime between very fast and very slow noise is not special in the sense that the techniques to circumvent this type of noise do not differ significantly from that for slow noise. Additionally, we found that it is very challenging to use optimal control for separating different (non-Gaussian) noise models, since higher order effects are already partially decoupled if a drive is applied. The best method here is probably to investigate the noise in an undriven experiment with very short decoupling pulses in between.

In the last part, we demonstrated that Rabi inspired parity detection schemes might outperform Ramsey type schemes. We learned that it is necessary for a reliable model to include second order Josephson excitations and to use higher levels for parity detection, since the frequency splitting of the parity is larger there. Future work could for example investigate if a higher number of parameters in the optimization of the control can find even better solutions for parity detection. Apart from the scientific results, I learned that cooperation between theory and experiment is often at the heart of progress. Overall, I hope this thesis helps the field to gain a better under-

standing of how to make quantum control and the controlled devices more reliable and stable.

A. Appendix

A.1. Lie-closure proof

To verify controllability, we explicitly compute the Lie closure of the operator set (a summary of why this is enough can be found in [dAl21])

$$S = \{H_0, X_0 = \sigma_x \otimes \mathbb{1}\}. \tag{A.1}$$

The first 9 independent operators are

$$\{H_0, H_1 = [H_0, X_0], H_2 = [H_1, X_0], \cdots, H_9 = [H_8, X_0]\}. \tag{A.2}$$

Then we do not find new independent elements and we continue by extending the list with

$$\{H_{10} = [H_1, H_2], H_{11} = [H_1, H_3], \cdots, H_{14} = [H_1, H_6]\} \tag{A.3}$$

and the last element is

$$\{H_{15} = [H_{10}, H_{11}]\}. \tag{A.4}$$

Meaning that successive commutators generate all tensor products of Pauli operators, and therefore span the full Lie algebra $\mathfrak{su}(4)$. This shows that the system remains fully controllable even without a direct drive on the nuclear spin.

A.2. Pseudo code for generating noise traces

Ornstein-Uhlenbeck process

This is pseudocode generating static OU-noise with a given time grid times, noise amplitude σ and rate κ.

```
N ← number of time steps
dt ← size of time step
std ← σ/√(2κ)
X[0] ← sample from ~𝒩(0, std)
W ← sample N-1 times from ~𝒩(0,1)
dstd ← std * (1 − exp{−2κdt})
For k in {1,...,N-1}:
    X[k+1] ← exp{−κ * dt}X[k] + dstdW[k]
return X
```

TLS-noise

This is pseudocode generating static OU-noise with a given time grid times, flipping rate λ and coupling strenght g.

```
N = number of time stpes
fliptime = 1/λ
currentstate = sample from {-1,1}
next_flip_time =
    sample from exponential_distribution(t_flip)
flip_index = [next_flip_time / dt ]
for k in {0,1,...,N-1}:
    if k >= flip_index:
        current_state *= -1
        next_flip_time =
            sample from exponential_distribution(t_flip)
        flip_index = i+ [next_flip_time / dt]
    X[i] = current_state
return g*X
```

Inverse-Fourier-Transform method

This is pseudocode for generating time valued noise traces, by Fourier transforming the spectral density with random phases.

```
### spec[:,0] frequency of spectrum
### spec[:,1] spectral density values
fmax = max(spec[:,0])
fmin = min(spec[:,0])
fvals = linspace(fmin, fmax, steps)
density = interpolate(fvals, spec[:, 0], spec[:, 1])
phase = 2 * pi * uniform(0, 1, steps)
times = arange(0, steps  * dt, dt)
noise_vals = fft(irfft(sqrt(2)*dens*exp(1j * phase))
return fvals, times, noise_vals
```

B. Stochastic Hamiltonians and Lindblad like equations

B.1. Motivation

In quantum computation, accurate characterizing and calibrating qubits needs excellent models, which predict where performance resources lie and how quantum systems evolve in time. In the younger past, a zoo of methods to simulate the dynamics of quantum systems was developed. It is very difficult to say under which conditions which simulation method works best, and there has been a lot of effort been put on testing and comparing different simulation methods [WKO21]. The goal of this chapter is to compare some of the latest and most promising methods of the recent past and use the insight on the individual methods to translate between them and find conditions which tell us which method should be used. Furthermore, another goal is to develop methods to include also non-Gaussian environmental dynamics. We start by looking at the most simple example we can think of, which is a system consistent of a single qubit under pure dephasing noise.

B.2. Pure Dephasing

In the case of semi-classical dephasing for one qubit the Hamiltonian of the qubit in the rotating frame can be expressed as

$$H(t) = \beta(t)\sigma_z. \tag{B.1}$$

Any state $\rho(t)$ will evolve under the action of the von-Neumann equation $\dot{\rho} = -\mathrm{i}[H, \rho]$ which is formally solved by

$$\rho(t) = U\rho_0 U^\dagger \tag{B.2}$$

where

$$U = \exp\left\{-\mathrm{i}\int_0^t \beta(s)dsZ\right\} \tag{B.3}$$

$$= \exp\left\{-\mathrm{i}\Phi(t)Z\right\}. \tag{B.4}$$

If we look at the evolution averaged over multiple noise realizations $\beta_k(t)$ we see that for a general initial density matrix

$$\rho_0 = \frac{1}{2}(\mathbb{1} + xX + yY + zZ) \tag{B.5}$$

the dynamics are given as

$$\rho(t) = \exp\{-i\Phi(t)Z\}\rho_0 \exp\{i\Phi(t)Z\} \tag{B.6}$$

$$= \frac{1}{2}[\mathbb{1} + (x\cos(2\Phi(t)) - y\sin(2\Phi(t)))X + (y\cos(2\Phi(t)) + x\sin(2\Phi(t)))Y + zZ]. \tag{B.7}$$

or written in the Pauli basis in vector form

$$\|\rho_t\rangle = \begin{pmatrix} 1 \\ x_t \\ y_t \\ z_t \end{pmatrix}, \tag{B.8}$$

where $x_t = \mathrm{Tr}\{\rho_t X\}, y_t = \mathrm{Tr}\{\rho_t Y\}, z = \mathrm{Tr}\{\rho_t Z\}$ and averaged over multiple noise realizations this takes the form

$$\|\rho(t)\rangle = \begin{pmatrix} 1 & 0 & 0 & 0 \\ 0 & \langle\cos(2\Phi(t))\rangle & -\langle\sin(2\Phi(t))\rangle & 0 \\ 0 & \langle\sin(2\Phi(t))\rangle & \langle\cos(2\Phi(t))\rangle & 0 \\ 0 & 0 & 0 & 1 \end{pmatrix} \|\rho_0\rangle. \tag{B.9}$$

If we look at the characteristic function of the random variable Φ we notice that

$$\begin{aligned} \varphi_{\Phi(\tau)}(z=2) &= \langle\exp\{i2\Phi(t)\}\rangle \\ &= \langle\cos(2\Phi(t))\rangle + i\langle\sin(2\Phi(t))\rangle \\ &= \chi(t) + i\upsilon(t), \end{aligned} \tag{B.10}$$

where we introduced $\chi(t) = \mathrm{Re}\{\varphi_{\Phi(t)}(z=2)\}$, $\upsilon(t) = \mathrm{Im}\{\varphi_{\Phi(t)}(z=2)\}$. Thus, we get

$$\|\rho(\tau)\rangle = \begin{pmatrix} 1 & 0 & 0 & 0 \\ 0 & \chi(t) & -\upsilon(t) & 0 \\ 0 & \upsilon(t) & \chi(t) & 0 \\ 0 & 0 & 0 & 1 \end{pmatrix} \|\rho_0\rangle. \tag{B.11}$$

Which means that if we know the characteristic function of our noise process (at $z = 2$) we can exactly describe the dynamics of our system. We now make the assumption that our noise field has zero mean ($\langle\beta(t)\rangle = 0$)). This implies that in the case of

Gaussian noise all odd cumulants vanish and Equation (B.11) simplifies to

$$\|\rho(\tau)\rangle = \begin{pmatrix} 1 & 0 & 0 & 0 \\ 0 & \chi(t) & 0 & 0 \\ 0 & 0 & \chi(t) & 0 \\ 0 & 0 & 0 & 1 \end{pmatrix} \|\rho_0\rangle. \tag{B.12}$$

B.3. Driven dephasing dynamics

We consider the Hamiltonian

$$H(t) = \frac{\Omega(t)}{2} X + \beta(t) Z, \tag{B.13}$$

where $\Omega(t)$ is a deterministic control function and $\beta(t)$ is a stochastic field with zero mean. Because $[H(t), H(t')] \neq 0$ in general, the time evolution is nontrivial, and one cannot simply exponentiate a time-integral of $H(t)$. For readability, time dependencies are for the following section indicated with subscripts (f.e. $H_t = H(t)$). A standard trick is to move to a frame which is rotating with the drive $R = \exp\left(\mathrm{i}\frac{\Theta_t}{2} X\right)$ where $\Theta_t = \int_0^t \Omega_{t'} dt'$. The Hamiltonian in the new frame is then given through

$$\begin{aligned} \tilde{H}_t &= \mathrm{i}\dot{R}_t R_t^\dagger + R_t H_t R_t^\dagger && \text{(B.14)} \\ &= -\Omega_t X + \exp\left\{\mathrm{i}\frac{\Theta_t}{2} X\right\} (\Omega_t X + \beta_t Z) \exp\left\{-\mathrm{i}\frac{\Theta_t}{2} X\right\} && \text{(B.15)} \\ &= \cos(\Theta_t)\beta_t Z + \sin(\Theta_t)\beta_t Y && \text{(B.16)} \\ &= \beta_{zt} Z + \beta_{yt} Y. && \text{(B.17)} \end{aligned}$$

Thus, the pure Z-dephasing noise in the original frame is rotated into a mixture of Z and Y in the new frame, with time-dependent weights. We are interested in the ensemble-averaged dynamics, but first consider the unitary propagator in this frame, obeying

$$\dot{V} = -\mathrm{i}\tilde{H} V. \tag{B.18}$$

Differentiating again,

$$\Rightarrow \ddot{V} = -\mathrm{i}\left(\dot{\tilde{H}} V + \tilde{H}\dot{V}\right). \tag{B.19}$$

One finds (after some algebra)

$$\dot{\tilde{H}} = \left(\frac{\dot{\beta}_t}{\beta_t}\mathbb{1} + 2\mathrm{i}\Omega_t X\right)\tilde{H} \tag{B.20}$$

and hence

$$\ddot{V} = -\mathrm{i}\Big(\dot{\tilde{H}}V + \tilde{H}\dot{V}\Big) \tag{B.21}$$

$$= \left(2\mathrm{i}\Omega X + \frac{\dot{\beta}_t}{\beta_t}\mathbb{1}\right)\underbrace{\big(-\mathrm{i}\tilde{H}V\big)}_{=\dot{V}} + (-\mathrm{i})^2\tilde{H}\tilde{H}V \tag{B.22}$$

$$= \left(2\mathrm{i}\Omega_t X + \frac{\dot{\beta}_t}{\beta_t}\mathbb{1}\right)\dot{V} - \beta_t^2 V. \tag{B.23}$$

This differential equation should remind the reader to that of a damped harmonic oscillator, which is

$$\ddot{x} + 2\gamma\dot{x} + \omega_0^2 x = 0, \tag{B.24}$$

where 2γ plays the role of the damping coefficient and ω_0^2 the driving force frequency. We see that the noise derivative together with the drive play the role of the damping, while the noise square determines the frequency induced by the external noise force. However, there are two crucial sources which add more difficulty. First V is an operator, which implies that multiplying the damping-like term $2\mathrm{i}\Omega_t X + \frac{\dot{\beta}_t}{\beta_t}\mathbb{1}$ is a non-commuting operation and second this term is explicitly time-dependent and does not commute at different times, so one cannot simply integrate or diagonalize it. This makes obtaining closed-form solutions extremely challenging. Because of these complications, general analytic solutions are rare. In fact, for certain classes of driven two-level problems (single axis-driving) analytic solutions were found [BD12]. However, in the general case we need to use methods to get approximate solutions such as Magnus Expansion for dissipative systems which was done here [BE20], master equations for non-Markovian noise [Gro+23] and Laplace transform approximations [WZ21].

We now aim to derive a Lindblad-type equation in the rotating frame, beginning with the von Neumann equation

$$\dot{\rho}_t = -\mathrm{i}[H_t, \rho_t]. \tag{B.25}$$

$$\tag{B.26}$$

Integrating this leads to

$$\rho_t = \rho_0 - \mathrm{i}\int_0^t ds[H_s, \rho_s] \tag{B.27}$$

and reinserting the last result in the von-Neumann equation yields

$$\dot{\rho}_t = -\mathrm{i}[H_t, \rho_0] - \int_0^t ds[H_t, [H_s, \rho_s]] \tag{B.28}$$

$$= -\mathrm{i}[H_t, \rho_0] - \int_0^t ds[\beta_{zt}Z + \beta_{yt}Y, [\beta_{zs}Z + \beta_{ys}Y, \rho_s]] \tag{B.29}$$

$$\begin{aligned} = -\mathrm{i}[H_t, \rho_0] - \int_0^t ds\Big(&\beta_{zt}\beta_{zs}[ZZ\rho_s - Z\rho_s Z - Z\rho_s Z + \rho_s ZZ] \\ &+ \beta_{zt}\beta_{ys}[ZY\rho_s - Z\rho_s Y - Y\rho_s Z + \rho_s YZ] \\ &+ \beta_{yt}\beta_{zs}[YZ\rho_s - Y\rho_s Z - Z\rho_s Y + \rho_s ZY] \\ &+ \beta_{yt}\beta_{ys}[YY\rho_s - Y\rho_s Y - Y\rho_s Y + \rho_s YY]\Big) \end{aligned} \tag{B.30}$$

$$\begin{aligned} = -\mathrm{i}[\beta_{zt}Z + \beta_{yt}Y, \rho_0] + \int_0^t ds\Big(&\beta_{zt}\beta_{zs}D_{ZZ}[\rho_s] + \beta_{zt}\beta_{ys}D_{ZY}[\rho_s] \\ &+ \beta_{yt}\beta_{zs}D_{YZ}[\rho_s] + \beta_{yt}\beta_{ys}D_{YY}[\rho_s]\Big), \end{aligned} \tag{B.31}$$

where we introduced the Pauli Lindblad operators

$$D_{\sigma_i\sigma_j}[\rho] = [\sigma_i, [\sigma_j, \rho]]. \tag{B.32}$$

Averaging over multiple noise realization β we are left with

$$\dot{\rho}_t = -\int_0^t ds\Big(\langle\beta_{zt}\beta_{ys}D_{ZY}[\rho_s]\rangle + \langle\beta_{yt}\beta_{zs}D_{YZ}[\rho_s]\rangle\, Z + \langle\beta_{zt}\beta_{zs}D_{ZZ}[\rho_s]\rangle + \langle\beta_{yt}\beta_{ys}D_{YY}[\rho_s]\rangle \Big). \tag{B.33}$$

This means we do not only have to deal with orthogonal noise but also with cross correlations.

So far we made no approximations. Normally, what is done now is to assume that the correlation between the noise and the density matrix is not strong, i.e., that for any linear operator $\mathcal{B}$ we have

$$\langle\beta_t\beta_s\mathcal{B}[\rho_s]\rangle \approx \langle\beta_t\beta_s\rangle\,\mathcal{B}[\rho_s] \tag{B.34}$$

$$:= C(t,s)\mathcal{B}[\rho_s]. \tag{B.35}$$

After this approximation is done we cannot distinguish anymore between Gaussian random processes and Non-Gaussian processes. It leads in the Pauli basis to the following integral-differential equation

$$\|\dot{\rho}_t\rangle \approx -4\int_0^t dsC(t,s)A(t,s)\|\rho_s\rangle, \tag{B.36}$$

where we introduced the matrix

$$A(t,s) = \begin{pmatrix} 1 & 0 & 0 & 0 \\ 0 & \cos(2(\Theta_s - \Theta_t)) & 0 & 0 \\ 0 & 0 & \cos(2\Theta_s)\cos(2\Theta_t) & -\cos(2\Theta_s)\sin(2\Theta_t) \\ 0 & 0 & -\cos(2\Theta_s)\sin(2\Theta_t) & \sin(2\Theta_s)\sin(2\Theta_t) \end{pmatrix}. \quad \text{(B.37)}$$

The elements of the matrix can be computed by looking at the action on a density matrix in the Pauli basis

$$\rho = \frac{1}{2}(\mathbb{1} + xX + yY + zZ) \quad \text{(B.38)}$$

which is given as

$$\rho'_O = \mathrm{Tr}([H_t, [H_s, \rho_s]]O) \quad \text{for} \quad O \in \{X, Y, Z\}. \quad \text{(B.39)}$$

B.4. Magnus-Cumulant-Expansion (MCE)

The von Neumann equation in the vectorized form is

$$\dot{\rho}(t) = \mathcal{L}(t)\rho(t), \quad \text{(B.40)}$$

where $\mathcal{L}$ is the Liouville operator. Since we want to solve it, a particular useful method is to write the solution as an exponential of a function $Q(t)$

$$\rho(t) = \exp\{Q(t)\}\rho_0. \quad \text{(B.41)}$$

Where we can expand Q in terms of $\mathcal{L}$ according to the Magnus expansion

$$Q(t) = \sum_{k=1}^{\infty} Q_k(t), \quad \text{(B.42)}$$

where the first few terms are given as

$$Q_1(t) = \int_0^t dt_1 \mathcal{L}(t_1) \quad \text{(B.43)}$$

$$Q_2(t) = \frac{1}{2}\int_0^t dt_1 \int_0^{t_1} dt_2 [\mathcal{L}(t_1), \mathcal{L}(t_2)] \quad \text{(B.44)}$$

$$Q_3(t) = \frac{1}{6}\int_0^t dt_1 \int_0^{t_1} dt_2 \int_0^{t_2} dt_3 ([\mathcal{L}(t_1), [\mathcal{L}(t_2), \mathcal{L}(t_3)]] + [\mathcal{L}(t_3), [\mathcal{L}(t_2), \mathcal{L}(t_1)]]) \quad \text{(B.45)}$$

$$Q_4(t) = \frac{1}{12}\int_0^t dt_1 \int_0^{t_1} dt_2 \int_0^{t_2} dt_3 \int_0^{t_3} dt_4 [[[\mathcal{L}_1, \mathcal{L}_2], \mathcal{L}_3], \mathcal{L}_4] \quad \text{(B.46)}$$

$$+ [\mathcal{L}_1, [[\mathcal{L}_2, \mathcal{L}_3], \mathcal{L}_4]] + [\mathcal{L}_1, [\mathcal{L}_2, [\mathcal{L}_3, \mathcal{L}_4]]] + [\mathcal{L}_2, [\mathcal{L}_3, [\mathcal{L}_4, \mathcal{L}_1]]]. \tag{B.47}$$

Now, we expand in terms of noise operators $\beta(t)$, i.e. in the control frame we can write

$$\mathcal{L}(t) = \beta(t) L(t). \tag{B.48}$$

We want a time evolution method which can distinguish Gaussian and Non-Gaussian noise, that also means we have to include (for centered noise) all orders up to β^4 (for space reasons we will put the time dependence from now on as an index or omit it completely):

$$\begin{aligned}
\rho_t &= \langle \exp\{Q_t\} \rangle \, \rho_0 && \text{(B.49)}\\
&\approx \left(\mathbb{1} + \langle Q_t \rangle + \frac{1}{2} \left\langle Q_t^2 \right\rangle + \frac{1}{6} \left\langle Q_t^3 \right\rangle + \frac{1}{24} \left\langle Q_t^4 \right\rangle \right) \rho_0 && \text{(B.50)}\\
&=: (\mathbb{1} + \Upsilon) \rho_0. && \text{(B.51)}
\end{aligned}$$

Then, we can calculate Υ as

$$\begin{aligned}
\Upsilon &\approx \langle Q_1 \rangle + \langle Q_2 \rangle + \langle Q_3 \rangle + \langle Q_4 \rangle && \text{(B.52)}\\
&+ \frac{1}{2} \left(\left\langle Q_1^2 \right\rangle + \left\langle Q_2^2 \right\rangle + \langle \{Q_1, Q_2\} \rangle + \langle \{Q_1, Q_3\} \rangle \right) && \text{(B.53)}\\
&+ \frac{1}{6} \left(\left\langle Q_1^3 \right\rangle + \left\langle Q_1^2 Q_2 \right\rangle + \langle Q_1 Q_2 Q_1 \rangle + \left\langle Q_2 Q_1^2 \right\rangle \right) && \text{(B.54)}\\
&+ \frac{1}{24} \left\langle Q_1^4 \right\rangle . && \text{(B.55)}
\end{aligned}$$

Now, we want to rewrite the solution again as an exponential. Therefore, we approximate and drop again terms with order $n > 4$:

$$\begin{aligned}
\mathcal{G}(t) = \ln(\mathbb{1} + \Upsilon) &\approx \Upsilon - \frac{\Upsilon^2}{2} + \frac{\Upsilon^3}{3} - \frac{\Upsilon^4}{4} && \text{(B.56)}\\
&= \langle Q_1 \rangle + \langle Q_2 \rangle + \langle Q_3 \rangle + \langle Q_4 \rangle && \text{(B.57)}\\
&+ \frac{1}{2} \left(\left\langle Q_1^2 \right\rangle + \left\langle Q_2^2 \right\rangle + \langle \{Q_1, Q_2\} \rangle + \langle \{Q_1, Q_3\} \rangle \right) && \text{(B.58)}\\
&+ \frac{1}{6} \left(\left\langle Q_1^3 \right\rangle + \left\langle Q_1^2 Q_2 \right\rangle + \langle Q_1 Q_2 Q_1 \rangle + \left\langle Q_2 Q_1^2 \right\rangle \right) && \text{(B.59)}\\
&+ \frac{1}{24} \left\langle Q_1^4 \right\rangle && \text{(B.60)}\\
&- \frac{1}{2} \left(\langle Q_1 \rangle^2 + \langle Q_2 \rangle^2 + \{ \langle Q_1 \rangle , \langle Q_2 \rangle \} + \{ \langle Q_1 \rangle , \langle Q_3 \rangle \} + \frac{1}{4} \left\langle Q_1^2 \right\rangle^2 \right) && \text{(B.61)}\\
&+ \frac{1}{3} \langle Q_1 \rangle^3 && \text{(B.62)}\\
&- \frac{1}{4} \langle Q_1 \rangle^4 , && \text{(B.63)}
\end{aligned}$$

such that

$$\rho(t) \approx \exp[\mathcal{G}(t)] \rho_0. \tag{B.64}$$

Note: the approximations are valid as long as $\int_0^t dt \|\mathcal{L}(t_1)\|_2 dt_1 < \pi$ (Convergence radius of the Magnus expansion) and $\|\Upsilon\| \leq 1$ (Convergence condition for the expansion of the logarithm).
In the case of centered noise, i.e. noise with zero mean, we are left with:

$$\mathcal{G}(t) \approx \langle Q_2 \rangle + \langle Q_3 \rangle + \langle Q_4 \rangle \tag{B.65}$$
$$+ \frac{1}{2}\Big(\big\langle Q_1^2 \big\rangle + \big\langle Q_2^2 \big\rangle + \langle \{Q_1, Q_2\} \rangle + \langle \{Q_1, Q_3\} \rangle\Big) \tag{B.66}$$
$$+ \frac{1}{6}\Big(\big\langle Q_1^3 \big\rangle + \big\langle Q_1^2 Q_2 \big\rangle + \langle Q_1 Q_2 Q_1 \rangle + \big\langle Q_2 Q_1^2 \big\rangle\Big) \tag{B.67}$$
$$+ \frac{1}{24}\big\langle Q_1^4 \big\rangle \tag{B.68}$$
$$- \frac{1}{2}\Big(\langle Q_2 \rangle^2 + \frac{1}{4}\big\langle Q_1^2 \big\rangle^2\Big). \tag{B.69}$$

B.5. Dyson-Cumulant-Expansion (DCE)

We can do the same with a Dyson-Series instead of a Magnus expansion, which is related to the previous chapter. We start again with

$$\dot{\rho}(t) = \mathcal{L}(t)\rho(t), \tag{B.70}$$

but now want to directly get

$$\rho(t) = \mathcal{U}(t)\rho_0. \tag{B.71}$$

Therefore we can expand $\mathcal{U}$ in a Dyson like series:

$$\mathcal{U} = \sum_{k=0}^{\infty} \mathcal{U}_k, \tag{B.72}$$

where the first terms are given as

$$\mathcal{U}_0 = \mathbb{1} \tag{B.73}$$
$$\mathcal{U}_1 = \int_0^t dt_1 \mathcal{L}(t_1) \tag{B.74}$$
$$\mathcal{U}_2 = \int_0^t dt_1 \int_0^{t_1} dt_2 \mathcal{L}(t_1)\mathcal{L}(t_2) \tag{B.75}$$
$$\mathcal{U}_3 = \int_0^t dt_1 \int_0^{t_1} dt_2 \int_0^{t_2} dt_3 \mathcal{L}(t_1)\mathcal{L}(t_2)\mathcal{L}(t_3) \tag{B.76}$$
$$\mathcal{U}_4 = \int_0^t dt_1 \int_0^{t_1} dt_2 \int_0^{t_2} dt_3 \int_0^{t_3} dt_4 \mathcal{L}(t_1)\mathcal{L}(t_2)\mathcal{L}(t_3)\mathcal{L}(t_4). \tag{B.77}$$

Taking the average results in

$$\rho(t) \approx (\mathbb{1} + \langle \mathcal{U}_1 \rangle + \langle \mathcal{U}_2 \rangle + \langle \mathcal{U}_3 \rangle + \langle \mathcal{U}_4 \rangle)\rho_0 \tag{B.78}$$
$$= (\mathbb{1} + \Upsilon)\rho_0. \tag{B.79}$$

And again we now try to express it as some exponential $\rho(t) \approx \exp(\mathcal{G}(t))\rho_0$

$$\mathcal{G}(t) \approx \Upsilon - \frac{\Upsilon^2}{2} + \frac{\Upsilon^3}{3} - \frac{\Upsilon^4}{4} \tag{B.80}$$
$$= \langle \mathcal{U}_1 \rangle + \langle \mathcal{U}_2 \rangle + \langle \mathcal{U}_3 \rangle + \langle \mathcal{U}_4 \rangle \tag{B.81}$$
$$- \frac{1}{2}\big(\langle \mathcal{U}_1 \rangle^2 + \langle \mathcal{U}_2 \rangle^2 + \langle \mathcal{U}_1 \rangle \langle \mathcal{U}_2 \rangle + \langle \mathcal{U}_1 \rangle \langle \mathcal{U}_3 \rangle \big) \tag{B.82}$$
$$+ \frac{1}{3} \langle \mathcal{U}_1 \rangle^3 - \frac{1}{4} \langle \mathcal{U}_1 \rangle^4 \tag{B.83}$$

in the case of centered noise ($\langle \mathcal{U}_1 \rangle = 0$) this simplifies to

$$\mathcal{G}(t) \approx \langle \mathcal{U}_2 \rangle + \langle \mathcal{U}_4 \rangle - \frac{1}{2} \langle \mathcal{U}_2 \rangle^2 \tag{B.84}$$

Which involves considerably fewer terms than the Magnus-Cumulant-Expansion.

B.6. Expansions for the time derivative

Unfortunately, these methods are numerically difficult to implement because we have to evaluate 4-fold integrals over matrix product functions, and we were not able to test them easily, yet. This is why it might be easier to make some expansions for the time derivative of ρ_t.

B.6.1. Dyson

We start again with

$$\dot{\rho}(t) = \mathcal{L}(t)\rho(t) \tag{B.85}$$
$$\approx \mathcal{L}(t)(\mathbb{1} + \mathcal{U}_1 + \mathcal{U}_2 + \mathcal{U}_3)\rho_0 \tag{B.86}$$

in the case of centered, Gaussian noise this simplifies to

$$\dot{\rho}(t) = \int_0^t \mathcal{L}(t)\mathcal{L}(t_1)\rho_0 + \int_0^t dt_1 \int_0^{t_1} dt_2 \int_0^{t_2} dt_3 \mathcal{L}(t)\mathcal{L}(t_1)\mathcal{L}(t_2)\mathcal{L}(t_3)\rho_0 \tag{B.87}$$

B.6.2. Magnus

Here we start with

$$\dot{\rho}(t) = \mathcal{L}(t)\rho(t) \tag{B.88}$$
$$= \mathcal{L}(t)\exp\{Q_t\}\rho_0 \tag{B.89}$$
$$\approx \mathcal{L}(t)(\mathbb{1} + Q_t + \frac{1}{2}Q_t^2 + \frac{1}{6}Q_t^3)\rho_0 \tag{B.90}$$
$$\approx \left(\langle\mathcal{L}(t)\rangle + \langle\mathcal{L}(t)(Q_1+Q_2+Q_3)\rangle + \frac{1}{2}\left\langle\mathcal{L}(t)(Q_1^2+Q_1Q_2+Q_2Q_1)\right\rangle + \frac{1}{6}\left\langle\mathcal{L}(t)Q_1^3\right\rangle\right)\rho_0 \tag{B.91}$$

in the case of zero mean and Gaussian noise this evaluates to

$$\dot{\rho}(t) \approx \left\langle\mathcal{L}(t)\left(Q_1+Q_3+\frac{1}{2}(Q_1Q_2+Q_2Q_1)+\frac{1}{6}Q_1^3\right)\right\rangle\rho_0. \tag{B.92}$$

Taking the average assuming $\langle L(t)\rangle = 0$ and keeping only terms of $\mathcal{O}(\beta^4)$ leads to

$$\dot{\rho}(t) = \left(\langle\mathcal{L}(t)(Q_1+Q_2+Q_3)\rangle + \frac{1}{2}\left\langle\mathcal{L}(t)(Q_1^2+Q_1Q_2+Q_2Q_1)\right\rangle + \frac{1}{6}\left\langle\mathcal{L}(t)Q_1^3\right\rangle\right)\rho_0. \tag{B.93}$$

Since we want to have a time-local expansion we also expand ρ_0 and keep all non-vanishing terms up to order β^2

$$\rho_0 = \exp(-Q_t)\rho_t \tag{B.94}$$
$$\approx (\mathbb{1} - \langle Q_2\rangle + \frac{1}{2}\left\langle Q_1^2\right\rangle)\rho_t, \tag{B.95}$$

such that the final result, sorted by orders of β reads

$$\begin{aligned}\dot{\rho}_t \approx \Big(&\langle\mathcal{L}_tQ_1\rangle + \left\langle\mathcal{L}_tQ_2 + \tfrac{1}{2}\mathcal{L}_tQ_1^2\right\rangle \\ &+ \tfrac{1}{2}\left\langle\mathcal{L}_tQ_3 + \mathcal{L}_t\{Q_1,Q_2\} + \tfrac{1}{3}\mathcal{L}_tQ_1^3\right\rangle - \langle\mathcal{L}_tQ_1\rangle\langle Q_2\rangle \\ &+ \tfrac{1}{2}\langle\mathcal{L}_tQ_1\rangle\left\langle Q_1^2\right\rangle\Big)\rho_t.\end{aligned} \tag{B.96}$$

In order to evaluate this expression we use $\mathcal{L}_t = \beta_t L(t)$ and get

$$\dot{\rho}_t \approx L(t)\left[I_2(t)\left(1 - q_2(t) + \frac{1}{2}q_1^2(t)\right) + I_3(t) + I_4(t)\right]\rho_t, \tag{B.97}$$

where

$$I_2 = \int_0^t dt_1\,\langle\beta_{01}\rangle\,L_1 \tag{B.98}$$
$$I_3 = \frac{1}{2}\left(\int_0^t dt_1\int_0^{t_1} dt_2\,\langle\beta_{012}\rangle\,[L_1,L_2] + \int_0^t dt_1\int_0^t dt_2\,\langle\beta_{012}\rangle\,L_1L_2\right) \tag{B.99}$$

$$I_4 = \frac{1}{6}\int_0^t dt_1 \int_0^{t_1} dt_2 \int_0^{t_2} dt_3 \,\langle \beta_{0123}\rangle \,[L_1,[L_2,L_3]] + [L_3,[L_2,L_1]] \tag{B.100}$$

$$+ \frac{1}{2}\int_0^t dt_1 \int_0^{t} dt_2 \int_0^{t_2} dt_3 \,\langle \beta_{0123}\rangle \, L_1[L_2,L_3] \tag{B.101}$$

$$+ \frac{1}{2}\int_0^t dt_1 \int_0^{t_1} dt_2 \int_0^{t} dt_3 \,\langle \beta_{0123}\rangle \,[L_1,L_2]L_3 \tag{B.102}$$

$$+ \frac{1}{3}\int_0^t dt_1 \int_0^{t} dt_2 \int_0^{t_2} dt_3 \,\langle \beta_{0123}\rangle \, L_1L_2L_3 \tag{B.103}$$

$$q_1^2(t) = \int_0^t dt_1 \int_0^t dt_2 \,\langle \beta_{12}\rangle \, L_1L_2 \tag{B.104}$$

$$q_2(t) = \frac{1}{2}\int_0^t dt_1 \int_0^{t_1} dt_2 \,\langle \beta_{12}\rangle \,[L_1,L_2]. \tag{B.105}$$

B.7. Time-convolutionless (TCL) expansion

This section follows the derivation of Van-Kampen [Van74a; Van74b]. Assume we already transformed to a frame where the noise acts multiplicative on the system's Hamiltonian. Since the noise is considered as a perturbation with smallness parameter α, we can expand the Liouville equation

$$\dot{\rho(t)} = \alpha L(t)\rho(t) \tag{B.106}$$

by taking a Dyson expansion of the solution of this differential equation and averaging. This leads to

$$\langle\rho(t)\rangle = \left[\mathbb{1} + \alpha\int_0^t dt_1 \,\langle L(t_1)\rangle + \alpha^2\int_0^t dt_1 \int_0^{t_1} dt_2 \,\langle L(t_1)L(t_2)\rangle + \dots\right]\rho(0). \tag{B.107}$$

We now write $1,2,\dots$ instead of $\alpha L(t_1), \alpha L(t_2)\dots$ and denote the integration with an overbar, for example $\left\langle\overline{12}\right\rangle = \alpha^2\int_0^t dt_1\int_0^{t_1} dt_2\,\langle L(t_1)L(t_2)\rangle$ and write

$$\langle\rho(t)\rangle = \left[\mathbb{1} + \left\langle\overline{1}\right\rangle + \left\langle\overline{12}\right\rangle + \left\langle\overline{123}\right\rangle + \dots\right]\rho(0). \tag{B.108}$$

We now take the derivative with respect to time and write 0 for $\alpha L(t)$

$$\langle\dot{\rho}(t)\rangle = \left[\langle 0\rangle + \left\langle 0\overline{1}\right\rangle + \left\langle 0\overline{12}\right\rangle + \dots\right]\rho(0). \tag{B.109}$$

Inverting Equation (B.107) by Taylor expanding $\frac{1}{1+x}$ lets us reinsert $\rho(0)$ such that the time local version takes the form

$$\langle\dot{\rho}(t)\rangle = \left[\langle 0\rangle + \left\langle 0\overline{1}\right\rangle + \left\langle 0\overline{12}\right\rangle + \dots\right] \tag{B.110}$$

$$\times \left[\mathbb{1} - \left(\langle \overline{1} \rangle + \langle \overline{12} \rangle + \dots \right) + \left(\langle \overline{1} \rangle + \langle \overline{12} \rangle + \dots \right)^2 - (\dots)^3 + \dots \right] \langle \rho(t) \rangle \,. \quad \text{(B.111)}$$

Now, we work out the products in this equation and sort the resulting terms by orders of α^m. The formal result of this is

$$\langle \dot{\rho}(t) \rangle = \left[\sum_{m=1}^{\infty} \alpha^m S_m(t) \right] \langle \rho(t) \rangle \,, \quad \text{(B.112)}$$

where each $k_m(t)$ is a (m-1)-fold integral

$$k_m(t) = \int_0^t dt_1 \int_0^t dt_2 \cdots \int_0^{t_{m-2}} dt_{m-1} \, \langle L(t) L(t_1) \cdots L(t_{m-1}) \rangle_{oc} \quad \text{(B.113)}$$

and where $\langle \dots \rangle_{oc}$ denotes the time-ordered cumulants, which can be constructed in the following way. Suppose you want to construct a cumulant of order α^m:

(i) Begin by writing a sequence of m dots.

(ii) Partition the sequence into subsequences by inserting angular brackets in all possible ways, ensuring no subsequence is empty.

(iii) For each partition containing p subsequences, include a factor $(-1)^{p-1}$.

(iv) Assign the numeral 0 to the first dot in each partition, and distribute the numerals $1, 2, \dots, m-1$ across the remaining dots in all permutations, ensuring that the numbers do not decrease within any subsequence.

(v) Replace each numeral n with its corresponding operator $A(t_n)$, perform the averaging, and integrate over all variables $t_1, t_2, \dots, t_{m-1}$, subject to the condition $t_1 \leq t_2 \leq \dots \leq t_{m-1}$.

Recently, there was found a recursive way of getting the n-th order from the previous ones [NT19].

Low order terms

Assume we are given a time dependent-Liouville operator in the control frame. It takes the form

$$\mathcal{L}(t) = \beta(t) L(t), \quad \text{(B.114)}$$

where $L(t)$ is a deterministic operator and $\beta(t)$ is a stochastic noise field with zero mean. Then, the first order vanishes because of the vanishing mean, and we are left with the second and higher orders.

$$S^{(2)}(t) = L(t) \int_0^t dt_1 \, \langle \beta(t) \beta(t_1) \rangle \, L(t_1) \quad \text{(B.115)}$$

$$S^{(3)}(t) = \mathrm{i}L(t)\int_0^t dt_1 \int_0^{t_1} dt_2 \,\langle\beta(t)\beta(t_1)\beta(t_2)\rangle\, L(t_1)L(t_2)$$

$$S^{(4)}(t) = -\int_0^t dt_1 \int_0^{t_1} dt_2 \int_0^{t_2} dt_3 \Big[\langle\beta_{0123}\rangle\, L_{0123} - \langle\beta_{01}\rangle\,\langle\beta_{23}\rangle\, L_{0123} - \langle\beta_{02}\beta_{13}\rangle\, L_{0213} - \langle\beta_{03}\rangle\,\langle\beta_{12}\rangle\, L_{0312}\Big].$$

B.8. Pseudo-Lindblad master equation (PLME)

The discussion and method of this section are partially taken from [Gro+23]. The PLME method is the TCL expansion method under the assumptions of Gaussian noise (in this case we can simplify Equation (B.115) to get)

$$\partial_t\rho(t) = \mathcal{R}(t)\rho(t) \tag{B.116}$$
$$= (\mathcal{R}_2(t) + \mathcal{R}_4(t) + \dots)\rho(t), \tag{B.117}$$

where

$$\mathcal{R}_2 = \mathcal{L}(t)\int_0^t dt_1 S_{01}\mathcal{L}(t_1) \tag{B.118}$$

and

$$\mathcal{R}_4(t) = \mathcal{L}(t)\int_0^t dt_1 \int_0^{t_1} dt_2 \int_0^{t_2} dt_3 \tag{B.119}$$
$$\Big(S_{02}S_{13}[\mathcal{L}_1,\mathcal{L}_2]\mathcal{L}_3 \tag{B.120}$$
$$+ S_{03}S_{12}\mathcal{L}_1[\mathcal{L}_2,\mathcal{L}_3] \tag{B.121}$$
$$+ S_{03}S_{12}[\mathcal{L}_1,\mathcal{L}_3]\mathcal{L}_2\Big). \tag{B.122}$$

Here, $S_{ij} = \langle\beta(t_i)\beta(t_j)\rangle$ has been defined.

B.9. Calculation of multipoint correlators

B.9.1. Gaussian case

For a Gaussian process we can use Isserlis' theorem which states that for a centered process all odd correlators vanish which also implies

$$\langle\beta(t_1)\beta(t_2)\beta(t_3)\rangle = 0. \tag{B.123}$$

It further allows us to express the next non-vanishing correlator in terms of two-point correlators

$$\begin{aligned}\langle\beta(t_1)\beta(t_2)\beta(t_3)\beta(t_4)\rangle = &\langle\beta(t_1)\beta(t_2)\rangle\langle\beta(t_3)\beta(t_4)\rangle \\ &+ \langle\beta(t_1)\beta(t_3)\rangle\langle\beta(t_2)\beta(t_4)\rangle \\ &+ \langle\beta(t_1)\beta(t_4)\rangle\langle\beta(t_2)\beta(t_3)\rangle\,.\end{aligned} \tag{B.124}$$

Especially, if the process is the Ornstein-Uhlenbeck process, with parameters σ, κ and correlation function

$$\langle\beta(t_1)\beta(t_2)\rangle = \frac{\sigma^2}{2\kappa}\exp\{-\kappa(|t_2 - t_1|)\} \tag{B.125}$$

we have

$$\langle\beta(t_1)\beta(t_2)\beta(t_3)\beta(t_4)\rangle = \frac{\sigma^4}{4\kappa^2}\left(\exp\{-\kappa(|t_2 - t_1| + |t_4 - t_3|)\}\right. \tag{B.126}$$

$$+ \exp\{-\kappa(|t_3 - t_1| + |t_4 - t_2|)\} \tag{B.127}$$

$$\left. + \exp\{-\kappa(|t_3 - t_2| + |t_4 - t_1|)\}\right)\,. \tag{B.128}$$

Since these expressions only occur time-ordered ($t_1 > t_2 > t_3 > t_4$)in the differential equations we can further simplify

$$\langle\beta(t_1)\beta(t_2)\beta(t_3)\beta(t_4)\rangle = \frac{\sigma^4\left(\mathrm{e}^{2\kappa t_2} + 2\mathrm{e}^{2\kappa t_3}\right)\mathrm{e}^{-\kappa(t_1+t_2+t_3-t_4)}}{4\kappa^2} \tag{B.129}$$

B.9.2. Random telegraph process

For a symmetric two level fluctuator we have to evaluate this manually: the probability of an even or odd number of switches happening between t_i and t_j is

$$P(\text{even switches in } |t_i - t_j|) = \frac{1 + \mathrm{e}^{-2\gamma|t_i - t_j|}}{2} \tag{B.130}$$

$$P(\text{odd switches in } |t_i - t_j|) = \frac{1 - \mathrm{e}^{-2\gamma|t_i - t_j|}}{2}. \tag{B.131}$$

which leads to

$$\frac{\langle\beta(t_1)\beta(t_2)\beta(t_3)\rangle}{g^3} = P(\text{even, even}) + P(\text{odd, odd}) \tag{B.132}$$

$$- P(\text{odd, even}) - P(\text{even, odd}). \tag{B.133}$$

It follows after some algebra

$$\langle\beta(t_1)\beta(t_2)\beta(t_3)\rangle = g^3\exp\{-2\gamma(|t_1 - t_2| + |t_2 - t_3|)\} \tag{B.134}$$

and again assuming $t_1 > t_2 > t_3$ leads to

$$\langle\beta(t_1)\beta(t_2)\beta(t_3)\rangle = g^3\exp\{-2\gamma(t_1 - t_3)\}. \tag{B.135}$$

Similarly we have

$$\langle\beta(t_1)\beta(t_2)\beta(t_3)\beta(t_4)\rangle/g^4 = \tag{B.136}$$
$$P(\text{even, even, even}) + P(\text{odd, odd, even}) + P(\text{odd, even, odd}) + P(\text{even, odd, odd}) \tag{B.137}$$
$$- P(\text{odd, odd, odd}) - P(\text{even, even, odd}) - P(\text{even, odd, even}) - P(\text{odd, even, even}). \tag{B.138}$$

After some algebra this simplifies to

$$\langle\beta(t_1)\beta(t_2)\beta(t_3)\beta(t_4)\rangle = g^4 \exp\left(-2\gamma\left(|t_1 - t_2| + |t_2 - t_3| + |t_3 - t_4|\right)\right) \tag{B.139}$$

again assuming $t_1 > t_2 > t_3 > t_4$ we are left with

$$\langle\beta(t_1)\beta(t_2)\beta(t_3)\beta(t_4)\rangle = g^4 \exp\{-2\gamma(t_1 - t_4)\}. \tag{B.140}$$

B.9.3. Centered squared gaussian noise

Given a zero-mean Gaussian process, β_t we can define a centered Non-Gaussian process $\xi(t) = \beta^2(t) - \sigma^2$ [Sun+19] by taking its square and subtracting the mean. We can now make again use of Isserlis theorem to give the following multipoint correlators:

$$\langle\xi(t_1)\xi(t_2)\rangle = \left\langle(\beta^2(t_1) - \sigma^2)(\beta^2(t_2) - \sigma^2)\right\rangle \tag{B.141}$$
$$= \left\langle\beta^2(t_1)\beta^2(t_2)\right\rangle - \sigma^4 \tag{B.142}$$
$$= 2\left\langle\beta(t_1)\beta(t_2)\right\rangle^2 \tag{B.143}$$
$$= 2C_\beta(t_1, t_2)^2 \tag{B.144}$$

and after some algebra we get

$$\langle\xi_1\xi_2\xi_3\rangle = 8C_\beta(t_1, t_2)C_\beta(t_1, t_3)C_\beta(t_2, t_3) \tag{B.145}$$

and after some more algebra

$$\begin{aligned}\langle\xi_1\xi_2\xi_3\xi_4\rangle =& 4\Big(C_\beta(t_1, t_2)^2C_\beta(t_3, t_4)^2 + C_\beta(t_1, t_3)^2C_\beta(t_2, t_4)^2 + C_\beta(t_1, t_4)^2C_\beta(t_2, t_3)^2\Big) \\ &+ 16\Big[C_\beta(t_1, t_2)C_\beta(t_1, t_3)C_\beta(t_2, t_4)C_\beta(t_3, t_4) \\ &\quad + C_\beta(t_1, t_3)C_\beta(t_1, t_4)C_\beta(t_2, t_3)C_\beta(t_2, t_4) \\ &\quad + C_\beta(t_1, t_2)C_\beta(t_1, t_4)C_\beta(t_2, t_3)C_\beta(t_3, t_4)\Big].\end{aligned} \tag{B.146}$$

More details can be found in [Grü72].

B.10. TCL-performance

We benchmark the TCL/PLME approach across different noise regimes. All time integrals entering the perturbative expansions are evaluated analytically using Mathematica. The resulting dynamics are compared in Figure B.1.

B.11. Mapping pure dephasing Spin-Star system to semi-classical dynamics

In this chapter, we show how an analytically solvable system, described by a Lindblad master equation, can be equivalently described by averaging the dynamics over a stochastic, Gaussian process. We start with the (time independent) spin-star model and translate it step-by-step into a stochastic semi-classical model, this has to our knowledge not been done yet. The Hamiltonian for a spin surrounded by N spins which couple via ZZ interaction can be written as

$$H = \frac{\omega_0}{2} Z \otimes \mathbb{1}_B + \sum_{k=1}^{N} \frac{\Omega_k}{2} \mathbb{1} \otimes Z^{(k)} + \alpha \sum_{k=1}^{N} g_k Z \otimes Z^{(k)}, \tag{B.147}$$

where Z^k is the Pauli-Z operator acting on the k-th spin. Assuming $g_k = 1$ and $\Omega_k = \Omega$, we can find the Lindblad equation for the centered spin in the interaction picture as [Sin+24]

$$\begin{aligned} \dot{\rho}_S(t) &= -\mathrm{i}\,\mathrm{Im}\{g(t)\}[Z, \rho_S] + \mathrm{Re}\{g(t)\}(Z\rho_S(t)Z - \rho_S) && \text{(B.148)} \\ &= -\mathrm{i}S(t)[Z, \rho_S] + \gamma(t)(Z\rho_S(t)Z - \rho_S), && \text{(B.149)} \end{aligned}$$

where

$$g(t) = \frac{N}{\cos(4t) + \cosh(-\beta\Omega)} [\sin(4t) + \mathrm{i}\sinh(-\beta\Omega)]. \tag{B.150}$$

We can also try to model the systems' dynamics by a semi-classical stochastic noise process with

$$H(t) = \eta(t) Z. \tag{B.151}$$

As seen later η can be chosen as a Gaussian process. The dynamics for a single noise realization, with initial density matrix $\rho_0 = \frac{1}{2}(1 + xX + yY + zZ)$ are then given as

$$\begin{aligned} \rho_k(t) &= \mathrm{e}^{-\mathrm{i}\int_0^t H_k(t')dt' Z} \rho_0 \mathrm{e}^{-\mathrm{i}\int_0^t H_k(t')dt' Z} && \text{(B.152)} \\ &= \frac{1}{2} \begin{pmatrix} 1+z & \exp\{-2\mathrm{i}\Phi_k(t)\}(x - iy) \\ \exp\{2\mathrm{i}\Phi_k(t)\}(x + iy) & 1-z \end{pmatrix}, && \text{(B.153)} \end{aligned}$$

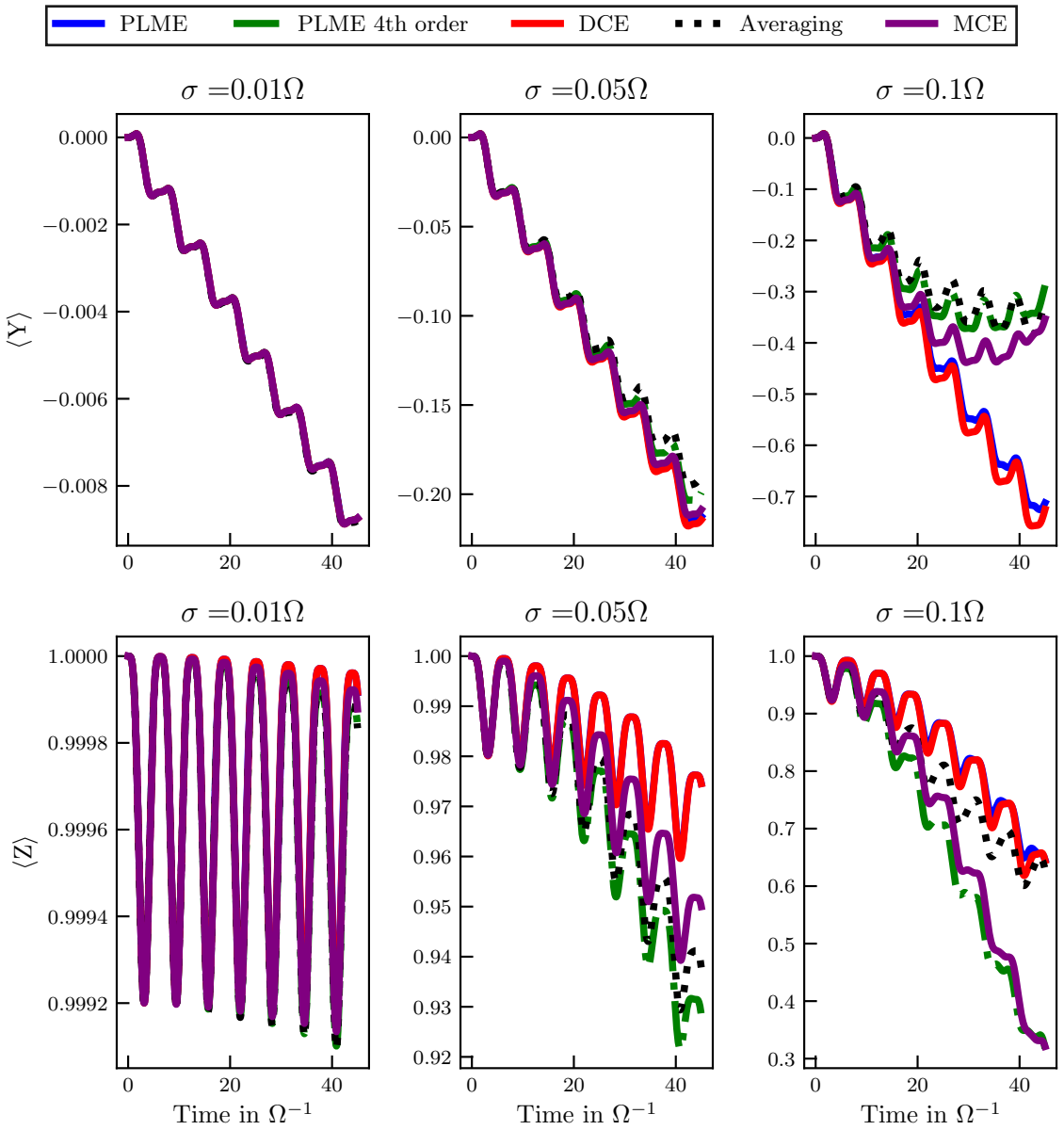

Figure B.1.: Comparison of the propagation methods introduced in this chapter against static dephasing noise. The dotted results are averaged over 10,000 noise realizations and all integral methods are evaluated analytically using Mathematica. While all methods exhibit noticeable deviations from the reference dynamics at long times, the fourth-order approaches PLME 4th order and MCE show a modest but systematic improvement.

where $\Phi_k(t) = \int_0^t \eta_k(s)ds$ is the accumulated phase for the k-th noise realization. If we average now over multiple noise realizations, we get

$$\rho(t) = \frac{1}{2}\begin{pmatrix} 1+z & \bar{G}(t)(x-iy) \\ G(t)(x+iy) & 1-z \end{pmatrix}, \tag{B.154}$$

where $G(t) = \langle \exp[2i\Phi(t)] \rangle$, which we identify as the characteristic function of Φ at $z = 2$. It follows

$$\dot{\rho} = \frac{1}{2}\begin{pmatrix} 0 & \dot{\bar{G}}(t)(x-iy) \\ \dot{G}(t)(x+iy) & 0 \end{pmatrix}. \tag{B.155}$$

Starting from the LME we have

$$\dot{\rho} = -iS(t)[Z,\rho] + \gamma(t)(Z\rho Z - \rho) \tag{B.156}$$

$$\overset{B.154}{=} \begin{pmatrix} 0 & \bar{G}(t)(x-iy)(-iS(t)-\gamma(t)) \\ G(t)(x+iy)(iS(t)-\gamma) & 0 \end{pmatrix}. \tag{B.157}$$

Comparing Equation (B.155) and Equation (B.157) leads to

$$\frac{\dot{G}(t)}{G(t)} = -2(\gamma(t) + iS(t)) \tag{B.158}$$

or equivalently

$$2\gamma(t) = -\operatorname{Re}\left\{\frac{\dot{G}}{G}\right\} \tag{B.159}$$

$$2S(t) = \operatorname{Im}\left\{\frac{\dot{G}}{G}\right\}. \tag{B.160}$$

We therefore find

$$G(t) = \exp\{-2\Gamma(t) + 2i\Lambda(t)\}, \tag{B.161}$$

where $\Gamma(t) = \int_0^t \gamma(s)ds$ and $\Lambda(s) = \int_0^t S(t')dt'$. This results in

$$\Gamma(\tau) = \frac{1}{4}N \log\left(\frac{\cosh(\beta\Omega)+1}{\cos(4\alpha\tau)+\cosh(\beta\Omega)}\right) \tag{B.162}$$

and

$$\Lambda(\tau) = -\frac{1}{2}N \tan^{-1}\left(\tan(2\alpha\tau)\tanh\left(\frac{\beta\Omega}{2}\right)\right) \tag{B.163}$$

$$\text{if } \csc(2\alpha\tau) \neq 0 \wedge 4\alpha\tau < \pi \wedge \cos(4\alpha\tau) + \cosh(\beta\Omega) > 0. \tag{B.164}$$

A (Gaussian) process $\Phi(t)$ has the characteristic function

$$\chi_\Phi(z) = \exp\left\{-\frac{1}{2}\sigma^2(t)z^2 + iz\mu(t)\right\} \tag{B.165}$$

$$\overset{z=2}{=} \exp\left\{-2\sigma^2(t)z^2 + 2i\mu(t)\right\}. \tag{B.166}$$

Therefore we get the requested dynamics by letting $\sigma^2(t) = \Gamma(t)$ and $\mu(t) = \Lambda(t)$

$$\Phi(t) \sim \mathcal{N}(\Lambda(t), \Gamma(t)). \tag{B.167}$$

It would be nice to sample not from Φ, but from its time-derivative. It is not defined in the classical sense, but in the Ito-sense, and we know that the derivative of a Gaussian process is again a Gaussian process. These are fully characterized by their mean and auto-correlation function. We can write

$$\Phi(t) = \Lambda(t) + \sqrt{\Gamma(t)}\xi, \tag{B.168}$$

where $\xi \sim \mathcal{N}(0,1)$ and derive:

$$\langle \eta(t) \rangle = \dot{\Lambda} = S(t) \tag{B.169}$$

$$\langle \tilde{\eta}(t)\tilde{\eta}(t') \rangle = \partial_t \partial_{t'} \left\langle \tilde{\Phi}(t)\tilde{\Phi}(t') \right\rangle \tag{B.170}$$

$$= \frac{\gamma(t)\gamma(t')}{4\sqrt{\Gamma(t)\Gamma(t')}} \tag{B.171}$$

where $\tilde{\eta}(t) = \eta(t) - S(t)$ and $\tilde{\Phi}(t)$ are the centered versions of the corresponding random variable. In Figure B.2 we show the results for $N = 1000$ noise realizations. We see very good agreement and conclude that both methods are indeed equivalent.

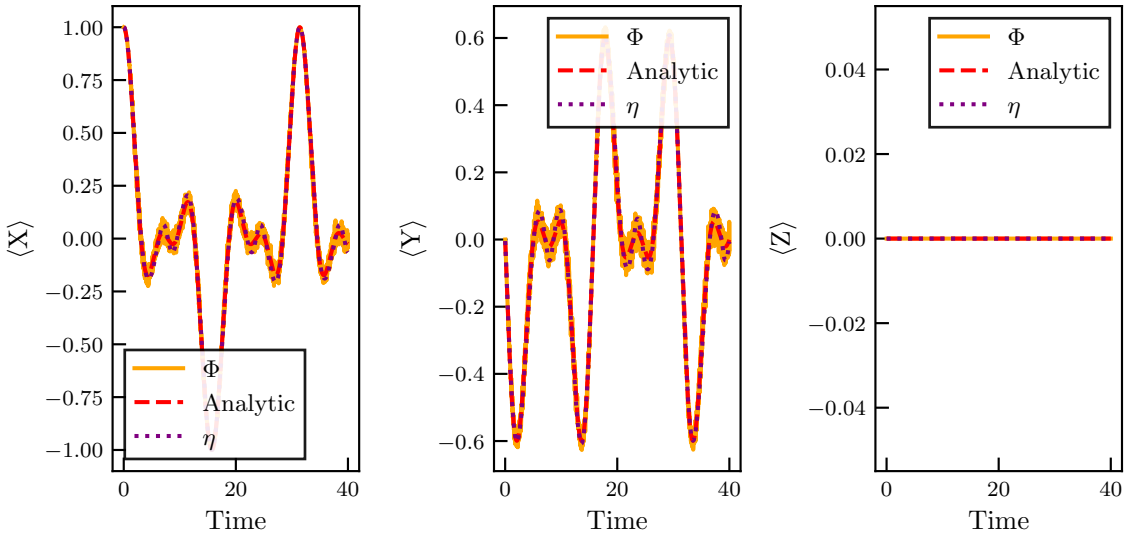

Figure B.2.: Dynamics of the centered spin of the ZZ-spinstar calculated ones analytically, ones by sampling Φ and once by sampling η. The parameters for the simulation were $T = 40, dt = 0.01, \alpha = 0.1, \beta = 0.1, \Omega = 10, N = 5$.

Bibliography

[Aas+25] David Aasen et al. *Roadmap to fault tolerant quantum computation using topological qubit arrays*. arXiv preprint. Station Q conference paper on scaling Majorana-1 to multi-qubit systems. Feb. 2025.

[Abd+24] Leonid Abdurakhimov et al. "Technology and Performance Benchmarks of IQM's 20-Qubit Quantum Computer". In: *arXiv preprint arXiv:2408.12433* (2024).

[Abu25] Muhammad AbuGhanem. "IBM quantum computers: evolution, performance, and future directions". In: *The Journal of Supercomputing* 81.5 (2025), p. 687.

[Ach+24] Rajeev Acharya et al. "Quantum error correction below the surface code threshold". In: *arXiv preprint arXiv:2408.13687* (2024).

[Agh+25] Morteza Aghaee et al. "Interferometric single-shot parity measurement in InAs–Al hybrid devices". In: *Nature* (Feb. 2025). Majorana 1 topological qubit platform, measurement of fermion parity. DOI: 10.1038/s41586-024-08445-2.

[AJ07] William G Alway and Jonathan A Jones. "Arbitrary precision composite pulses for NMR quantum computing". In: *Journal of Magnetic Resonance* 189.1 (2007), pp. 114–120.

[AKN98] Dorit Aharonov, Alexei Kitaev, and Noam Nisan. "Quantum circuits with mixed states". In: *Proceedings of the thirtieth annual ACM symposium on Theory of computing*. 1998, pp. 20–30.

[AS11] Gonzalo A. Alvarez and Dieter Suter. "Dynamical decoupling noise spectroscopy". In: *Phys. Rev. Lett.* 107.23 (Nov. 30, 2011), p. 230501. ISSN: 0031-9007, 1079-7114. DOI: 10.1103/PhysRevLett.107.230501. arXiv: 1106.3463[cond-mat,physics:physics,physics:quant-ph]. URL: http://arxiv.org/abs/1106.3463 (visited on 07/24/2024).

[ASK19] Mohamed Abdelhafez, David I Schuster, and Jens Koch. "Gradient-based optimal control of open quantum systems using quantum trajectories and automatic differentiation". In: *Physical Review A* 99.5 (2019), p. 052327.

[Aum+04] Joe Aumentado et al. "Nonequilibrium quasiparticles and 2 e periodicity in single-cooper-pair transistors". In: *Physical review letters* 92.6 (2004), p. 066802.

[Aws+25] David D Awschalom et al. "Challenges and opportunities for quantum information hardware". In: *Science* 390.6777 (2025), pp. 1004–1010.

[Bar+13] Nir Bar-Gill et al. “Solid-state electronic spin coherence time approaching one second”. In: *Nature communications* 4.1 (2013), p. 1743.

[Bar+14] Rami Barends et al. “Superconducting quantum circuits at the surface code threshold for fault tolerance”. In: *Nature* 508.7497 (2014), pp. 500–503.

[Bar+20] John F Barry et al. “Sensitivity optimization for NV-diamond magnetometry”. In: *Reviews of Modern Physics* 92.1 (2020), p. 015004.

[Bar+25] HP Bartling et al. “Universal high-fidelity quantum gates for spin qubits in diamond”. In: *Physical Review Applied* 23.3 (2025), p. 034052.

[Bar+95] Adriano Barenco et al. “Elementary gates for quantum computation”. In: *Physical review A* 52.5 (1995), p. 3457.

[BC94] Samuel L Braunstein and Carlton M Caves. “Statistical distance and the geometry of quantum states”. In: *Physical Review Letters* 72.22 (1994), p. 3439.

[BD12] Edwin Barnes and Sankar Das Sarma. “Analytically solvable driven time-dependent two-level quantum systems”. In: *Physical review letters* 109.6 (2012), p. 060401.

[BE20] Tuguldur Kh Begzjav and Hichem Eleuch. “Magnus expansion applied to a dissipative driven two-level system”. In: *Results in Physics* 17 (2020), p. 103098.

[Bha+20] Mihir K Bhaskar et al. “Experimental demonstration of memory-enhanced quantum communication”. In: *Nature* 580.7801 (2020), pp. 60–64.

[BJG23] Bora Basyildiz, Casey Jameson, and Zhexuan Gong. “Speed limits of two-qubit gates with qudits”. In: *arXiv preprint arXiv:2312.09218* (2023).

[BP02] H.-P. Breuer and F. Petruccione. *The Theory of Open Quantum Systems*. Oxford: Oxford University Press, 2002. ISBN: 978-0-19-921390-0.

[Bra+19] Carlo Bradac et al. “Quantum nanophotonics with group IV defects in diamond”. In: *Nature communications* 10.1 (2019), p. 5625.

[Bun25] Bundesamt für Sicherheit in der Informationstechnik. *Entwicklungsstand Quantencomputer (Zusammenfassung in deutscher Sprache) V2.1*. Tech. rep. Accessed: 2025-02-13. Bundesamt für Sicherheit in der Informationstechnik, Jan. 2025. URL: `https://www.bsi.bund.de/SharedDocs/Downloads/DE/BSI/Publikationen/Studien/Quantencomputer/Entwicklungsstand_QC_Zusammenfassung_V_2_1.html`.

[Bur69] Donald Bures. “An extension of Kakutani’s theorem on infinite product measures to the tensor product of semifinite w*-algebras”. In: *Transactions of the American Mathematical Society* 135 (1969), pp. 199–212.

[Cai+23] Zhenyu Cai et al. “Quantum error mitigation”. In: *Reviews of Modern Physics* 95.4 (2023), p. 045005.

[Car09] Donatella Carbonera. "Optically detected magnetic resonance (ODMR) of photoexcited triplet states". In: *Photosynthesis research* 102.2 (2009), pp. 403–414.

[CCK24] Eunmi Chae, Joonhee Choi, and Junki Kim. "An elementary review on basic principles and developments of qubits for quantum computing". In: *Nano Convergence* 11.1 (2024), p. 11.

[Chr+19] BG Christensen et al. "Anomalous charge noise in superconducting qubits". In: *Physical Review B* 100.14 (2019), p. 140503.

[CLJ03] H. K. Cummins, G. Llewellyn, and J. A. Jones. "Tackling systematic errors in quantum logic gates with composite rotations". In: *Physical Review A* 67.4 (2003), p. 042308. DOI: 10.1103/PhysRevA.67.042308.

[CW08] John Clarke and Frank K Wilhelm. "Superconducting quantum bits". In: *Nature* 453.7198 (2008), pp. 1031–1042.

[CWP17] J Casanova, Z-Y Wang, and Martin B Plenio. "Arbitrary Nuclear Spin Gates in Diamond Mediated by a NV-center Electron Spin". In: *arXiv preprint arXiv:1702.05330* (2017).

[Cyw+08] Łukasz Cywiński et al. "How to enhance dephasing time in superconducting qubits". In: *Physical Review B—Condensed Matter and Materials Physics* 77.17 (2008), p. 174509.

[DAl07] Domenico D'Allessandro. *Introduction to Quantum Control and Dynamics*. Boca Raton, FL: Chapman and Hall/CRC, 2007. ISBN: 978-1-58488-884-0.

[dAl21] Domenico d'Alessandro. *Introduction to quantum control and dynamics*. Chapman and hall/CRC, 2021.

[DC17] Sebastian Deffner and Steve Campbell. "Quantum speed limits: from Heisenberg's uncertainty principle to optimal quantum control". In: *Journal of Physics A: Mathematical and Theoretical* 50.45 (2017), p. 453001.

[DH76] Gordon Davies and MF Hamer. "Optical studies of the 1.945 eV vibronic band in diamond". In: *Proceedings of the Royal Society of London. A. Mathematical and Physical Sciences* 348.1653 (1976), pp. 285–298.

[Did+18] Nicolas Didier et al. "Analytical modeling of parametrically modulated transmon qubits". In: *Physical Review A* 97.2 (2018), p. 022330.

[DN05] Christopher M Dawson and Michael A Nielsen. "The solovay-kitaev algorithm". In: *arXiv preprint quant-ph/0505030* (2005).

[Fah+23] Alfaiz Fahrurrachman et al. "Simulating Decoherence of a Nitrogen–Vacancy Centre Spin Qubit via Ornstein–Uhlenbeck Process". In: *Journal of Physics: Conference Series*. Vol. 2498. 1. IOP Publishing. 2023, p. 012025.

[Fer06] Jesse Fern. “Expectations of two-level telegraph noise”. In: *arXiv preprint quant-ph/0611020* (2006).

[Fey82] Richard P Feynman. “Simulating Physics with Computers”. In: *International Journal of Theoretical Physics* 21.6/7 (1982).

[Fey86] Richard P Feynman. “Quantum mechanical computers.” In: *Found. Phys.* 16.6 (1986), pp. 507–532.

[For+15] Simon Forest et al. “Exact synthesis of single-qubit unitaries over Clifford-cyclotomic gate sets”. In: *Journal of Mathematical Physics* 56.8 (2015), p. 082201.

[Fre20] Jurek Frey. “Dynamisches Entkoppeln für supraleitende Qubits”. Master’s thesis. Saarbrücken, Germany: Universität des Saarlandes, Feb. 2020.

[FV02] Christopher A Fuchs and Jeroen Van De Graaf. “Cryptographic distinguishability measures for quantum-mechanical states”. In: *IEEE Transactions on Information Theory* 45.4 (2002), pp. 1216–1227.

[GLM03a] Vittorio Giovannetti, Seth Lloyd, and Lorenzo Maccone. “Quantum limits to dynamical evolution”. In: *Phys. Rev. A* 67 (2003), p. 052109. DOI: 10.1103/PhysRevA.67.052109.

[GLM03b] Vittorio Giovannetti, Seth Lloyd, and Lorenzo Maccone. “The quantum speed limit”. In: *Fluctuations and Noise in Photonics and Quantum Optics*. Vol. 5111. Proceedings of SPIE. 2003, pp. 1–6.

[GLM04] Vittorio Giovannetti, Seth Lloyd, and Lorenzo Maccone. “The speed limit of quantum unitary evolution”. In: *J. Opt. B: Quantum Semiclass. Opt.* 6 (2004), p. 807. DOI: 10.1088/1464-4266/6/8/028.

[Gri+25] Nick Grimm et al. “Coherent Control of a Long-Lived Nuclear Memory Spin in a Germanium-Vacancy Multi-Qubit Node”. In: *Physical Review Letters* 134.4 (2025), p. 043603.

[Gro+23] Peter Groszkowski et al. “Simple master equations for describing driven systems subject to classical non-Markovian noise”. In: *Quantum* 7 (2023), p. 972.

[Gru+97] A Gruber et al. “Scanning confocal optical microscopy and magnetic resonance on single defect centers”. In: *Science* 276.5321 (1997), pp. 2012–2014.

[Grü72] F Alberto Grünbaum. “The square of a Gaussian process”. In: *Zeitschrift für Wahrscheinlichkeitstheorie und Verwandte Gebiete* 23.2 (1972), pp. 121–124.

[Gun+25] Prithvi Gundlapalli et al. “High-Fidelity Single-Shot Readout and Selective Nuclear Spin Control for a Spin-1/2 Quantum Register in Diamond”. In: *arXiv preprint arXiv:2510.09164* (2025).

[GWK15] Michael H Goerz, K Birgitta Whaley, and Christiane P Koch. "Hybrid optimization schemes for quantum control". In: *EPJ Quantum Technology* 2.1 (2015), pp. 1–16.

[GZ04] C. W. Gardiner and P. Zoller. *Quantum Noise*. 3rd. Berlin: Springer, 2004. ISBN: 978-3540223016.

[HE24] Isaac BW Harris and Dirk Englund. "Coherence of group-IV color centers". In: *Physical Review B* 109.8 (2024), p. 085414.

[Her+19] ED Herbschleb et al. "Ultra-long coherence times amongst room-temperature solid-state spins". In: *Nature communications* 10.1 (2019), p. 3766.

[Hui+23] William Huie et al. "Repetitive Readout and Real-Time Control of Nuclear Spin Qubits in 171 Yb Atoms". In: *PRX Quantum* 4.3 (Sept. 18, 2023), p. 030337. ISSN: 2691-3399. DOI: 10.1103/PRXQuantum.4.030337. URL: https://link.aps.org/doi/10.1103/PRXQuantum.4.030337 (visited on 09/18/2024).

[HW68] Ulrich Haeberlen and John S Waugh. "Coherent averaging effects in magnetic resonance". In: *Physical Review* 175.2 (1968), p. 453.

[IG25] François Impens and D GuÃŠry-Odelin. "Approaching the Quantum Speed Limit in Quantum Gates with Geometric Control". In: *arXiv preprint arXiv:2501.05330* (2025).

[Ith+05] G Ithier et al. "Decoherence in a superconducting quantum bit circuit". In: *Physical Review B—Condensed Matter and Materials Physics* 72.13 (2005), p. 134519.

[Iwa+15] Takayuki Iwasaki et al. "Germanium-vacancy single color centers in diamond". In: *Scientific reports* 5.1 (2015), p. 12882.

[Iwa+17] Takayuki Iwasaki et al. "Tin-vacancy quantum emitters in diamond". In: *Physical review letters* 119.25 (2017), p. 253601.

[Jef60] CD Jeffries. "Dynamic orientation of nuclei by forbidden transitions in paramagnetic resonance". In: *Physical Review* 117.4 (1960), p. 1056.

[Jon+21] Tyler Jones et al. "Approximations in transmon simulation". In: *Physical Review Applied* 16.5 (2021), p. 054039.

[Joz94] Richard Jozsa. "Fidelity for mixed quantum states". In: *Journal of modern optics* 41.12 (1994), pp. 2315–2323.

[JW04] F Jelezko and J Wrachtrup. "Read-out of single spins by optical spectroscopy". In: *Journal of Physics: Condensed Matter* 16.30 (2004), R1089.

[Kak48] Shizuo Kakutani. "On equivalence of infinite product measures". In: *Annals of Mathematics* 49.1 (1948), pp. 214–224.

[Kha+05] Navin Khaneja et al. "Optimal control of coupled spin dynamics: design of NMR pulse sequences by gradient ascent algorithms". In: *Journal of magnetic resonance* 172.2 (2005), pp. 296–305.

[Kja+20] Morten Kjaergaard et al. "Superconducting Qubits: Current State of Play". In: *Annual Review of Condensed Matter Physics* 11.1 (Mar. 2020), pp. 369–395. DOI: 10.1146/annurev-conmatphys-031119-050605. URL: https://doi.org/10.1146/annurev-conmatphys-031119-050605.

[KKK22] Shingo Kukita, Haruki Kiya, and Yasushi Kondo. "General off-resonance-error-robust symmetric composite pulses with three elementary operations". In: *Physical Review A* 106.4 (2022), p. 042613.

[Klo+22] Marco Klotz et al. "Prolonged orbital relaxation by locally modified phonon density of states for the Si V-center in nanodiamonds". In: *Physical Review Letters* 128.15 (2022), p. 153602.

[Kna+24] Can M Knaut et al. "Entanglement of nanophotonic quantum memory nodes in a telecom network". In: *Nature* 629.8012 (2024), pp. 573–578.

[Koc+07] Jens Koch et al. "Charge-insensitive qubit design derived from the Cooper pair box". In: *Physical Review A—Atomic, Molecular, and Optical Physics* 76.4 (2007), p. 042319.

[Koc+22] Christiane P Koch et al. "Quantum optimal control in quantum technologies. Strategic report on current status, visions and goals for research in Europe". In: *EPJ Quantum Technology* 9.1 (2022), p. 19.

[Kra+19] Philip Krantz et al. "A Quantum Engineer's Guide to Superconducting Qubits". In: *Applied Physics Reviews* (2019). DOI: 10.1063/1.5089550. URL: https://doi.org/10.1063/1.5089550.

[Kra+21] Philip Krantz et al. *A Quantum Engineer's Guide to Superconducting Qubits*. July 7, 2021. DOI: 10.1063/1.5089550. arXiv: 1904.06560[cond-mat,physics:physics,physics:quant-ph]. URL: http://arxiv.org/abs/1904.06560 (visited on 09/17/2024).

[Kra+24] J Krause et al. "Quasiparticle effects in magnetic-field-resilient three-dimensional transmons". In: *Physical Review Applied* 22.4 (2024), p. 044063.

[KSK21] SMJ Khadem, NH Siboni, and SHL Klapp. "Transport and phase separation of active Brownian particles in fluctuating environments". In: *Physical Review E* 104.6 (2021), p. 064615.

[Lin+19] Junan Lin et al. "On the freedom in representing quantum operations". In: *New Journal of Physics* 21.2 (2019), p. 023006.

[Liu+24] Chuan-Hong Liu et al. "Quasiparticle poisoning of superconducting qubits from resonant absorption of pair-breaking photons". In: *Physical Review Letters* 132.1 (2024), p. 017001.

[Lüp+20] Uwe von Lüpke et al. "Two-qubit spectroscopy of spatiotemporally correlated quantum noise in superconducting qubits". In: *PRX Quantum* 1.1 (2020), p. 010305.

[Mac+15] Shai Machnes et al. "Gradient optimization of analytic controls: the route to high accuracy quantum optimal control". In: *arXiv preprint arXiv:1507.04261* (2015).

[Mac+18] Shai Machnes et al. "Tunable, flexible, and efficient optimization of control pulses for practical qubits". In: *Physical review letters* 120.15 (2018), p. 150401.

[Maj+23] Ritajit Majumdar et al. *Best practices for quantum error mitigation with digital zero-noise extrapolation*. 2023. arXiv: 2307.05203 [quant-ph]. URL: https://arxiv.org/abs/2307.05203.

[McK+17] David C McKay et al. "Efficient Z gates for quantum computing". In: *Physical Review A* 96.2 (2017), p. 022330.

[MG58] S Meiboom and D Gill. "Modified spin-echo method for measuring nuclear relaxation times". In: *Review of Scientific Instruments* 29.8 (1958), pp. 688–691.

[Mot+09] Felix Motzoi et al. "Simple pulses for elimination of leakage in weakly nonlinear qubits". In: *Physical review letters* 103.11 (2009), p. 110501.

[MP19] Oleg V Morzhin and Alexander N Pechen. "Krotov method for optimal control of closed quantum systems". In: *Russian Mathematical Surveys* 74.5 (2019), p. 851.

[Mül+22] Matthias M Müller et al. "One decade of quantum optimal control in the chopped random basis". In: *Reports on progress in physics* 85.7 (2022), p. 076001.

[MW13] Felix Motzoi and Frank K Wilhelm. "Improving frequency selection of driven pulses using derivative-based transition suppression". In: *Physical Review A—Atomic, Molecular, and Optical Physics* 88.6 (2013), p. 062318.

[NC00] Michael A. Nielsen and Isaac L. Chuang. *Quantum Computation and Quantum Information*. 1st. Cambridge, UK: Cambridge University Press, 2000. ISBN: 978-0-521-63503-5.

[Nev24] Hartmut Neven. *Meet Willow, our state-of-the-art quantum chip*. Accessed: 2025-02-13. 2024. URL: https://blog.google/technology/research/google-willow-quantum-chip/.

[Nie02] Michael A Nielsen. "A simple formula for the average gate fidelity of a quantum dynamical operation". In: *Physics Letters A* 303.4 (2002), pp. 249–252.

[NKa24] Hartmut Neven, Julian Kelly, and et al. “Quantum error correction below the surface-code threshold with a 105-qubit processor”. In: *Nature* (Dec. 2024). Willow processor; 105-qubit superconducting transmon. DOI: 10.1038/s41586-024-08449-y.

[NPT99] Yasunobu Nakamura, Yu A Pashkin, and JS Tsai. “Coherent control of macroscopic quantum states in a single-Cooper-pair box”. In: *nature* 398.6730 (1999), pp. 786–788.

[NPV16] Leigh M Norris, Gerardo A Paz-Silva, and Lorenza Viola. “Qubit noise spectroscopy for non-Gaussian dephasing environments”. In: *Physical review letters* 116.15 (2016), p. 150503.

[NT19] Konstantin Nestmann and Carsten Timm. “Time-convolutionless master equation: Perturbative expansions to arbitrary order and application to quantum dots”. In: *arXiv preprint arXiv:1903.05132* (2019).

[OG89] Eric van Oort and Max Glasbeek. “Cross-relaxation dynamics of optically excited N-V centers in diamond”. In: *Physical Review B* 40.10 (1989), p. 6509.

[Pal+14] E Paladino et al. “1/f noise: Implications for solid-state quantum information”. In: *Reviews of Modern Physics* 86.2 (2014), pp. 361–418.

[Pan+22] Xianchuang Pan et al. “Engineering superconducting qubits to reduce quasiparticles and charge noise”. In: *Nature Communications* 13.1 (2022), p. 7196.

[Pat+24] Anand Patel et al. “Single and double quantum transitions in spin-mixed states under photo-excitation”. In: *Scientific reports* 14.1 (2024), p. 22421.

[Pom+21] Matteo Pompili et al. “Realization of a multinode quantum network of remote solid-state qubits”. In: *Science* 372.6539 (2021), pp. 259–264.

[Rac+15] Niklas Rach et al. “Dressing the chopped-random-basis optimization: A bandwidth-limited access to the trap-free landscape”. In: *Physical Review A* 92.6 (2015), p. 062343.

[Reb+09] P Rebentrost et al. “Optimal control of a qubit coupled to a non-Markovian environment”. In: *Physical review letters* 102.9 (2009), p. 090401.

[Rem+20] Phila Rembold et al. “Introduction to quantum optimal control for quantum sensing with nitrogen-vacancy centers in diamond”. In: *AVS Quantum Science* 2.2 (2020).

[Res+25] Jeremias Resch et al. “High-fidelity control of a ^{13}C nuclear spin coupled to a tin-vacancy center in diamond”. In: *arXiv preprint arXiv:2509.03354* (2025).

[Rog+14] Lachlan J Rogers et al. “All-optical initialization, readout, and coherent preparation of single silicon-vacancy spins in diamond”. In: *Physical review letters* 113.26 (2014), p. 263602.

[Sch+05] T Schulte-Herbrüggen et al. "Optimal control-based efficient synthesis of building blocks of quantum algorithms: A perspective from network complexity towards time complexity". In: *Physical Review A—Atomic, Molecular, and Optical Physics* 72.4 (2005), p. 042331.

[Sch+14] Romana Schirhagl et al. "Nitrogen-vacancy centers in diamond: nanoscale sensors for physics and biology". In: *Annual review of physical chemistry* 65.1 (2014), pp. 83–105.

[Sen+24] Katharina Senkalla et al. "Germanium vacancy in diamond quantum memory exceeding 20 ms". In: *Physical Review Letters* 132.2 (2024), p. 026901.

[Sid+06] I Siddiqi et al. "Dispersive measurements of superconducting qubit coherence with a fast latching readout". In: *Physical Review B—Condensed Matter and Materials Physics* 73.5 (2006), p. 054510.

[Sid21] Irfan Siddiqi. "Engineering High-Coherence Superconducting Qubits". In: *Nature Reviews Materials* 6.10 (2021). DOI: 10.1038/s41578-021-00370-4. URL: https://doi.org/10.1038/s41578-021-00370-4.

[Sin+24] Miralem Sinanović et al. "Non-Markovian Ensemble Propagation". In: *arXiv preprint arXiv:2410.12301* (2024).

[Sip+16] Alp Sipahigil et al. "An integrated diamond nanophotonics platform for quantum-optical networks". In: *Science* 354.6314 (2016), pp. 847–850.

[Sør+18] Jens Jakob WH Sørensen et al. "Quantum optimal control in a chopped basis: Applications in control of Bose-Einstein condensates". In: *Physical Review A* 98.2 (2018), p. 022119.

[SR20] Jaime Sevilla and C Jess Riedel. "Forecasting timelines of quantum computing". In: *arXiv preprint arXiv:2009.05045* (2020).

[Sta+22] P-J Stas et al. "Robust multi-qubit quantum network node with integrated error detection". In: *Science* 378.6619 (2022), pp. 557–560.

[Sun+19] Youngkyu Sung et al. "Non-Gaussian noise spectroscopy with a superconducting qubit sensor". In: *Nat Commun* 10.1 (Sept. 16, 2019), p. 3715. ISSN: 2041-1723. DOI: 10.1038/s41467-019-11699-4. arXiv: 1903.01043[quant-ph]. URL: http://arxiv.org/abs/1903.01043 (visited on 07/23/2024).

[Sun+21] Youngkyu Sung et al. "Multi-level quantum noise spectroscopy". In: *Nature communications* 12.1 (2021), p. 967.

[SWS15] Yuval R Sanders, Joel J Wallman, and Barry C Sanders. "Bounding quantum gate error rate based on reported average fidelity". In: *New Journal of Physics* 18.1 (2015), p. 012002.

[Tay+08] Jacob M Taylor et al. "High-sensitivity diamond magnetometer with nanoscale resolution". In: *Nature Physics* 4.10 (2008), pp. 810–816.

[Tc24] Naoki Takeuchi and colleagues. “Superconducting circuit for qubit control within large-scale quantum computer systems successfully demonstrated”. In: *npj Quantum Information* 9 (1 2024). Accessed: 2025-02-13. DOI: 10.1038/s41534-024-00849-2. URL: https://phys.org/news/2024-06-superconducting-circuit-qubit-large-scale.html.

[Uhl76] Armin Uhlmann. “The “transition probability” in the state space of a^*-algebra”. In: *Reports on Mathematical Physics* 9.2 (1976), pp. 273–279.

[Van74a] NG Van Kampen. “A cumulant expansion for stochastic linear differential equations. II”. In: *Physica* 74.2 (1974), pp. 239–247.

[Van74b] Nico G Van Kampen. “A cumulant expansion for stochastic linear differential equations. I”. In: *Physica* 74.2 (1974), pp. 215–238.

[Vez+24] Arian Vezvaee et al. “Fourier transform noise spectroscopy”. In: *npj Quantum Information* 10.1 (2024), p. 52.

[VKL99] Lorenza Viola, Emanuel Knill, and Seth Lloyd. “Dynamical decoupling of open quantum systems”. In: *Physical Review Letters* 82.12 (1999), p. 2417.

[VMB24] Santiago Varona, Markus Müller, and Alejandro Bermudez. “Lindblad-like quantum tomography for non-Markovian quantum dynamical maps”. In: *arXiv preprint arXiv:2403.19799* (2024).

[Wan+24] Peng Wang et al. “Transform-limited photon emission from a lead-vacancy center in diamond above 10 K”. In: *Physical Review Letters* 132.7 (2024), p. 073601.

[Wat+15] Paul Watts et al. “Optimizing for an arbitrary perfect entangler. I. Functionals”. In: *Physical Review A* 91.6 (2015), p. 062306.

[Wei12] U. Weiss. *Quantum Dissipative Systems*. 4th. Singapore: World Scientific, 2012. ISBN: 978-1280669828.

[Wie83] Stephen Wiesner. “Conjugate coding”. In: *ACM Sigact News* 15.1 (1983), pp. 78–88.

[WJ06] Jörg Wrachtrup and Fedor Jelezko. “Processing quantum information in diamond”. In: *Journal of Physics: Condensed Matter* 18.21 (2006), S807.

[WKO21] Hendrik Weimer, Augustine Kshetrimayum, and Román Orús. “Simulation methods for open quantum many-body systems”. In: *Reviews of Modern Physics* 93.1 (2021), p. 015008.

[WS15] Dong-Sheng Wang and Barry C Sanders. “Quantum circuit design for accurate simulation of qudit channels”. In: *New Journal of Physics* 17.4 (2015), p. 043004.

[WZ21] Wei Wu and Ze-Zhou Zhang. “Controllable dynamics of a dissipative two-level system”. In: *Scientific Reports* 11.1 (2021), p. 7188.